11-7-2019

Combined Molecular Dynamics and Phase Field Simulation of Crystal Melt Interfacial Properties and Microstructure Evolution during Rapid Solidification of TI-NI Alloys

Sepideh Kavousi
Louisiana State University and Agricultural and Mechanical College

COMBINED MOLECULAR DYNAMICS AND PHASE FIELD SIMULATION OF CRYSTAL MELT INTERFACIAL PROPERTIES AND MICROSTRUCTURE EVOLUTION DURING RAPID SOLIDIFICATION OF TI-NI ALLOYS

A Dissertation

Submitted to the Graduate Faculty of the
Louisiana State University
and Agricultural and Mechanical College
in partial fulfillment of the
requirements for the degree of
Doctor of Philosophy

in

The Department of Mechanical Engineering

by
Sepideh Kavousi
B.Sc. Tabriz University, 2009
M.Sc. Amirkabir University of Technology, 2013
December 2019

To my parents

Farin and Shamsaddin

ACKOWLEDGEMENTS

I would like to dedicate my sincere gratitude to my advisor Dr. Morel Moldovan and my research committee, Dr. Asle Zaeem, Dr. Meng, and Dr. Vekhter for their tremendous guidance, support, and encouragement during my research. I also thank Dr. Elgrishi for serving on my dissertation committee as the Dean's Representative.

My special thanks go to my parents who sacrificed their lives for me and provided unconditional love and care. I would not have made it this far without them. I would also like to thank my sisters, Azadeh and Farzaneh, for their support and encouragement throughout this doctoral program.

Most importantly, I would like to thank my loving husband Mohammad Soleimani Dodaran, whose affection and support surrounded me with sunshine and made this study possible.

Table of Contents

ABSTRACT

Phase field method has become a popular tool to investigate the microstructure evolution during the solidification. Quantitative predictions using this method is still limited, and in this dissertation, we try to study this problem from different perspectives.

Most of the phase field models consider the solid-liquid interface to be in local equilibrium. Solidification during some manufacturing processes like selective laser melting, and electron beam additive manufacturing is rapid and far from equilibrium which can result in supersaturated solid solutions, segregation-free crystals, or metastable phases. Before obtaining any conclusions from the phase field simulations, we must know the answer for *"which phase field model works for rapid solidifications?"*

Solidification involves multiple special and temporal scales ranging from picoseconds to seconds, and from nanometers to micrometers. For this, phase field method considers interface width and the characteristic dissipation time scale in between those two limits. However, the questions that should be addressed is *"how using diffuse interface phase field models, especially for the rapid solidification, effects the quantitative predictions of this method?"*

The phase field parametrization requires knowing multiple material properties, and experiments are capable of calculating some of these them. The rest of these parameters are either estimated by analytical methods or molecular dynamic (MD), like the solid-liquid interfacial free energies, or considered to zero and non-effective for solidification, like solid-liquid kinetic coefficient. However, it is critical to know *"How the phase field simulation results, especially for rapid solidification, are effected by MD-calculated material properties?"*

To address these questions, in this research, we performed combined MD and phase field simulations to study the solidification of pure Ti and Ti-Ni alloys. MD simulations are used to

calculate interfacial properties, namely anisotropic kinetic coefficient and solid-liquid interface free energy. The first step for obtaining reliable MD simulation results is having an accurate interatomic potential. For this, we developed a new MEAM interatomic potential predicting the high-temperature solid liquid coexistence. We also performed MD simulation to yield a detailed understanding of the kinetic processes that occur during rapid solidification and the results are compared with different phase field simulations to test the consistency of these two simulation methods.

1 INTRODUCTION

During the solidification of metallic systems, microstructure grows in tree-like structures called dendrites. The morphology of dendrites formed during the solidification has a strong effect on the mechanical properties of the final product. For instance, the fine dendritic structures present a better ductility and yield strength than the coarser structures [1, 2]. Therefore, it is very important to predict solidification phenomena under different manufacturing conditions in the field of computer-aided design of materials [3].

Various simulation methodologies have been used over the last decades, including phase-field (PF) method [4] to solve the solidification problem. PF method was first introduced in the 1980's to study phase transition [5, 6] and was later expanded and applied to investigations in a multitude of areas such as solid-state phase transformations [7, 8], crack nucleation and propagation [9], dislocation dynamics, and precipitation growth [10-14].

The first PF models were limited to choose the diffuse interface width very close to the physical interface, but the models presented later enabled considering of the interface width much larger than the physical interface [15-18]. There are different phase field models to predict the binary alloy solidification such as WBM [19] , parabolic EFKP [15], hyperbolic EFKP [18], hyperbolic and parabolic finite interface dissipation [20]. Phase field simulations have been widely used to study the microstructure evolution during solidification of pure metals [14, 16, 21, 22] and alloys [23-28] as it does not require to track the sharp interface.

In spite of all its advantages, PF method has some limitations. The first limitation is defining accurate material properties. PF parameters are obtained by matching classical balance equations across a sharp interface with the PF equations using asymptotic analysis [15]. Sharp interface models are formulated based on the diffusion of heat and solute in the solid and liquid

phases, mass and heat conservation across the interface. The interfacial free energy, kinetic coefficient, and their anisotropy coefficients are important input parameters and need to be known accurately for quantitative prediction in a PF simulation of solidification. A major limiting factor of quantitative prediction of the characteristics of solidification process with PF simulation approach is the scarcity of available experimental data pertaining to crystal-melt interfacial properties, especially the anisotropy coefficients for interfacial energy and kinetic coefficients of the materials. Because the undercooled melt solidifies very rapidly, there are only a few experiments that have successfully measured the solidification velocity, and there are no reports on experimental measurement of interfacial anisotropy coefficients [29-31].

The second limitation is that it most models work for the low-velocity solidification where the interface can be considered to be in local equilibrium. When the solidification velocity is low, the process can be considered as an equilibrium one, in which the solute concentration in the liquid and solid phases at the crystal-melt interface are governed by the equilibrium phase diagram. Casting is an example of a low cooling rate process. In these processes, the kinetic undercooling term is neglected. Rapid solidification, which occurs during the laser melting [32] and containerless processing techniques [33], is a far from equilibrium process that can result in supersaturated solid solutions, micro segregation-free crystals, or metastable phases [34]. As the solidification rate increases, the jump in concentration across the interface deviates from the equilibrium value predicted from the phase diagram and vanishes as the velocity becomes sufficiently large. This phenomenon is called “solute trapping”. In rapid solidification, the interface is not in local equilibrium and the kinetic undercooling should be also considered. Recently a new PF model is developed by Pinomaa and Provatas [35] where the partition coefficient fits well with the analytical models of solidification at high velocities[36] but this

model, in oppose to other phase field models like EFKP, emphasizes on using a non-zero value of the crystal-melt kinetic coefficient.

Molecular dynamics (MD) simulations provide a detailed understanding of the kinetic processes happening during the solidification. They can also provide numerical values of the physical quantities that are necessary to model the continuum level simulations [37], such as the kinetic coefficient and crystal-melt interfacial free energy, which are difficult to obtain from experiments. In order to calculate PF parameters, having a reliable interatomic potential to perform MD simulations is crucial. Comparing the PF simulations with the experimental data requires the employed interatomic potential to reproduce the crystal-melt phase equilibrium conditions. For pure material, the thermal and physical properties such as the melting point, latent heat of fusion, are important factors in choosing the interatomic potential. For the alloys, in addition to the pure material properties, other properties like the solute partitioning, solidus, and liquidus slopes are also determinative factors in choosing parameters.

The main goal of this research is the prediction of non-equilibrium solidification happening during the rapid solidification of pure Ti and Ni-Ti alloys. The quantitative prediction of solidification requires a better understanding of crystal-melt (CM) interfacial properties. For this means, we focus on investigating the effects of kinetic and capillary anisotropies on the crystal morphology and growth rate in the solidification of pure titanium and binary Ni-Ti alloy using a combined MD with PF simulation approach.

To achieve the goals and objectives of this study, the dissertation is organized into five chapters. The present chapter briefly discusses the problem statement and objectives of this dissertation. The rest of the proposal is organized as following.

Chapter 2 will more exclusively conduct a review of the literature. It is divided into five main parts. In the first part, the general principals of solidification are discussed. It is then followed by a brief description of sharp interface and diffuse interface (phase field) models. In the fourth section, we will discuss the basics of molecular dynamics. In the end, it is illustrated that how the molecular dynamics and PF parameters are interconnected via the thin interface analysis.

Chapter 3 includes the details of the 2NN-MEAM potential for the Ni-Ti binary alloy that we have developed which is capable of predicting the crystal-melt interfacial properties in high temperatures. This potential is tested by calculating multiple, physical, thermal, and transport properties, for the pure Ni and Ti, and binary Ni-Ti alloy in the Ni-rich and Ti-rich compositions.

Chapter 4 presents the molecular dynamics simulations to calculate interface and kinetic properties. For pure Titanium and Ti- rich part of Ti-Ni alloy, the kinetic coefficient and CM interface energy and their anisotropy parameters are calculated.

Chapter 5 will present the phase field simulation to study the solidification of pure Ti and binary Ni-Ti system. The phase field parameters are estimated using the MD-calculated anisotropic crystal-melt interfacial properties. We have also investigated the effects of different anisotropic parameters on the dendrite shapes and growth rate.

Chapter 6 summarizes the new insights and significant findings of the present study.

2 LITERATURE REVIEW

Solidification is the transformation of a non-crystallographic state to a crystallographic state. Solid to liquid phase transformation is the basis of numerous manufacturing processes like casting, selective laser melting, additive manufacturing, single crystal growth for semiconductors and metal glass formation [38]. Solidification involves multiple spacial and temporal scales. When studying the kinetics of attachment of liquid atoms to the crystal during solidification, the time scale should be in the order of picoseconds and the solid-liquid interface thickness is assumed few nanometers. While the microstructural features are observed on the length scale of hundreds of micrometers and the diffusion of heat and solute during solidification should be studied in the time scale of seconds. Capturing the physics of solidification over such multiple length scales, while still capturing long enough times to make contact with experiments requires innovations in both mathematical models and numerical simulation techniques [39].

In this chapter, we will first summarize basic concepts of solidification followed by different methods to study the solidification, namely the sharp and diffuse interface (Phase field) method and Molecular Dynamics (MD). In the last section, we will discuss the interconnection of phase field and MD by thin interface analysis.

2.1 Solidification

The solidification starts after the formation of a very small solid particle called nuclei. A Pure element can be undercooled as low as 250 K below its melting point if the system does not have any impurities and we do not let homogenous nucleation on the container walls. However, this is not the case for most of the applications because, in industrial applications, even pure material have very small amounts of impurities.

In modeling of solidification, the growth kinetics is expressed by equation 2.14 relating the interface velocity to the effective solidification driving force, ΔG_{eff}, using the kinetic prefactor velocity, V_c, which is the maximum solidification velocity at infinite driving force [40].

$$V(T, C_s, C_L) = V_c\left[1 - exp(\Delta G_{eff}/RT)\right] \quad (2.1)$$

The crystal-melt interface for the metallic systems is known to be rough; it means the interface grows normal to itself and the growth rate is explained by equation 2.2 [41].

$$V \approx \frac{V_c}{RT}\Delta G_{eff} = M\Delta G_{eff}\ , \quad (2.2)$$

where V is the interface velocity, $M=V_c/RT$ is the interface mobility and ΔG_{eff} is the effective solidification driving force. For the solidification of the pure materials, the driving force is given by:

$$\Delta G_{eff} = \frac{L}{T_M}\Delta T \quad (2.3)$$

where L is latent heat, T_M is the melting point of the element and ΔT is the undercooling of the interface below the T_M.

Calculations of the driving force for solidification of alloys is a little bit different. The solid and liquid phases with the corresponding C_L^{eq} and C_s^{eq}concenterations are in equilibrium if the chemical potential of each species in the solid and liquid phases are equal. This is shown in Figure 2.1 which schematically demonstrate the solid and liquid molar free energy plot as a function of composition. C is the molar fraction of B and C=0 composition denotes pure A. For each phase with any composition C, the intersects of the tangent to the molar free energy with the vertical C=0 and C=1 axes give the chemical potential of A and B in that phase, respectively. Common tangent among the two solid and liquid phases is also used to estimate the equilibrium compositions of solid and liquid coexistence. The equilibrium chemical potential values, as shown in Figure 2.1, is

calculated by the graphical method of tangents. When the liquid and solid phases have C_L^{eq} and C_s^{eq} compositions, the chemical potentials of the A particles in both solid and liquid are the same. A similar statement is valid for patricles B.

Consider the liquid phase with composition C_L, smaller than C_L^{eq}, goes through phase transformation and turn into solid with C_s composition. To calculate the total driving force available in the transformation we should first plot the tangent line to the liquid free energy at C_L. The difference between the corresponding free energy of this line and the free energy of the solid phase, both at C_s concentration, is the total free energy, ΔG which is expressed by the following equation [42].

$$\Delta G = (1 - C_s)(\mu_S^A - \mu_L^A) + C_s(\mu_S^B - \mu_L^B) \tag{2.4}$$

During the solidification of alloys, the concentration of solute at the solid side and liquid side of the interface is not equal. The solute particles rejected into the liquid, will be transported by the diffusion. The dissipation of free energy due to the diffusional process happening in the solid-liquid interface is the called "solute drag" [36, 38]. Solute drag tends to reduce the available driving force for the interface motion and the effective driving force, ΔG_{eff}, is smaller than ΔG. Solute drag is a kinetic effect and it cannot be specified from the equilibrium free energy diagrams. In Figure 2.1, the maximum value of drag free energy is shown as ΔG_D. For estimating the maximum value of solute drag, first, we plot a straight-line passing from C_L and parallel to the tangent line to the solid phase from C_s. At C=C_s the difference between the corresponding free energy by this line and the free energy of solid phase is known as ΔG_D [42]. If we call $\Delta\mu_{B(A)}$ as the chemical potential of solute (solvent) in the solid phase minus that in the liquid, which is a function of temperature (T) and composition (C) of solute in the solid and liquid phase, ΔG_D can be written as

$$\Delta G_D = (C_L - C_s)\,(\Delta\mu_A - \Delta\mu_B) \tag{2.5}$$

The actual driving force for the solidification would be:

$$\Delta G_{eff} = \Delta G - \mathfrak{D}\Delta G_D = \big(1 - C_{eff}\big)(\mu_S^A - \mu_L^A) + C_{eff}(\mu_S^B - \mu_L^B)\,, \tag{2.6}$$

where

$$C_{eff} = (1 - \mathfrak{D})C_S + \mathfrak{D}C_L \tag{2.7}$$

The parameter $\mathfrak{D}$ takes values between zero and one representing no and complete solute drag, respectively [36]. Equation 2.2 with the corresponding effective free energy for the solidification of alloy is used to correlate the interface velocity to the effecting driving force.

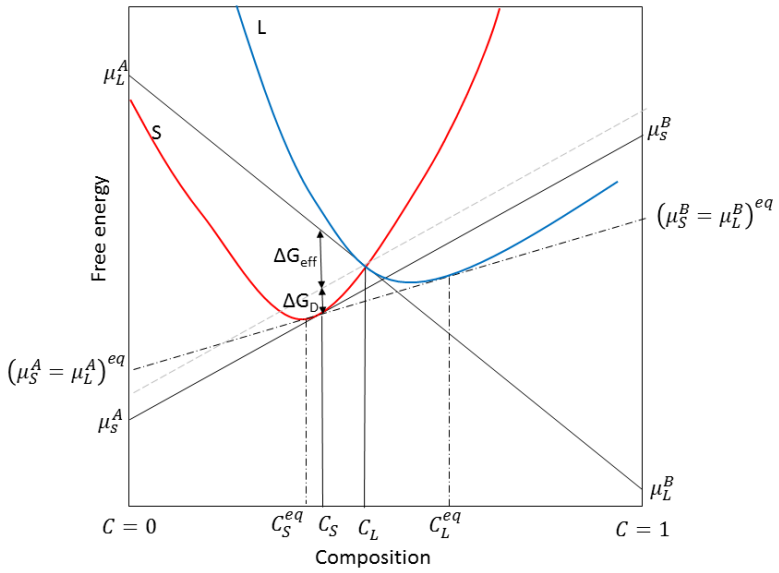

Figure 2.1. Solid and liquid free energy versus composition. It is used to demonstrate the effective free energy and solute drag component of free energy.

2.2 Sharp interface models

The sharp interface models consider the interface width much smaller than the capillary length, which is the smallest characteristics length in the solidification process[35] and for this, we can say in these models the interface width is assumed to be zero.

In the solidification of a pure melt, the temperature at any point along the moving liquid-crystal interface, T_I, is governed by the velocity-dependent Gibbs-Thomson (GT) relation [4] given by:

$$T_I = T_M - \frac{T_M}{L}\sum_{i=1,2}\frac{1}{R_i}\left[\gamma(\hat{n}) + \frac{\partial^2\gamma(\hat{n})}{\partial\theta_i^2}\right] - \frac{V}{\mu(\hat{n})}, \tag{2.8}$$

where T_M is the melting temperature and L is the latent heat of melting per unit volume. The second term on the right-hand side of equation 2.8 represents the local change of the interface equilibrium temperature due to the curvature of the interface, where R_i (i=1,2) are the local principal radii of curvature, $\gamma(\hat{n})$ is the interfacial excess free energy, $\gamma(\hat{n}) + \frac{\partial^2\gamma(\hat{n})}{\partial\theta_i^2}$ is the interfacial stiffness, and θ_i is the local angle between the interface normal direction ($\hat{n}$) and the two local principal directions. The last term on the right-hand-side of equation 2.8 represents the non-equilibrium kinetic undercooling, where $\mu(\hat{n})$ and V are the kinetic coefficient and solidification velocity for the interface normal direction, respectively.

For a dilute binary alloy and considering a straight liquidus and solidus line with m_l^e and m_l^e/k_e slopes, respectively, there are different non-equilibrium sharp interface theories to predict the dependence of interfacial kinetics and solute redistribution. In the classical models the liquidus line slope is assumed to stay constant versus velocity, and the generalized Gibbs-Thomson equation for dilute binary alloys is:

$$T_I = T_M - |m_e|C_L - \frac{T_M}{L}\sum_{i=1,2}\frac{1}{R_i}\left[\gamma(\hat{n}) + \frac{\partial^2\gamma(\hat{n})}{\partial\theta_i^2}\right] - \frac{V}{\mu(\hat{n})} \tag{2.9}$$

There are other models namely Continuous Growth Model (CGM), developed by Aziz and Kaplan [40], and the local non-equilibrium model (LNM) developed by Sobolev and Galenko [43-45], where the slope of liquidous line is considered to change by velocity, as shown by the following equations [36].

$$m_L(V) = m_L^e f\big(k(V)\big), \tag{2.10}$$

$$f\big(k(V)\big) = \frac{[k+(1-k)\mathfrak{D}]\log\left(\frac{k}{k_e}\right)+1-k}{1-k_e} \tag{2.11}$$

For a flat interface with an externally imposed temperature at the interface, T, and concentration of the liquid-side of interface, c_L [36]:

$$T = T_M - f(k)|m_l^e|c_L - \frac{V}{\mu} \tag{2.12}$$

$$\frac{C_L}{C_L^0} = \frac{1}{f(k)}\left(1 + \frac{T_l - T}{|m_l^e|c_L^0} - (1-k)d_0\kappa - (1-k)\beta V\right) \tag{2.13}$$

where C_L^0 is the equilibrium liquid concentration at that temperature, d_0 is the solute capillary length, κ is the interface curvature, T_l is the liquidus temperature, $\beta = 1/(\mu\Delta T_0)$ is the kinetic coefficient, and ΔT_0 is the freezing range. For small velocities, the partition coefficient can be assumed at the equilibrium value. In this limit f(k)≈1 and equation 2.12 turns into the classical Gibbs-Thomson equation. Therefore, the classical solidification models only works for slow solidification velocities. Following are two sharp interface models, CGM and LNM, describing the crystal growth kinetics at high velocities.

2.2.1 Continuous growth model

In the CGM for the ideal dilute binary alloy, the non-equilibrium partition coefficient, in terms of interface velocity V, can be written as [36]:

$$k(V) = (k_e + V/V_D^{CGM})/(1 + V/V_D^{CGM}) \tag{2.14}$$

where k_e is the equilibrium partition coefficient, and V_D^{CGM} is the diffuse interface velocity which denotes the velocity at which solute move across the interface. CGM [46] defined V_D^{CGM} as a function of temperature and interface mobility which cannot be calculated directly. It is a free parameter which is estimated by fitting the dependence of the partition coefficient to velocity from

the experiment to the CGM model. Cook and Clancy [47] performed MD simulations to study the impurity segregation in Lennard-Jones metals and they showed estimating V_D^{CGM} as the ratio of bulk liquid diffusivity to interatomic spacing does not affect the results significantly.

2.2.2 Local non-equilibrium model

Unlike the CGM, the LN model predicts a finite velocity can lead to complete solute trapping. The non-equilibrium partition coefficient is written as [43-45]:

$$k(V) = \begin{cases} \frac{\left(1-\left(V/V_B^{LNM}\right)^2\right)k_e+V/V_D^{LNM}}{1-\left(V/V_B^{LNM}\right)^2+V/V_D^{LNM}} & V < V_B^{LNM} \\ 1 & V > V_B^{LNM} \end{cases}, \tag{2.15}$$

where V_B^{LNM} is the bulk diffuse velocity, calculated by the square root of liquid diffusivity divided by the relaxation time for the steady-state flux, and V_D^{LNM} is interface diffuse velocity. This model predicts the occurrence of complete solute trapping at a large but finite velocity.

Olsen and Hultgren [48], Falkenhagen and Hofman [49] and Duwez *et al.* [50, 51] conducted the first experiments to study the extension of solubility limits by increasing the cooling rates. Since then, many experiments have been performed on multiple binary alloys to explore the solute trapping, but there are still some unsolved issues, like estimating the velocity in which the complete solute trapping happens, or how the solute trapping depends on the crystallographic growth orientation. Experimental studies for multiple binary alloys [48-53] shows that at a finite value of solidification velocity, the complete solute trapping occurs. While the CGM, in contrary with the experiments, predicts the complete solute trapping will occur when velocity asymptotically increases to infinity, the LNM found the onset of full solute trapping at a large but finite velocity. Although CGM is not consistent with the experiments for high solidification velocities, it is widely used because at the moderate velocity regime, which is relevant to industrial

processes like the additive manufacturing, it gives a valuable and accurate description of solute trapping.

2.3 Diffuse interface models

In a crystal growing from the melt in phase field method, an order parameter is used to describe how each phase evolves during the solidification. For example, we can define the solid phase with $\phi \approx 1$ and the liquid phase with $\phi \approx 0$. The main assumption in PFM is that $\phi(x)$ evolves so that the total free energy *F*, which is defined as a functional of PF parameter, temperature, and concentration, reduces over time. The equations of motion for the fields are derived by taking the variational derivatives of the free energy *F* with respect to the independent variables. The resulting partial differential equations are then solved numerically [54]:

For solidification of pure material, a widely used form for *F* is the following:

$$F[\phi, T] = \int \left\{ \frac{|\varepsilon_\phi \nabla \phi|^2}{2} + f_{dw}(\phi, T) \right\} dV \tag{2.16}$$

The first term on the right-hand-side is the excess free energy due to the interface (sharp change order parameter along the interface). ε_ϕ can be tuned to account for the total surface energy. The second term is the bulk free energy density, which can be separated into the barrier term, only depending on ϕ, and the remaining bulk free energy. PF simulation methodologies allow for significant freedom when choosing the functional form for bulk free energy term. For the solidification of pure material, we consider the form of $f_{dw}(\phi, T)$ as follows:

$$f_{dw}(\phi, T) = wg(\phi) + h(\phi) \frac{L_0}{T_m} (T - T_m) \tag{2.17}$$

where $g(\phi) = \phi^2(1-\phi)^2$ represents the double-well Ginzburg-Landau free energy function, $wg(\phi)$ is the free energy distribution, and $h(\phi)$ is the so-called smoothing function with 0 and 1 values in the liquid and solid phases, respectively [22]. The time evolution of the order parameter,

which is a non-conserved parameter, is described by the PF equation, where M_ϕ is the mobility related to the kinetic coefficient.

$$\frac{\partial \phi}{\partial t} = -M_\phi \frac{\delta F}{\delta \phi} \tag{2.18}$$

For pure material the final time-evolution equations [55] for the two field variables, T and ϕ, are:

$$\frac{\partial T}{\partial t} = D\nabla^2 T + \frac{L_0}{c_p} h'(\phi) \frac{\partial \phi}{\partial t} \tag{2.19}$$

$$\frac{1}{M(\theta)} \frac{\partial \phi}{\partial t} = \nabla.(\varepsilon(\theta)^2 \nabla\phi) + \frac{\partial\left(\varepsilon(\theta)\varepsilon'(\theta)\frac{\partial \phi}{\partial x}\right)}{\partial y} - \frac{\partial\left(\varepsilon(\theta)\varepsilon'(\theta)\frac{\partial \phi}{\partial y}\right)}{\partial x} - wg'(\phi) - h'(\phi)\left(\frac{L_0}{T_m}(T - T_m) + Noise(\phi)\right) \tag{2.20}$$

Both ϕ and T are functions of position, r, and time, t. Typically, in a phase-field model, the anisotropy effect is accounted for by considering the dependence of the ε and M parameters on the angle, θ, between the direction normal to the interface and a specified direction in crystal.

The side branching of dendrites arises from thermal fluctuations. To mimic the thermal fluctuations in a phase-field model, a continuous source of noise is added to the right-hand-side of equation 2.20. $Noise(\phi) = 16R\phi^2(1-\phi)^2$, where R is a randomly generated number that takes values between -1 and +1.

In this study, we will use the EFKP model, explained in [15] for the PF simulation of binary alloys. In this model, considering order parameter ranging from -1 to +1 moving from the liquid into solid, we can set $f_{dw}(c, \phi, T)$ as:

$$f_{dw}(c, \phi, T) = wg(\phi) + \bar{f}_{AB}^{mix}(\phi, c, T)\ , \tag{2.21}$$

where $g(\phi) = (-\varphi^2/2 + \varphi^4/4)$ represents the double-well free energy distribution, and $\bar{f}_{AB}^{mix}(\phi, c, T)$ is:

$$\bar{f}_{AB}^{mix}(\phi, c, T) = f^{A}(T_m) - (T - T_m)s(\phi) + \frac{RT_m}{v_0}(clnc - c) + \epsilon(\phi)c \tag{2.22}$$

$$\epsilon(\phi) = \frac{\epsilon_s + \epsilon_l}{2} + \bar{g}(\phi)\frac{\epsilon_s - \epsilon_l}{2} \tag{2.23}$$

$$s(\phi) = \frac{s_s + s_l}{2} - \tilde{g}(\phi)\frac{L}{2T_m} \tag{2.24}$$

$\bar{g}(\phi)$ and $\tilde{g}(\phi)$ are chosen so that the surface diffusion, interface stretching and chemical potential jump at the interface vanishes [15].

The time evolution of the concentration, which is a conserved parameter, is described by the PF equation:

$$\frac{\partial c}{\partial t} = \nabla.\left(M_c \nabla \frac{\delta F}{\delta c}\right) \tag{2.25}$$

The final time-evolution equations for the two field variables, c and ϕ are explained as [15]:

$$\tau_0\left[1 - (1-k)\frac{z - V_p t}{l_T}\right]\frac{\partial \phi}{\partial t} = W^2\nabla^2\phi + \phi - \phi^3 - \lambda g'(\phi)\left(U + \frac{z - V_p t}{l_T}\right) \tag{2.26}$$

$$\left[\frac{1+k}{2} - \frac{1-k}{2}h(\phi)\right]\frac{\partial U}{\partial t} = \vec{\nabla}.\left(Dq(\phi)\vec{\nabla}U + a(\phi)W[1 + (1-k)U]\frac{\partial \phi}{\partial t}\frac{\vec{\nabla}\phi}{|\vec{\nabla}\phi|}\right) + [1 + (1-k)U]\frac{1}{2}\frac{\partial h(\phi)}{\partial t} \tag{2.27}$$

where U $= \frac{e^u - 1}{1-k}$, $u = \ln(\frac{2c}{c_0^l[1+k-(1-k)\tilde{g}(\phi)]})$, and $a(\phi)$, the anti-trapping coefficient, is considered $1/(2\sqrt{2})$.PF method is capable of realistic simulation of micro-scale dendritic growth, reproducing most of the features observed experimentally. It accurately reproduces the morphology and size of the developing dendrites and captures the phenomena associated with the dendrite formation (eg equilibrium shape and kinetics of the dendrite tip, preferred growth direction, branching and, etc.) [15, 56, 57]**.** Subsequent improved geometrical models together with the incorporation of realistic crystal-melt interfacial energy and/or kinetic properties allowed for a more quantitative description and lead to the development of a variety of PF models used to

study solidification of pure materials [10, 11, 58-64] and alloys [15, 17, 26, 65, 66]. Multiple numerical simulations using diffuse interface PF models have been conducted to investigate the solute trapping [20, 24, 67-69]. In all these simulations, the crystal-melt interface kinetics is considered as zero, which is not applicable for cases with the moderate to high solidification rates. The EFKP model works fine for slow solidifications because the classical thin interface limit considers k (V)=k_e and it cannot be implemented to study the rapid solidification. To overcome this issue, one solution is presented by Gosh et al. [66] where the anti-trapping flux is modified by using higher interface width, W_0, for the higher solidification velocities such that k(V)>k_e.

The second solution is using the thin interface analysis to map the thin interface behavior of the phase field method to the non-equilibrium sharp interface models. The phase field method presented by Pinomaa and Provatas (PP) [35] maps to the CG model and can be used to investigate the rapid solidifications. In this method the anti-trapping, coefficient is modified as following:

$$a_t \rightarrow a_t' = \frac{1}{2\sqrt{2}}\left(1 - A(1-\phi^2)\right) \tag{2.28}$$

A is the trapping parameters and it controls the solute trapping. By considering A=0, the anti-trapping will be equal to the anti-trapping in the EFKP model.

Phase field method has been also widely used in investigating the primary and secondary arm spacing [70-72]. The primary dendritic arm spacing (PDAS) and secondary dendritic arm spacing (SDAS) provide information on the segregation patterns and the distribution of precipitates between the dendritic arms, which influences the mechanical properties [71]. For the steady-state directional solidification, the phase field results are compared with the geometric models relating the dendritic arm spacing to puling velocity, thermal gradient, and alloy concentration. Two well-known theoretical models are the Hunt-Burden [73] and Kruz-Fisher [70] models which both consider the processing conditions, thermodynamic parameters, and geometry

of the cells in their calculations. Burden and Hunt considered only the geometry of the cell tip and obtain the following relation for the arm spacing:

$$PDAS = 2.83(k_e \Gamma \Delta T_0 D_l)^{0.25} G^{-0.5} V^{-0.25} \quad , \tag{2.29}$$

while Kurz and Fisher considered the geometry of the cell tip and trunk and obtained:

$$PDAS = 4.3(\Gamma \Delta T_0 D_l / k_e)^{0.25} G^{-0.5} V^{-0.25} \quad , \tag{2.30}$$

The phase-field method requires previous knowledge of the material properties of the system in study. The input includes bulk properties such as density, heat capacity, and latent heat, and others such as interfacial and kinetic growth coefficients, being the latter properties, which are hardly accessible in experiments. Here molecular simulations play a fundamental role since they provide a link between an interaction potential and all the required properties.

2.4 Molecular Dynamics

MD is a computer simulation technique where, by integrating the equation of motion for each atom, we will be able to study the time evolution of their interaction. Considering an initial set of positions and velocities based on atomic structures and the simulation temperature, the MD simulations are aimed to determine the subsequent time evolution of position and momenta of each particle [74]. Newton's law is used to calculate the force acting on each atom i in a system, F_i.

$$\vec{F}_i = m_i \vec{a}_i \tag{2.31}$$

$$\vec{a}_i = \frac{d^2 \vec{r}_i}{dx^2} \tag{2.32}$$

where $\vec{a}_i$ is the acceleration. If a force acting on an object is a function of position only, it is said to be a conservative force, and it can be derived as the gradient of potential with respect to atomic

displacements. This form implies the presence of conservation law for total energy $E = K+V$, where K is the instantaneous kinetic energy.

$$\vec{F}_i = -\nabla_{\vec{r}_i} V(\vec{r}_1, \vec{r}_2, \dots, \vec{r}_3) \tag{2.33}$$

Given an initial configuration of atoms with initial velocities, and interaction potential between the atoms, a time integration algorithm is required to integrate the equation of motion, equation 2.32. In MD, the most commonly used time integration algorithm is the Verlet Algorithm [75]. In this algorithm, one forward and one backward Taylor expansion for the position is written and added to each other, and the final form is given as:

$$\vec{r}_i(t + \Delta t) = 2\vec{r}_i(t) - \vec{r}_i(t - \Delta t) + a(t)\Delta t^2 + O(\Delta t^4) \tag{2.34}$$

By knowing the interaction potential between the atoms, and the initial velocity and position of atoms, one can calculate the time evolution of the system's trajectory[76].

In order to perform MD simulation, a potential is required, which describe how the particles in the simulation interact. It should be noted that several models have been presented to estimate the interatomic potential in metals such as Finnis-Sinclair (FS) model [77], embedded-atom (EAM) model [78], modified-EAM (MEAM) model [79], and the second nearest-neighbor (2NN) MEAM model [80]. As the 2NN-MEAM potential will be used in this research, we will explain this potential with more details.

2.4.1 MEAM potential

Baskes [79] proposed modified embedded atom method (MEAM) interatomic potential which was especially suitable for the simulation of multi-component systems. Later, Lee and Baskes [80] modified the MEAM potential to take into account the second-nearest neighbor interactions. Details of the MEAM potential has been published in the literature [80-82] and will be briefly reviewed here.

The total energy, E, for a system of atoms is approximated as the sum of atomic energies, E_i.

$$E = \sum_i E_i = \sum_i F_i(\bar{\rho}_i) + \frac{1}{2} \sum_{i \neq j} S_{i,j} \varphi_{ij}(r_{ij}) \ , \tag{2.35}$$

The first term on the right-hand side of this equation is related to the embedding energy, which can be interpreted as the energy cost to insert an atom at the site of atom i with the background electron density, $\bar{\rho}_i$. Background electron density, given by equations 2.36, and 2.37, is calculated by combining several partial electron density ($\rho_i^{(k)}$ $(k = 1 - 3)$) terms with weighting factors $\bar{t}^{(k)}$ $(k = 1 - 3)$ which are calculated using equation 2.38 .

$$\bar{\rho}_i = \frac{\rho_i^{(0)}}{1 + e^{-\Gamma_i}} \tag{2.36}$$

$$\Gamma_i = \sum_{k=1}^{3} \bar{t}^{(k)} \left(\frac{\rho_i^{(k)}}{\rho_i^{(0)}} \right)^2 \tag{2.37}$$

$$\bar{t}^{(k)} = \frac{1}{\rho_i^{(0)}} \sum_{i \neq j} t^{(k)} \rho_j^{a(0)} S_{ij} \tag{2.38}$$

S_{ij} is the screening function that ranges between 0 and 1 [83]. Two extreme values of $S_{i,j} = 0$ and 1 mean the interaction between the atoms i and j are fully-screened and non-screened, respectively. A detailed description of the multi-body screening function is presented later in this section. Each partial electron density in equation 2.37, $\rho_i^{(k)}(k = 0 - 4)$, is a function of atomic configuration and atomic electron density. The atomic electron density is computed as:

$$\rho_i^{a(k)}(r_{ij}) = \rho_{i0} \exp\left[-\beta_i^{(k)} \left(\frac{r_{ij}}{r_i^0} - 1 \right) \right] \tag{2.39}$$

r_i^0 is the nearest neighbor distance in reference structure, reference structure, where all the atoms are at their perfect crystal structure. $\beta_i^{(k)}(k = 1 - 3)$, are adjustable element-dependent parameters, and ρ_{i0} is element dependent density scaling factor. The partial electron densities are given by equations 2.40- 2.44.

$$\rho_i^{(0)} = \sum_{i \neq j} S_{ij} \rho_j^{a(0)} \tag{2.40}$$

$$(\rho_i^{(1)})^2 = \sum_{\alpha} \left[\sum_{i \neq j} \frac{r_{ij}^{\alpha}}{r_{ij}} S_{ij} t^{(1)} \rho_j^{a(1)} \right]^2 \rho_i^{(0)} / Q^{(1)} \tag{2.41}$$

$$(\rho_i^{(2)})^2 = \left\{ \sum_{\alpha,\beta} \left[\sum_{i \neq j} \frac{r_{ij}^{\alpha} r_{ij}^{\beta}}{{r_{ij}}^2} S_{ij} t^{(2)} \rho_j^{a(2)} \right]^2 - \frac{1}{3} \left[\sum_{i \neq j} S_{ij} t^{(2)} \rho_j^{a(2)} \right]^2 \right\} \rho_i^{(0)} / Q^{(2)} \tag{2.42}$$

$$(\rho_i^{(3)})^2 = \left\{ \sum_{\alpha,\beta,\gamma} \left[\sum_{i \neq j} \frac{r_{ij}^{\alpha} r_{ij}^{\beta} r_{ij}^{\gamma}}{{r_{ij}}^3} S_{ij} t^{(3)} \rho_j^{a(3)} \right]^2 - \frac{3}{5} \left[\sum_{i \neq j} \frac{r_{ij}^{\alpha}}{r_{ij}} S_{ij} t^{(3)} \rho_j^{a(3)} \right]^2 \right\} \rho_i^{(0)} / Q^{(3)} \tag{2.43}$$

$$Q^{(k)} = \sum_{i \neq j} S_{ij} (t^{(k)})^2 \rho_j^{a(0)} \tag{2.44}$$

r_{ij}^{α} , r_{ij}^{β}, and r_{ij}^{γ} represent the α, β and γ component of r_{ij}. After defining the background electron density using equations 2.36-2.44, the embedding energy is calculated using equation 2.45. A_i is an arbitrary scaling factor and E_i^0 is the cohesive energy.

$$F(\bar{\rho}_i) = \begin{cases} A_i E_i^0 \bar{\rho}_i \ln(\bar{\rho}_i) & \bar{\rho}_i \geq 0 \\ A_i E_i^0 \bar{\rho}_i & \bar{\rho}_i < 0 \end{cases} \tag{2.45}$$

The second term on the right-hand side of equation 2.35 is related to the pair potential. $\varphi_{ij}(r_{ij})$ is the pair interaction between atoms i and j separated by r_{ij}. While the embedding function, F_i, has a given specific form, shown in equation 2.45, the pairing interaction function is not known. For calculating the pairing interaction first the total energy per atom for the reference structure is calculated using the zero-temperature universal Rose–Vinet equation of state [84] given in equations 2.46 and 2.47:

$$E_{ij}^{u} = -E_i{}^0 \left[1 + a^* + \delta \frac{r_{ij}^0}{r_{ij}} (a^*)^3\right] e^{-a^*} \tag{2.46}$$

$$a^* = \alpha_{ij} \left(\frac{r_{ij}}{r_{ij}^0} - 1\right) \tag{2.47}$$

E_{ij}^{u} is the total energy of the reference structure, a^* is the scaled distance from the nearest neighbor in reference structure, δ is an adjustable element-dependent parameter that takes positive and negative for $a^* \geq 0$, and $a^* < 0$, respectively. Then the pair interaction is evaluated from the known values of total energy and embedding function of the reference structure. It is also necessary to use a screening or cut-off procedure to limit the range of interaction by using a screening function.

In the original MEAM potential, the second-nearest neighbor interactions were neglected by using strong screening function values. While the 2NN-MEAM potential considers the second nearest neighbor interactions in the screening function by adjusting the screening functions [82]. The screening factor between atoms i and j, S_{ij}, has two extreme values of 0 and 1, which represents the full-screening and no-screening respectively. S_{ij} depends on the distribution of atom k which is the common neighbor of the atoms i, and j. The S_{ikj} is generated using a simple geometric construction [83]. Consider atom i,j,k are all on a plane, as shown in Figure 2.2. The origin is set on the mid-point between i and j. Now consider an ellipse passing through the atoms i,j, and k with the minor axis of the ellipse on the line connecting atoms let r_{ij} be the distance between atom i,j. The equation of this ellipse is given by:

$$x^2 + \frac{y^2}{C} = \left(\frac{1}{2} r_{ij}\right)^2 \tag{2.48}$$

C controls the extension of the ellipse in the y-direction and is determined by:

$$C = \frac{2(X_{ik} + X_{kj}) - (X_{ik} - X_{kj})^2 - 1}{1 - (X_{ik} - X_{kj})^2} \tag{2.49}$$

where $X_{ik} \equiv \left(r_{ik}/r_{ij}\right)^2$ and $X_{kj} \equiv \left(r_{kj}/r_{ij}\right)^2$. For instance, the corresponding values of C for perfect FCC and BCC crystal structures are 1 and 2, respectively. The blue and red counters in Figure 2.2 are the corresponding C plots for the perfect BCC and FCC crystal structure.

In 2NN-MEAM potential, the screening factor is specified by two parameters C_{min} and C_{max}. When the ellipse passing from atoms *i*,*j*, and *k* is outside the ellipses defined by C_{max}, C_{min}, it means atom *k* does not screen the interaction between atoms *i* and *j* and S_{ikj} will be considered 1. On contrary, if the ellipse passing from atoms *i*,*j*, and *k* is inside the ellipses defined by C_{max}, C_{min}, it means atom *k* fully screens the interaction between atoms *i* and *j* and S_{ikj} will be considered 0. When the ellipse passing from atoms *i*,*j*, and *k* is between the ellipses defined by C_{max} and C_{min}, S_{ikj} will vary smoothly between 0 and 1. The overall form of S_{ikj} is assumed to follow the following form with the cut-off function of $f_c(x)$.

$$S_{ikj} = f_c\left(\frac{C-C_{min}}{C_{max}-C_{min}}\right) \tag{2.50}$$

$$f_c(x) = \begin{cases} 1 & x \geq 1, \\ (1-(1-x)^4)^2 & 0 < x < 1, \\ 0 & x \leq 1, \end{cases} \tag{2.51}$$

The same radial cut-off function is applied to the pair potential in the form of $f_c((r_c - r)/\Delta r)$, where r_c is the cut-off distance and Δr controls the distance over which the radial cut-off is smoothened from 0 to 1 near r_c. S_{ij} is calculated using equation 2.52 and 2.53.

$$\bar{S}_{ij} = \prod_{k \neq i,j} S_{ikj} \tag{2.52}$$

$$S_{ij} = \bar{S}_{ij} f_c\left(\frac{r_c - r}{\Delta r}\right) \tag{2.53}$$

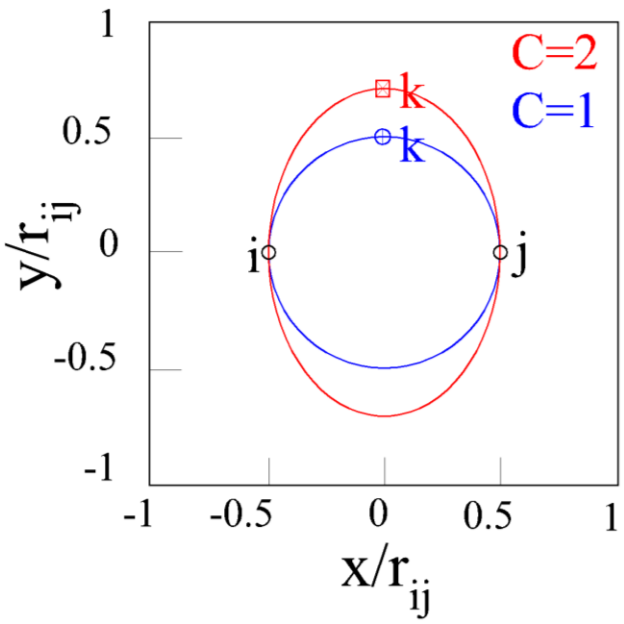

Figure 2.2. Screening of atoms i, j by the neighboring atom k

2.4.2 Crystal-melt properties calculated by molecular dynamics

2.4.2.1 Interface energy

There are various MD methods used to calculate the solid-liquid interfacial free energy such as the cleavage method [85], the critical nucleus method [86], metadynamics [87], transition interface sampling [88], the mold integration method [89], the interface pinning method [90], and the CFM [91]. Here, we use the CFM, which was chosen due to its relative simplicity, ability to obtain anisotropy coefficients and applicability to alloys for future use.

Interface energy is calculated using the CFM. The solid-liquid coexistence system is quasi-two-dimensional; the interface length (W) in the x direction is much larger than its width (b) in the y direction. The system is very long (L) in the interface normal direction to avoid any interactions between the interfaces. The simulation system is shown in Figure 2.3.

Let $h(x)$ be the position along the z direction of an interface separating solid and liquid phases. Its deviation from the mean value, $\langle h \rangle$, can be written as a summation of Fourier modes: $h(x) - \langle h \rangle = \sum_k A(k)\, e^{ikx}$. Based on the equipartition of energy on the degrees of freedom applied to individual capillary fluctuation modes, the interface stiffness can be calculated using:

$$\gamma + d^2\gamma/d\,\theta^2 = \frac{k_B T}{bW\langle |A(k)|^2 \rangle k^2} \tag{2.54}$$

where, $k_B T$ is the thermal energy, $\langle |A(k)|^2 \rangle$ is the mean squared amplitude of the Fourier modes and k is the mode wave number. Plotting $k_B T/(bW\langle |A(k)|^2 \rangle)$ versus k^2 and fitting for small values of k gives a slope which is the interface stiffness.

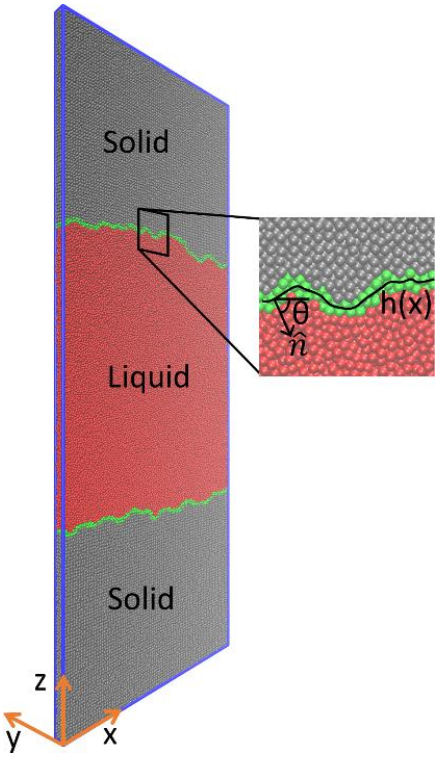

Figure 2.3. A snapshot from the MD simulation of pure titanium depicting the thermal fluctuations of the liquid-crystal interface. The gray atoms represent the solid and the red atoms represent the liquid phase. The green atoms are those located at the liquid-solid interface and the solid line represents the interface location where the order parameter has a value halfway between that of bulk solid and bulk liquid.

For the pure material, the interface energy will be calculated at exactly the melting point. For the binary alloy, the interface energy and anisotropy parameters can be as a function of composition or temperature.

The interfacial free energy and anisotropy coefficients are obtained from MD simulations for aluminum [92], iron [93], magnesium [94], nickel [91], gold and silver [95] elements, as well as alloys such as nickel-aluminum [96] and nickel-copper [97] and nickel-silver [98].

2.4.2.2 Interface mobility and drag coefficient

Calculating the chemical potential of each species is solid and liquid phases are required to estimate the interface mobility and drag coefficient using equations 2.2, 2.6, and 2.7. For this, we use the semi-grand canonical (SGC) ensemble methodology. SGC discussed in [99] is often used to obtain phase diagram information, the free energy, $\Delta G(T,X)$, and chemical potential differences between elements, $\Delta\mu$, as a function of temperature (T) and mole fraction (X), for the liquid and solid phases.

Using the Gibbs-Helmholtz equation, the difference between the free energy of solid and liquid for a single element, $\Delta G(T,0)$, can be written as:

$$\Delta G(T,0) = T\int_{T}^{T_m} \frac{H^{sol}(T\prime)-H^{liq}(T\prime)}{T\prime^2}\,dT' \tag{2.55}$$

where T_m is the melting point, H^{sol} and H^{liq} are the solid and liquid enthalpies. In the SGC, the chemical potential difference between atom types is set and swapping of atom types is performed such that the set chemical potential difference is achieved on average. The main result of a simulation in the SGC is the average concentration corresponding to the set chemical potential difference. For a binary system at a given temperature, T, the free energy of either solid or liquid phase, as a function of concentration is:

$$G(\mathrm{T},X) = G(\mathrm{T},0) + k_B T\big(X\ln X + (1-X)\ln(1-X)\big) + \int_0^X \Delta\mu_{ex}(\mathrm{T},X')dX' \tag{2.56}$$

The second term is the integral of the ideal chemical potential difference and the third term is the integral of the excess chemical potential difference, $\Delta\mu_{ex}$. Since the free energy difference is related to an integral of the chemical potential over concentration, several semi-grand ensemble simulations are required with concentrations going down to small values. Since an arbitrary reference can be chosen, $G^S(T,0)$ or $G^L(T,0)$ can be set to zero and the other one can be obtained from equation 2.55 which is equivalent to applying equation 2.56 to both phases and taking the difference. The liquidus and solidus concentrations for a given temperature are the liquid and solid concentrations corresponding to the chemical potential difference where the grand potentials for the liquid and solid are equal.

$$G^L(T,X^L) - X^L\Delta\mu^L(\mathrm{T},X^L) = G^S(T,X^L) - X^S\Delta\mu^S(\mathrm{T},X^S) \tag{2.57}$$

To compute ΔG_{DF} and ΔG_D using equations 2.4 and 2.5, $\Delta\mu_A$ and $\Delta\mu_B$ are needed and can be obtained from SGC results by relating them to G^S, G^L, $\Delta\mu^S$ and $\Delta\mu^L$ [23]:

$$\Delta\mu_A = \mu_A^S - \mu_A^L = G^S(X^S,T) - G^L(X^L,T) - X^S\Delta\mu^S + X^L\Delta\mu^L \tag{2.58}$$

$$\Delta\mu_B = \mu_B^S - \mu_B^L = G^S(X^S,T) - G^L(X^L,T) + (1-X^S)\Delta\mu^S - (1-X^L)\Delta\mu^L \tag{2.59}$$

where mole fractions, X, refer to solute species B.

Calculating the effective free energy, using equation 2.6, and the corresponding interface mobility requires estimating the drag coefficient first. In this study, we use a method similar to the one presented by Yang et al [100]. They estimated the drag coefficient by fitting the velocity versus the effective free energy and determining the optimal drag coefficient as the value, which results in the best linear fit. The drag coefficient is also required for the kinetic coefficient calculations discussing in the following section.

2.4.2.3 Kinetic coefficient

The MD simulation approaches used for calculation of the kinetic coefficient of solid-liquid interfaces can be divided into equilibrium and non-equilibrium methodologies [4]. The equilibrium methods rely on the analysis of the fluctuations of the solid-liquid interface through the capillary fluctuation method (CFM) [4]. The non-equilibrium MD methods are classified as either forced velocity [101, 102] or free solidification [102] approaches. In this study the kinetic coefficient was calculated by using a free solidification method [102].

During an MD simulation, the solid-liquid interface, on average, remains planar. Therefore, according to equation 2.8 for pure material, the slope of the solidification velocity as a function of temperature gives the kinetic coefficient.

$$\mu(\hat{n}) = \frac{V_{\hat{n}}}{(T_M - T_I)} \tag{2.60}$$

For the alloys, the kinetic coefficient can be estimated either as a function of composition or temperature. The driving force for performing the free solidification can be obtained either by reducing the temperature of an equilibrium system (undercooling) at a target concentration or reducing the liquid composition from the equilibrium value at a target temperature. In our simulations, we used the second method and therefore the interface temperature is equal to the equilibrium temperature and it is maintained at a constant value. For a fixed temperature, the kinetic coefficient as a function of composition is estimated by equation 2.61.

$$\beta = \frac{1+\frac{T_l - T}{\left|m_e^l\right| c_0^l} - \frac{c^L}{c_0^l} \times f(k)}{(1-k)V} \tag{2.61}$$

Calculations of kinetic coefficient using MD simulations were reported for various pure elements such as nickel [103, 104], gold and silver [105], aluminum [104], magnesium [94], and

copper [104, 106], and also compounds such as Ni_3Al [107]. To the best of our knowledge the calculations of kinetic coefficient for the alloys has not been performed by MD simulations.

2.5 Thin interface analysis

The PF modeling of pure material and binary alloy solidification, explained in section 2.3, can be mapped onto the classical free boundary problem. The relationship between the parameters in the PF equations and material's parameters are obtained from the mapping process. It can be done at two different limit conditions; sharp interface limit, where the interface width is very small, and thin interface limit, where the interface width, ζ_p, is finite but smaller than the interface curvature and the characteristic length scale of diffusion field. For pure materials, using thin interface analysis the ε_0, w, and M parameters present in the phase field equations are calculated by using the MD-calculated solid-liquid interfacial free energy and its kinetic coefficient in the following equations :

$$\zeta_p = \frac{\varepsilon_0}{\sqrt{w}} 2\sqrt{2}\, ln3 \tag{2.62}$$

$$\gamma = \frac{\varepsilon\sqrt{w}}{3\sqrt{2}} \tag{2.63}$$

$$\frac{1}{\mu} = \frac{1}{3\sqrt{2}} \frac{T_m\sqrt{w}}{\varepsilon L_0 M} - \frac{L_0}{Dc_p} \frac{\varepsilon}{\sqrt{2w}} \int_0^1 \frac{h(\phi)(1-h(\phi))}{\sqrt{g(\phi)}}\, d\phi \tag{2.64}$$

The asymptotic analysis to construct the mapping of the parameters as given in equations 2.65-2.66 is rather complicated and can be found in [16].

For the alloys, using EFKP model, having λ as a free parameter denoting the interface width, the thin interface analysis gives [15]:

$$d_0(\vec{n}) = \frac{\gamma\, T_m}{L\Delta T_0} = a_1 \frac{W(\vec{n})}{\lambda} \tag{2.65}$$

$$\beta(\vec{n}) = a_1 \frac{\tau_0(\vec{n})}{\lambda W(\vec{n})} - a_1 a_2 \frac{W(\vec{n})}{D_L} \tag{2.66}$$

The capillary length and kinetic coefficient are the parameters calculated from MD and used to estimate W and τ_0.a_1 and a_2 are equal to 0.8839 and 0.6867 respectively.

For the PF model of Pianomaa and Provatas, the continuous growth model thin interface limit of the phase field model leads to modification of a_2 used to set the anti-trapping [35].

$$a_2 \rightarrow a_2^{\mp} = J\left(\overline{K} + \overline{F^{\mp}}\right) \tag{2.67}$$

where $a_2^{+}(a_2^{-})$ are used for considering the zero solute drag (full solute drag) and the other constants in equation 2.67 is given by:

$$J = \frac{4\sqrt{2}}{5} \tag{2.68}$$

$$\overline{F^{+}} = \frac{\sqrt{2}ln2}{2} - \frac{\sqrt{2}}{4}A \tag{2.69}$$

$$\overline{F^{-}} = \frac{\sqrt{2}ln2}{2} + \frac{3\sqrt{2}}{4}A \tag{2.70}$$

3 DEVELOPMENT OF 2NN-MEAM POTENTIAL FOR Ni-Ti ALLOY

Several interatomic potentials have been developed for the Ti-Ni binary systems. These include the Finnis-Sinclair (FS) potentials [77] by Lai and Liu [108] and Ren and Sehitoglu [109], the modified-FS potentials by Mutter and Nielaba [110] and Zhong et al. [111], the Gupta potential by Kexel et al. [112], the embedded-atom method (EAM) potential [78] by Farkas et al. [113], the EAM type potential, referred to as a long-range empirical potential (LREP), by Li et al. [114], the modified-EAM method (MEAM) potentials [79] by Ishida and Hiwatari [115] and Saitoh et al. [116], and the second nearest-neighbor (2NN) MEAM potentials [80] by Ko et al. [117], Kim et al. [118], and Muralles et al. [119]. Most of these potentials were developed to reproduce the main characteristics of the martensitic transformation close to the equiatomic composition. For the results of MD simulations to be predictive when simulating melting and solidification processes, the employed interatomic potential needs to be able to reproduce the experimental CM phase diagram to obtain the correct solute partitioning and slopes of solidus and liquidus lines. To the best of our knowledge, currently, there is no interatomic potential that accurately reproduces the CM phase diagram in binary Ti-Ni alloys.

In the chapter, building on the Ni and Ti potentials developed by Ko et al. [117], we developed new unary potentials with improved capability for predicting high temperature properties of Ni and Ti. In addition to providing better predictions of the targeted properties, melting temperature and latent heat, for pure Ti and Ni; the newly developed potentials also improve the prediction of several thermodynamic and transport properties that affect CM equilibrium and kinetic processes, such as density, cohesive energy, diffusion coefficient, and viscosity. We complement the optimization of the unary potentials with the development of a new MEAM potential for the binary Ni-Ti alloy targeting the CM phase diagram for the Ti rich and Ni

rich solutions and liquid phase enthalpy mixing. This new binary potential also improves the prediction of solid and liquid phase properties at high temperatures. The transferability of the binary potential was also tested by monitoring the crystal structure and the formation energies of stable intermetallic compounds in the phase diagram of Ti-Ni.

3.1 Optimization of potential parameters

We improved 2NN-MEAM potentials for Ti, Ni, and Ti-Ni binary systems that reliably predict the crystal-melt (CM) interfacial properties for pure and binary systems and the high temperature portions of the binary system equilibrium phase diagram for both nickel-rich and titanium-rich range of compositions. The parameters of the newly developed potentials were obtained by adjusting them, through a trial and error process, using the initial values of the corresponding parameters for pure Ti and Ni of the 2NN MEAM potential developed by Ko *et al.* [117].

Table 3.1 compares the melting temperature and latent heat of fusion calculated by molecular dynamics simulations, based on the coexistence method explained by Asadi et al. [104] using the original Ko *et al.* potentials [117], with the experimental values of Valencia and Quested [120].

Melting points were calculated using coexistence of liquid and solid phases by keeping the normal stress in the interface normal direction constant and allowing the temperature to evolve toward the melting point through partial melting or solidification of one of the phases [104]. All steps used a 1.5 fs time step. First the solid phase ($10 \times 10 \times 120$ unit cells, 24000 atoms for bcc Ti; $10 \times 6 \times 100$ unit cells, 24000 atoms for hcp Ti; $8 \times 8 \times 96$ unit cells, 24576 atoms for fcc Ni) was equilibrated in the NPT ensemble for 300 ps at the initial guess for the melting point and the average lattice parameters were obtained over an additional 300 ps. Next the atomic positions and

box sizes in the x and y directions were scaled to obtain the average lattice parameters from the previous step. The lower quarter and upper quarter of the atoms were then melted at high temperature while keeping the central half of the atoms fixed in the NVT ensemble for 50 ps. After rescaling velocities back to the initial guess for the melting temperature, the liquid was relaxed in a 500 ps simulation where the temperature and normal stress in the z direction were kept constant but only the liquid atom positions were scaled while keeping the solid atoms fixed. This allowed the liquid which was far from equilibrium to increase its volume before allowing the solid atoms to move. Following this step, the solid atoms no longer fixed, and all atom positions were scaled to keep the normal stress constant and the temperature was kept constant for 1 ns. If significant solidification or melting was observed during this step, then the melting point estimate was revised and the above steps were repeated. If not, then a 10 ns simulation was run where the normal stress was kept constant, but the temperature could change. An improved guess for the melting temperature was then obtained by averaging the temperature in the last 4 ns of that simulation. If this temperature was less than about 3 degrees from the previous guess, no further iterations were used. If not, all previous steps were repeated with the improved guess for the melting temperature.

Note that there are small biases in the melting points due to the finite size of the interfaces and the fact that melting point depends slightly on crystal orientation for finite sized systems and we only considered the (100) planes for fcc and bcc, and the (0001) plane for hcp.

As evident from Table 3.1, the Ko *et al.* potentials underestimate the melting temperatures of Ti by about 225 K and that of Ni by about 164 K. The melting temperature reported by Ko *et al.* [117] for Ti appears to be for the metastable hcp phase since in our MD simulations we obtained a similar value for that phase. In Table 3.1, all high temperature properties for Ti were calculated considering the stable bcc phase. In addition, Table 3.1 shows that there are also differences

between the experimental and calculated values of latent heat of fusion for both Ti and Ni and the consequence of these differences are significant because the latent heat of fusion is directly related to the driving force for solidification. As such, our approach was based on the premise that the first step towards obtaining an improved potential capable of reproducing the crystal-melt alloy phase diagram starts with improving the melting properties of the pure components.

Table 3.1. Calculated melting temperature T_m(K), and latent heat of fusion ΔH_f (kJ/mol) for pure Ti and Ni using the 2NN-MEAM potential by Ko et al. [117], and the corresponding data from experiments [120]. Uncertainties are for 95% confidence intervals.

	Ti		Ni	
Property	Experiment	2NN MEAM (Ko *et al.*)	Experiment	2NN MEAM (Ko *et al.*)
T_m	1942	1651; 1716.0 ± 1.9[a]	1728	1892
ΔH_f	14.17	11.7; 9.07[a]	17.48	20.7

[a] Results obtained from our MD simulations using the same interatomic potential

There are 14 independent parameters describing the single element 2NN MEAM potential. Four of these parameters: E^c, r^e, α, and δ, are related to the pair potential term. The other parameters include the scaling factor parameter A; four decay lengths, $\beta^{(h)}$ (h=0-4); and three weighting factors, $t^{(h)}$ (h=1-3) which are related to the embedding potential term. C_{min} and C_{max} are the parameters controlling the many-body screening. In addition, a reference structure must be chosen. The equilibrium reference structure for a single element can be any structure in which individual atoms occupy the sites of a perfect lattice. We chose fcc for Ni, and bcc for Ti which are the equilibrium phases at the melting points. As a rule of thumb, during the iterative tuning of the potential, the parameters that were being adjusted were chosen such that they had a very limited effect on most of the previously fitted properties such as the equilibrium lattice parameter(s), cohesive energy, and elastic constants. In our study, the guiding criteria was to adjust certain potential parameters such that the resulting potential reproduces the melting point and latent heat

close to the corresponding experimental values. Other calculated transport and thermo-physical properties such as: diffusion coefficient, density, volume change on melting, etc., were not included in the iterative fitting process; instead they were used as part of the validation process by evaluating how well these calculated values match those measured in experiments. During the iterative procedure of adjustment of parameters, whenever a compromise was needed, the melting point was given the priority over the latent heat of fusion.

Table 3.2. Optimized 2NN MEAM potential parameter sets for pure Ti and Ni systems. The parameters depicted in bold are those that were modified from the original potential of Ko et al. [117]. The cohesive energy of the reference structure, Ec, is in eV/atom and the equilibrium nearest neighbor distance, re, is in Å. The reference structures are bcc for Ti and fcc for Ni.

	E^c	r^e	α	A	$\beta^{(0)}$	$\beta^{(1)}$	$\beta^{(2)}$	$\beta^{(3)}$	$t^{(1)}$	$t^{(2)}$	$t^{(3)}$	C_{min}	C_{max}	δ
Ti	4.75	2.85	4.756	0.24	2.2	3.0	4.0	3.0	-18.0	-32.0	**-14.15**	**0.28**	**1.61**	0
Ni	4.45	2.49	5.0607	**0.763**	2.48	1.94	3.46	2.56	2.84	-1.20	**-2.0**	0.95	1.75	0.05

In general, it is not possible to relate the melting point and the enthalpy of fusion to one single parameter in the potential. However, it is known that some parameters have strong effects on certain properties. For example, previous studies have shown that for most materials, small modification of the $t^{(3)}$ parameter has a considerable effect on the melting point [104]. Our study shows that, for Ni, when they are modified together, the parameters $t^{(3)}$ and A have a significant effect on the melting temperature and latent heat. Reducing $t^{(3)}$ reduces the background electron density, which consequently reduces the embedding energy which in turn helps the reduction of the melting point. Reducing the parameter A also reduces the embedding energy. Based on this understanding, for Ti, we modified the parameters $t^{(3)}$, C_{min}, and C_{max}, to adjust the potential to accurately predict its melting temperature. As explained in section 2.4.1, the value of the parameter C at a second neighbor (defined in the ellipse formula) for a perfect bcc crystal is equal to 2. In the

original potential, C_{min} and C_{max} values were 0.25 and 1.58 respectively, so the 2NN interactions were not screened. Increasing both C_{min} and C_{max} to 0.28 and 1.61 has a little effect on screening in the solid phase and does not noticeably affect the solid enthalpy. Table 3.2 presents the potential parameter sets for Ti and Ni.

Extension of 2NN-MEAM potentials of the pure Ti and Ni to the corresponding binary alloy system requires the evaluation of the pair interaction between Ti and Ni atoms. Therefore, 13 additional parameters need to be determined. Four parameters; E^c, r^e, α, and δ; are needed for describing the pair potential. One parameter is the atomic electron density factor ρ_0^{Ni}/ρ_0^{Ti} in the embedding energy function. Finally, eight parameters describe the multi-body screening. First, we need to estimate the potential parameters; E^c, r^e, α, and δ; for the reference structure found in the universal equation of state. The reference structure for the binary system can be any simple compound structure in which each type of atom has only the same type of atoms as its second nearest-neighbors [118]. The binary Ti-Ni system has four stable compounds: NiTi (B19'), NiTi (B2), Ni_3Ti, and $NiTi_2$ [121], and some metastable compounds Ni_3Ti_2 and Ni_4Ti_3 [122]. We chose the reference structure to be the NiTi B2 structure, which is stable at high temperatures. The values of E^c, α, and r^e are chosen based on the corresponding experimental data for enthalpy of formation [123], bulk modulus [124] and the lattice constant [125] of the B2 NiTi compound. The parameter δ is simply taken to be equal to the average of d for each pure element and the parameter ρ_0^{Ni}/ρ_0^{Ti} is kept at unity. There are four C_{min} and four C_{max} parameters remaining which can be modified. The main goal for the developed binary potential is to accurately reproduce the crystal-melt equilibrium coexistence behavior. As such, the fitting procedure favors the prediction of the characteristics of crystal-melt phase diagram and the enthalpy of mixing in the liquid phase. The enthalpy of formation of the stable compounds, melting point of Ni_3Ti and CM phase diagram for

Ni_3Ti on the high Ni concentration side, and liquid densities are used to test the performance of the potential. Table 3.3 presents the optimized potential parameter set for the binary Ti-Ni system. In addition to the 13 parameters mentioned above, Table 3.3 also includes the cutoff distance parameter r_c, and the switching function range, Δr.

In MD simulations, the interaction between atoms is only considered if the separation between atoms is within a cut-off radius, r_c. This is accomplished by smooth switching of the potentials, over a distance Δr, to approach zero at r_c. In the potential optimization procedure for the binary system, the original cut-off radius of 5 Å was used.

Table 3.3. Optimized 2NN-MEAM potential parameter set for the binary Ti-Ni system. The parameters depicted in bold are those that were modified from the original potential of Ko et al. [117]. The units are eV/atom for cohesive energy of the reference structure, E^c, and Å for the equilibrium nearest neighbor distance, r^e; cutoff distance, r_c; and switching function range Δr. The reference structure is B2 NiTi.

E^c	**4.93**	$C_{min}^{Ni\text{-}Ti\text{-}Ni}$	**1.70**
r^e	2.614	$C_{min}^{Ti\text{-}Ni\text{-}Ti}$	**1.60**
α	**4.6338**	$C_{min}^{Ni\text{-}Ni\text{-}Ti}$	**0.15**
ρ_0^{Ni}/ρ_0^{Ti}	1	$C_{min}^{Ti\text{-}Ti\text{-}Ni}$	**0.25**
d	0.025	$C_{max}^{Ni\text{-}Ti\text{-}Ni}$	**2.0**
r_c	5.0	$C_{max}^{Ti\text{-}Ni\text{-}Ti}$	**1.70**
Δr	**0.4**	$C_{max}^{Ni\text{-}Ni\text{-}Ti}$	**2.8**
		$C_{max}^{Ti\text{-}Ti\text{-}Ni}$	**1.9**

To illustrate the role of the appropriate choice for r_c and Δr, the interaction energies of Ti-Ti, Ni-Ti, and Ni-Ni atomic pairs as a function of separation distance between atoms were calculated using the original MEAM potential by Ko et al. [117] and the present MEAM potential. Using $\Delta r = 0.1$ Å, which is the value in the original Ko *et al.* potential, leads to large slopes in the energy near the cutoff distance and correspondingly large forces. In order to reduce the force between atoms, Δr is increased from 0.1 to 0.4 Å.

3.2 Accuracy and transferability of the developed 2NN-MEAM potential for Ti, Ni, and Ti-Ni

When choosing an interaction potential for a MD simulation one should consider both its accuracy and transferability. For these reasons, the physical properties calculated based on the developed MEAM potential are compared with those obtained from a wide variety of DFT and experimental data. Two sets of physical properties are presented in this section. The first set includes the properties that are considered in the parameter optimization procedure, and therefore they are indicative of the accuracy of the developed potential, and second set of properties were used for the assessment of transferability of the newly developed potential. All MD simulations were performed using the LAMMPS software package [126]. For the sake of clarity, the details pertaining to the simulation methodologies that were used for the calculations of various properties will not be discussed here. Instead, we provide the necessary references, which contain the details of these simulation methodologies. This section is divided up into two main sub-sections; the first sub-section deals with testing the transferability and accuracy of the unary potentials and the second sub-section focuses on the same issues pertaining to the binary potential.

3.2.1 Physical properties of pure Ti and Ni

3.2.1.1 Solid phase

3.2.1.1.1 Bulk and defect properties at 0 K

The calculated bulk, elastic, and various defect properties for Ti and Ni are shown in Table 3.4 and Table 3.5. The corresponding data is compared with the results from DFT, experiments, and those obtained by using the original Ko et al. potential. For both Ti and Ni, in the fitting procedure of the potentials, the experimental cohesive energies were considered more reliable than

the DFT values. Both the present and the Ko et al. potentials for Ni yield very similar results. Moreover, it appears that the present potentials for both Ti and Ni underestimate C_{44} by 15% and 33%, respectively. As the main objective of these potentials is to represent the CM interface properties, the mismatch between the shear modulus obtained from simulations and the values obtained from DFT calculations or experimental data was not considered a major issue.

Table 3.4. Calculated bulk and defect properties of pure Ti using the present 2NN-MEAM potential, in comparison with experiment data, DFT data, and previous MEAM potential by Ko et al. [117]. The following properties are listed: the cohesive energy Ec (eV/atom); the lattice constant a and c (Å) and the ratio of c/a; the bulk modulus and elastic constants C11, C12, C13, C33, and C44 (GPa); the vacancy formation energy E_f^{vac}(eV); the surface energies (erg/cm2) for the orientations indicated by the superscripts, and the structural energy differences ΔE (eV/atom).

Property	Experiment	DFT	2NN-MEAM (Ko *et al.* [117])	2NN-MEAM (present)
E_c	4.87 [a]	5.27 [b]	4.86	4.83
a	2.95 [c]	2.93 [b]	2.92	2.92
c	4.68 [c]	4.65 [b]	4.69	4.73
c/a	1.59 [c]	1.59 [b]	1.60	1.62
B	109.7 [d]	113.7 [e]	109.7	110
C_{11}	176.1 [d]	172 [e]	170	158
C_{12}	86.9 [d]	82 [e]	80.4	108
C_{13}	68.3 [d]	75 [e]	74.8	66.7
C_{33}	190.5 [d]	190 [e]	187.1	198
C_{44}	50.8 [d]	45 [e]	42.1	33.9
E_f^{vac}	1.27 [f]	2.045 [b]	1.46	1.83
$E_{surf}^{(0001)}$	1920 [g, k], 2100 [h, k]	1939 [e]	2032	2006
$E_{surf}^{(1\bar{1}00)}$	-	2451 [e]	2307	2255
$E_{surf}^{(11\bar{2}0)}$	-	1875 [e]	2711	2538
$\Delta E_{hcp\rightarrow fcc}$		0.059 [b]	0.011	0.002
$\Delta E_{hcp\rightarrow bcc}$		0.108 [b]	0.078	0.054

[a] Reference [127]. [b] Reference [117]. [c] Reference [128]. [d] Reference [129]. [e] Reference [130].
[f] Reference [131]. [g] Reference [132]. [h] Reference [133]. [k] The experimental value is for polycrystalline solid.

The calculated surface energies have maximum discrepancies of 35% for Ti for the $(11\bar{2}0)$ plane and 17.3% for Ni for the (111) plane. Despite these discrepancies, overall, the comparison

of the surface energy results, obtained by using the two potential sets, shows improvement when using the presently developed potential.

Table 3.5. Calculated bulk and defect properties of pure Ni using the present 2NN-MEAM potential, in comparison with experimental data, DFT data, and previous MEAM potential by Ko et al. [117] The following properties are listed: the cohesive energy E_c (eV/atom); the lattice constant a (Å); the bulk modulus and elastic constants C_{11}, C_{12}, and C_{44} (GPa); the vacancy formation energy E_f^{vac}(eV); the surface energies (erg/cm^2) for the orientations indicated by the superscripts and the structural energy differences ΔE (eV/atom)

Property	Experiment	DFT	2NN-MEAM (Ko *et al.* [117])	2NN-MEAM (present)
E_c	4.45 [a]	4.842 [b]	4.45	4.45
a	3.520 [c]	3.524 [b]	3.521	3.521
B	187.6 [d]	190.9 [b]	185.9	185.9
C_{11}	261.2 [d]	266.1 [b]	260.4	260.9
C_{12}	150.8 [d]	155.1 [b]	148.6	148.3
C_{44}	131.7 [d]	128.5 [b]	111.1	112
E_f^{vac}	1.6 [e]	1.41 [b]	1.51	1.35
$E_{surf}^{(100)}$	2240 [f, h]	2426 [g]	2085	2108
$E_{surf}^{(110)}$		2368 [g]	2148	2095
$E_{surf}^{(111)}$		2011 [g]	1630	1662
$\Delta E_{fcc\rightarrow bcc}$		0.093 [b]	0.088	0.071
$\Delta E_{fcc\rightarrow hcp}$		0.026 [b]	0.01	0.009

[a] Reference [127]. [b] Reference [117]. [c] Reference [134]. [d] Reference [129]. [e] Reference [135].
[f] Reference [132]. [g] Reference [136]. [h] The experimental value is for a crystalline solid.

3.2.1.2 Titanium phase stability

The crystal structure of Ti at room temperature is hcp [137]. At about 1155 K, Ti undergoes an allotropic phase transformation to a bcc (β) phase, which remains stable up to the melting temperature. In this study the allotropic transition temperature for both the original and the present potential is calculated using the method presented by Sun et al. [138] which is based on the Gibbs-Helmholtz equation shown below:

$$\int_{T^{hcp\to bcc}}^{T_m^{bcc}} \frac{\Delta H^{hcp\to bcc}(T)}{T^2}\,dT + \int_{T_m^{bcc}}^{T_m^{hcp}} \frac{\Delta H_m^{hcp}(T)}{T^2}\,dT = 0 \tag{3.1}$$

where, $T^{hcp\to bcc}$ and $\Delta H^{hcp\to bcc}$ are the hcp to bcc allotropic phase transition temperature and the temperature dependent enthalpy difference between the phases, T_m^{bcc} and T_m^{hcp} are the melting temperatures of the bcc and hcp phases, and ΔH_m^{hcp} is the temperature dependent enthalpy difference between the hcp crystal and liquid phases.

The allotropic hcp to bcc phase transition temperature and enthalpy of transition are presented in Table 3.6. The present potential, as well as the original potential by Ko et al. [117], predicts a stable bcc (β) phase at high temperature. The experimental transition temperature is approximately 1155 K [139] and the corresponding values obtained using the present and original potentials are 1312 and 1481 K respectively; values which deviate by 13% and 28% respectively from experiment data. The enthalpy of transition for both potentials are in good agreement with the experiment data [140-142], but they differ considerably from the DFT result [143] which is 2-3 times higher than experimental values.

Table 3.6. Allotropic transition temperature, $T^{hcp\to bcc}$ (K), and enthalpy of transition, $\Delta H_{hcp-bcc}$ ($T^{hcp\to bcc}$) (kJ/mol), for titanium from experiments, DFT, obtained by using the original 2NN-MEAM potential by Ko et al. [117], and by using the present 2NN-MEAM potential.

Property	Experiment	DFT	2NN-MEAM (Ko *et al. [117]*)	2NN-MEAM (present)
$T_{hcp-bcc}$	1155 [a]	-	1481.7	1312.3
$\Delta H_{hcp-bcc}$	3.2 [b] ; 4.17 [c] ; 4.30 [d]	8.97 [e]	3.18	2.86

[a] Reference [139] [b] Reference [140] [c] Reference [141] [d] Reference [142] [e] Reference [143]

3.2.2 Liquid phase

3.2.2.1 Thermo-physical, and transport properties at the melting point

Table 3.7 presents the summary of various thermo-physical and transport properties of pure Ti and Ni at the melting point obtained from experiments and calculated from the current potential and the one developed by Ko et al. The crystal-melt (CM) coexistence approach is used for calculation of the melting point. Details of this method are presented in the paper by Asadi et al. [104].

Table 3.7. Various thermo-physical and transport properties of pure Ti and Ni at their melting points calculated based on the present 2NN-MEAM potential, the potential of Ko et al. [117], and obtained from experiments. The following properties are listed: melting temperature, T_m (K); latent heat of fusion, ΔH_f (kJ/mol); volume change upon melting normalized by the volume of the solid phase, $\Delta V_m/V_s$; density of liquid, ρ_L (g/cm^3); shear viscosity of liquid, η_L (mPa.s); self-diffusivity of liquid, D_L (10^{-5}cm^2/s); and enthalpy of liquid, h_L (kJ/mol). Uncertainties are for 95% confidence intervals.

Property	Ti			Ni		
	Exp.	2NN MEAM (Ko *et al.* [117])	2NN MEAM (present)	Exp.	2NN MEAM (Ko *et al.* [117])	2NN MEAM (present)
T_m	1941 [a]	1716.0 ± 1.9	1942.6 ± 2.6	1728 [a]	1892	1726.7 ± 2.2
ΔH_f	14.15 [b]	9.07	11.45	17.48 [b]	20.7	17.41
$\Delta V_m/V_s(\%)$	2.817 [c]	1.60	1.62	4.5 [d]	7.0	6.1
ρ_L	4.14 [c]	4.25	4.20	7.795 [e]	7.816	7.819
η_L	3.25 [f]	3.024	3.73	4.7 [f]	7.26	6.3
D_L	4.922 [g]	5.73	4.733	3.27 [g]	2.52	2.83
h_L	-399.8 [h]	-405.652	-400.6	-361.6 [h]	-362.9	-364.9

[a] Reference [120] [b] Reference [144] [c] Reference [145] [d] Reference [146]
[e] Reference [147] [f] Reference [148] [g] Reference [149] [h] Reference [150]

As mentioned before, the optimization of the present unary potentials is performed to primarily obtain a good fit of the melting points and latent heats. However, for Ti we found that it was difficult to match both the melting point and the latent heat simultaneously. Therefore, the latent heat for Ti with our potential is significantly improved but still smaller than the experimental

value while we match the experimental melting point. For Ni, we were able to match both the experimental melting temperature and latent heat closely.

The comparison of the volume change upon melting, density, viscosity, diffusivity, and the enthalpy of the liquid phase with the experimental values and the values calculated with the original potential [117] shows that most properties are improved with exceptions for the Ti diffusivity, Ni density, and Ni enthalpy.

3.2.2.2 Temperature-dependence of density and surface tension

The variation of density and surface tension with temperature, for both Ti and Ni in the liquid phase, were calculated by MD simulations using both the present and the original potential of Ko et al. Over a limited range of temperatures, both density and surface tension can be assumed to be linear functions of temperature:

$$\rho = \rho_m + d\rho/dT\ (T - T_m) \tag{3.2}$$

$$\sigma = \sigma_m + d\sigma/dT\ (T - T_m) \tag{3.3}$$

where ρ_m and σ_m are the density and surface tension at the melting point, and $d\rho/dT$ and $d\sigma/dT$ are the temperature coefficients of density and surface tension, respectively. Table 3.8 presents the comparison of these parameters obtained from MD simulations using both the present potential and the original potential of Ko *et al*. compared to those obtained from experiments.

The temperature in these calculations was varied from 1833 K to 2103 K for Ti and from 1620 K to 1782 K for Ni. In the case of Ti, the comparison of the MD calculated density coefficients, based on the original and the present MEAM potential, and the experimental data reveals a noticeable improvement when using of the present potential; specifically, densities calculated using the present potential show a maximum deviation of less than 1.7% from

experimental data. For Ni, the densities calculated using both the original and present MEAM potential are very close to each other and are in good agreement with the experimental data.

Table 3.8. Surface tension at the melting point, $\sigma_m(mJm^{-2})$; surface tension temperature coefficient, $d\sigma/dT(mJm^{-2}K^{-1})$; density at the melting point, $\rho_m(gcm^{-3})$; and the density temperature coefficient, $d\rho/dT(g\,cm^{-3}\,K^{-1})$, calculated using the present potential in comparison with the original potential and experimental [151-154] results for Ti and Ni

		Ti			Ni		
Property	Coeff.	Exp.	2NN-MEAM (Ko *et al.*)	2NN-MEAM present	Exp.	2NN-MEAM (Ko *et al.*)	2NN-MEAM present
ρ	ρ_m	4.1426 [a]	4.251	4.2049	7.795[b]	7.816	7.819
	$d\rho/dT$	-0.000217 [a]	-0.000091	-0.000141	-0.00066 [b]	-0.00067	-0.00065
σ	σ_m	1.557 [c]	2.15938	2.02	1.7952 [d]	1.15	1.2
	$d\sigma/dT$	-0.156 [c]	-0.04	-0.09	-0.35 [d]	-0.266	-0.303

[a] Reference [151] [b] Reference [152] [c] Reference [153] [d] Reference [154]

The surface tensions are not accurate for either the original or present potential, but the present potentials improves the agreement with experiment. For Ni, the present potential underestimates the surface tension by approximately 35 %, but it still shows an improvement when compared with the 40% discrepancy obtained when using the original potential. In the case of Ti, the discrepancy between the surface tensions calculated based on the present potential and the experiment is about 33%, but it represents a 12% improvement when compared with the results obtained from MD calculations based on the original potential.

3.2.2.3 Temperature-dependent transport properties

Two temperature dependent transport properties: diffusivity and viscosity of the liquid phase were calculated by MD simulation using both the present and original potential by Ko et al. In the temperatures ranges considered, both the diffusion coefficient and viscosity are assumed to have an Arrhenius temperature dependence [155] given by:

$$D = D_0 \exp(-\frac{E_D}{k_B T}) \quad (3.4)$$

$$\eta = \eta_0 \exp(\frac{E_\eta}{k_B T}) \quad (3.5)$$

where, E_D, and E_η are the activation energies for diffusion and viscous flow respectively, and D_0 and η_0 are constants.

Table 3.9 presents the comparison of the parameters entering equations 3.4 and 3.5 as obtained from MD simulations using both the present and the original potential of Ko *et al*. and those obtained from experiments [148, 155] .

The comparison of experimental and MD-calculated diffusivity parameters (pre-exponential factor and activation energy) in the liquid phase shows that there is a considerable improvement when using the present MEAM potential compared to the original potential. Moreover, it should be noted that for Ti the simulation data based on the present potential is very close to data from the ab-initio calculations [156]. For instance, the diffusivity values predicted by ab-initio and our potential at T= 1950 K are 5.0, and 4.82 ($\times 10^{-9}$ m^2/s), respectively. This should be viewed with caution though, since in the case of Ni the ab-initio results [157] for diffusivity parameters are higher than the values reported in simulations using both potentials as well as experimental data. As an example we can point to the diffusivity values of 2.68, and 2.26 ($\times 10^{-9}$ m^2/s) predicted by ab-initio and our potential at T= 1620 K.

Viscosity calculations for Ti when using both the present and original potential are in reasonable agreement with the experimental [148] and ab-initio data [156]. In the case of Ni, the comparison of the MD simulation results based on both potentials with experimental [148] and ab-initio [157] data shows an improvement in the MD-calculated viscosity using the present potential.

Table 3.9. The activation energy for diffusion, $E_D(eV/atom)$, constant coefficient $D_0(\times 10^{-8}cm^2/s)$, activation energy for viscosity, $E_\eta(eV/atom)$, constant coefficient $\eta_0(mPa.s)$ calculated using the present and the original potential by Ko et al. [117] and experimental results[148, 155] for Ti and Ni

		Ti			Ni		
Property	Coeff.	Exp.	2NN-MEAM (Ko *et al.*)	2NN-MEAM present	Exp.	2NN-MEAM (Ko *et al.*)	2NN-MEAM present
D	E_D	0.43 [a]	0.338	0.393	0.47 [a]	0.533	0.498
	D_0	6.56 [a]	4.31	4.98	7.78 [a]	9.011	8.02
η	E_η	0.28 [b]	0.1826	0.24	0.79 [b]	0.427	0.445
	η_0	0.61 [b]	1.015	0.90	0.283 [b]	0.416	0.318

[a] Reference [148, 155] [b] Reference [148]

3.3 Physical properties of Ti-Ni binary system

The Ti-Ni phase diagram contains a few intermetallic solid phases seen in experiments [158-160] and DFT [161-163] calculations. For the equiatomic NiTi composition, there are two important structures, the so-called B2 and B19' crystal structures [121]. The B2 and B19' structures are related to the austenitic and martensitic phases of NiTi, respectively. Other structures, such as B19 and B33 which are experimentally observed under special conditions such in thermal aging or under high-pressure conditions [164], or are predicted by DFT [162], are not considered in this study. The other stable intermetallic compounds are Ni_3Ti and $NiTi_2$ intermetallic compounds which will be investigated as part of the verification of the transferability of the present MEAM potential for the binary system.

In this section, we evaluate the accuracy and transferability of the developed binary potential by comparing a set of calculated material properties with the available experimental and DFT calculated data. The parameters of the potential for Ti-Ni binary system were optimized based

on the experimental data for the phase diagram and enthalpy of mixing in the liquid. The potential was not fitted to the high temperature properties of the solid-solutions, and other liquid phase properties. Instead, these properties are studied to investigate the transferability of the potential.

3.3.1 Solid phase

3.3.1.1 Physical properties of binary compounds at 0 K

For testing the binary Ti-Ni potential, the physical properties of the solid solutions and binary compounds are very important and must be investigated. Table 3.10 lists various physical properties of NiTi (B2 and B19' structures), Ni_3Ti, and $NiTi_2$ intermetallic compounds as obtained from: MD calculations based on the present and the original potential of Ko et al., experimental investigations, and DFT calculations. These results show that the present potential reproduces very well the lattice constants, monoclinic angles, and the formation energies for most compounds. Moreover, the cohesive energies of the B2 and B19' structures calculated from MD simulation follow the same trend as that predicted by DFT calculations. The B19' structure has a lower energy than the B2 structure, which means that at 0 K the B19' structure is energetically more favorable. The lattice parameter and the formation energy for $NiTi_2$ matches very well with the corresponding experimental and DFT values. One shortcoming of the current potential is that, very much like DFT calculations, it gives a relatively poor estimate of the enthalpy of formation of Ni_3Ti when compared with the values obtained from experiments and the MD calculations based on Ko et al. potential.

Table 3.10. Physical properties of Ti-Ni binary compounds at various compositions from experiment data, DFT calculations, and from calculations based on the present 2NN-MEAM potential and the previous MEAM potential by Ko et al. *[117]*. The following properties are listed: the lattice constants a, b, c (Å); the monoclinic angle β (degree); the enthalpy of formation ΔE_f (eV/atom).

Composition	Structure (space group)	property	Experiment	DFT	2NN-MEAM (Ko *et al.* [117])	2NN-MEAM (present)
NiTi	B2 (*P* $m\bar{3}m$)	a	3.016 [a]	3.012 [b], 3.009 [c]	2.99	3.015
		b	4.265 [a]	4.26 [b], 4.255 [c]	4.242	4.264
		c	4.265 [a]	4.26 [b], 4.255 [c]	4.242	4.264
		β	90 [a]	90 [b], 90 [c]	90	90
		ΔE_f	-0.351 [d]	-0.355 [b]	-0.3968	-0.2957
	B19' (*$P2_1/m$*)	a	2.909 [a]	2.945 [b], 2.917 [e]	2.878	2.865
		b	4.114 [a]	4.034 [b], 4.047 [e]	4.129	4.187
		c	4.657 [a]	4.769 [b], 4.780 [e]	4.659	4.616
		β	97.9 [a]	101.8 [b], 100.0 [e]	99.4	97.3
		$E-E_{B2}$		-0.0428 [b], -0.0415 [e]	-0.0341	-0.0329
Ni_3Ti	*DO_{24} ($P6_3/mmc$)*	a	5.101 [f]	5.108 [b]	5.1577	5.175
		c	8.307 [f]	8.337 [b]	8.35	8.366
		ΔE_f	-0.36 [g]	-0.487 [b]	-0.35	-0.266
$NiTi_2$	*$E9_3$ ($F d\bar{3}m$)*	a	11.28 [h]	11.28 [b]	11.3	11.329
		ΔE_f	-0.278 [g]	-0.280 [b]	-0.298	-0.270

[a] Reference [125] [b] Reference [117] [c] Reference [162] [d] Reference [123, 165]
[e] Reference [163] [f] Reference [166] [g] Reference [124] [h] Reference [167]

3.3.1.2 Enthalpy of formation of binary compounds at high temperature

Any potential used in simulation of solidification of binary alloys should also be able to reproduce a reasonable set of properties of both the solid and liquid alloy phases at high temperature. Since there are experimental values for the enthalpy of formation of NiTi, Ni_3Ti, and $NiTi_2$ compounds at 1475, 1202, and 1513 K respectively[160], we performed MD calculations for enthalpy of formation for the three intermetallic compounds at the same temperatures using both the currently developed and the Ko et al. potentials and the results are presented in Table 3.11. The

comparison of the MD-calculated values using the two potentials with the experimental results clearly shows that the current potential is better suited for high temperature calculations. Specifically, while the calculations based on Ko et al. potential overestimate the heat of formation of NiTi by 20%, the calculated value based on the present potential deviates by less than 3% from the experimental value. Even though the present potential results for Ni_3Ti deviate by 28% from the experimental value, this is still better than the results obtained based on the Ko et al. potential which predicts that the Ni_3Ti compound melts at 1513 K. In addition, the only 4% difference between the MD calculated value, based on the present potential, and the experimental results for $NiTi_2$ is significantly smaller than the 16% discrepancy obtained when using the Ko et al. potential.

Table 3.11. The formation energy, ΔE_f (kJ/mol) of binary compounds NiTi (at 1475 K), Ni_3Ti (at 1513 K), and $NiTi_2$ (at 1202 K), from experiments [160] and calculated using the present 2NN MEAM potential and the original MEAM potential by Ko et al. [117].

Composition	Experiment	2NN MEAM (Ko *et al.* [117])	2NN MEAM (present)
NiTi	-34.0	-42.5	-35.0
Ni_3Ti	-42.9	melts	-30.4
$NiTi_2$	-29.3	-34.0	-30.4

3.3.2 Liquid phase

3.3.2.1 Density of liquid binary alloys

The transferability of the binary potential was tested by comparing the density in the liquid phase for a set of five compositions which include $Ni_{25}Ti_{75}$, $Ni_{40}Ti_{60}$, $Ni_{50}Ti_{50,}$ $Ni_{60}Ti_{40}$, and $Ni_{75}Ti_{25}$ with corresponding experimental values [168, 169], As illustrated in Figure 3.1, the density values obtained by using the binary MEAM potential are in very good agreement with the

experiments; the largest discrepancy, which is less than 5%, between the simulation and experimental data was obtained for the $Ni_{60}Ti_{40}$.

3.3.2.2 Enthalpy of mixing

During fitting, we computed liquid binary alloy enthalpies of mixing to ensure reasonable agreement with experiment [81]. The MD simulations were performed in the NPT ensemble starting with a random distribution of the elements in the initial state. All calculations were performed after the system has reached equilibrium, which was determined by monitoring the time variation of the enthalpy. During the equilibration period by using MC we swapped a randomly chosen Ti atom with a randomly chosen Ni atom 500 times after every 2000 MD steps. The system reaches the equilibrium state when the system enthalpy converges to a stationary value and after the equilibration period, MC swapping was turned off. The MD simulations show that the time it takes to reach equilibrium depends on the composition. Specifically, for systems with compositions as small as 5 atom% Ti or as large as 95 atom% Ti, the equilibrium time was found to be about 40 ps; for the concentrations close to the 50 atom% Ti the equilibrium time increases to about 400 ps. After the equilibration, the enthalpy was calculated by averaging over 50 ps simulation time.

In Figure 3.2, we compare the liquid binary alloy enthalpies of mixing at 1800 K and 1980 K with experimental data. The enthalpies of mixing calculated based on the present potential are in good agreement with the experimental data. The minimum values of the enthalpy of mixing obtained from both MD simulations and experiments are located approximately at compositions close to 45 atom % Ti. The agreement between the calculated and experimental values is especially good for the Ni-rich compositions. Overall, the maximum discrepancy between the calculated and experimental values for the Ni-rich and Ti-rich systems are less than about 5% and 16%,

respectively.

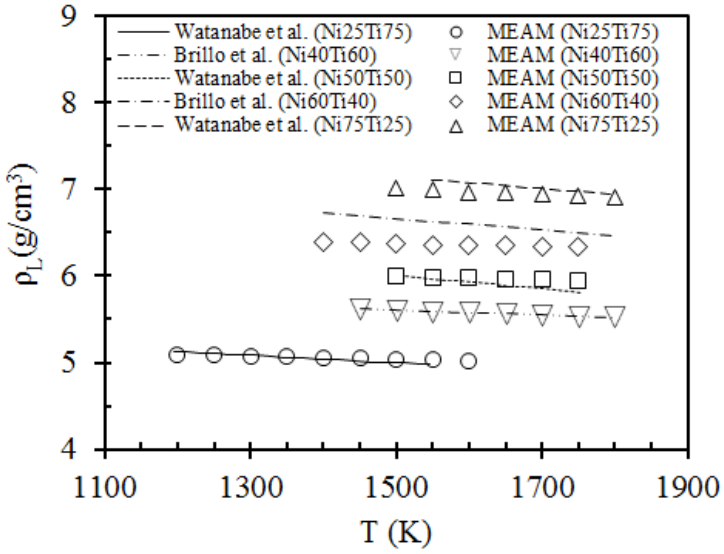

Figure 3.1. Temperature dependence of the liquid density, ρ_L, for $Ni_{25}Ti_{75}$, $Ni_{40}Ti_{60}$, $Ni_{50}Ti_{50}$, $Ni_{65}Ti_{40}$ and $Ni_{75}Ti_{25}$ compositions calculated using the present 2NN-MEAM potential and from experimental data by Watanabe at al. [168] and Brillo et al. [169].

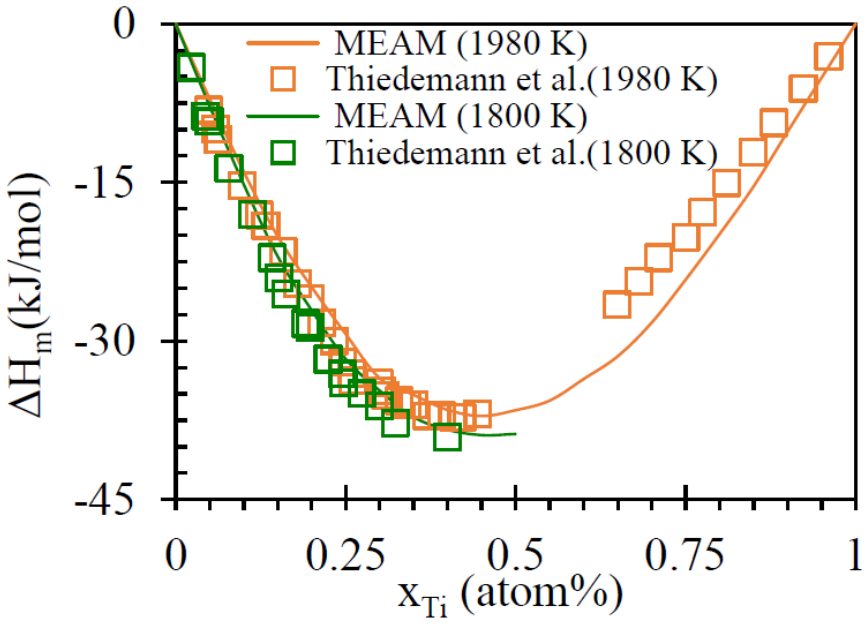

Figure 3.2. Concentration dependence of the enthalpy of mixing, ΔH_m, in liquid Ni-Ti alloys calculated using the present 2NN-MEAM potential and the experiment data by Thiedemann et al. [170]

3.3.3 Crystal-melt phase equilibrium

3.3.3.1 Phase diagram

As part of the optimization process of the parameters describing the potential, in addition to the enthalpy of mixing, we calculated the CM coexistence portions of the phase diagram for Ti-rich and Ni-rich solid solutions. For reference and comparison with the MD calculations, the entire phase diagram was calculated by using CALPHAD (CALculation of PHAse Diagrams) [171]. Specifically, we utilized the commercial software, Thermo-Calc version 4.1 [172], with the TCBIN binary solutions database under atmospheric pressure. The MD calculated portions of the CM coexistence region of the phase diagram for the Ti-rich portion were determined for concentrations ranging from 0 to 15.7 at% Ni for the liquidus line and from 0 to 7.6 at % Ni for solidus line. For the Ni-rich portion the phase diagram the calculations determined the liquidus line for concentrations ranging from 95 to 100 at% Ni.

The calculation of the phase diagram is a two-step process. In the first step, a rough estimation of the phase diagram is obtained and in the second step a more accurate phase diagram is calculated. In the first step, at the target temperature, the starting configuration consists of coexisting solid and liquid phases with an average composition $x_{ave}^{T} = 0.5 \times (x_s^T + x_L^T)$ where x_s^T, and x_L^T are the solid and liquid concentration obtained from the phase diagram generated by Thermo-Calc. The solid-liquid coexistence system was equilibrated for about 3 ns in the NPT ensemble with the temperature of the entire system equal to the target temperature. During the MD simulations, every 5000 MD steps, 1000 attempted swaps of the positions of atoms of different types were performed based on a Metropolis Monte Carlo acceptance criterion. The MC temperature used to determine acceptance was the same as the MD temperature. The simulations were continued until the concentrations of solute in the liquid and solid phases and the solid/liquid

volume fraction remained constant for at least 0.5 ns. For each target temperature, the equilibrium solute concentration in liquid and solid obtained from Thermo-calc can be different from the corresponding concentrations using the MD calculated phase diagram. This results in a different lattice parameter in the solid phase compared to the initial guess, so we first compute the lattice parameter in a separate simulation at the solid concentration obtained from the first step and then use that lattice parameter and the concentrations of solute in the solid and liquid phases as initial guesses for the second coexistence step.

In the second step, the solid-liquid coexistence system was equilibrated for about 3 ns in the $NP_{zz}T$ ensemble with the temperature of the entire system equal to the target temperature and the normal stress in the z-direction, P_{zz}, set to zero. The box sizes in x and y-directions were fixed such that the lattice parameter for the crystalline portion of the system matched the average lattice parameter for the solid phase concentration from the first step which was calculated by equilibrating a 10×10×10 crystal for 50 ps in the NPT ensemble, followed by an additional 300 ps simulation during which the average lattice parameter was determined. Again, the second stage coexistence simulations were continued until the concentrations of solute in the liquid and solid phases and the solid/liquid volume fraction remained constant for at least 0.5 ns.

Figure 3.3 shows the comparison of the Ti-rich and Ni-rich CM coexistence portions of the Ti-Ni phase diagram calculated from the MD simulation using the current potential and those obtained from Thermo-Calc software. As seen from Figure 3.3, the MD simulations reproduce quite accurately the Ni-rich portion of the phase diagram. For the Ti-rich portion and temperatures in the 1550 K to 1943 K range, the solidus and liquidus curves are approximately straight lines and agree with the Thermo-Calc generated phase diagram but the MD liquidus lines deviates from Thermo-Calc in the 1400 K to 1550 K temperature range. In the higher temperature range of 1550

K to 1943 K, the slopes for the solidus line, $m_{S,}$ and liquidus line, $m_{L,}$ derived from the Thermo-Calc calculated phase diagram, were estimated to be equal to 75 K/atom% and 25.7 K/atom%, respectively. The corresponding slopes from the MD calculated phase diagram are m_S = 77.3 K/atom% and m_L = 29.5 K/atom%. For the same temperature range, the partition coefficients from Thermo-Calc and MD-calculated phase diagrams are 0.35 and 0.38 respectively.

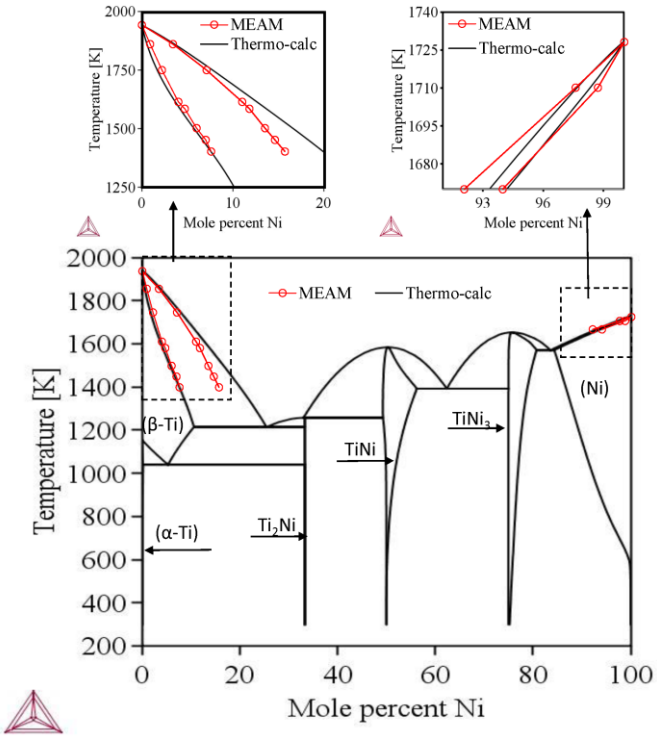

Figure 3.3. The Ti-rich and Ni-rich portions of Ti-Ni phase diagram calculated using the present MEAM potential compared to the phase diagram based on CALPHAD calculations with the Thermo-Calc software [172].

3.4 Conclusion

We developed 2NN MEAM potentials for Ti, Ni, and the Ti-Ni binary systems that improve the crystal-melt (CM) interfacial properties for pure and binary systems and the high temperature portions of the binary system CM equilibrium phase diagram for both the nickel-rich and titanium-rich compositions. The new parameters for pure Ti and Ni were obtained by adjusting

of the parameters of the 2NN-MEAM potentials developed by Ko *et al.* [117] to fit the melting points and latent heats of fusion. The reliability of the potentials for pure Ti and pure Ni were tested by comparison of various physical quantities including structural properties, elastic constants, point-defect properties, surface energies, temperatures and enthalpies of phase transformations, and thermodynamic and dynamic properties of the liquid phases with experimental and DFT data. Most of the 0 K properties are not affected much by the potential modifications, while most of high temperature properties are improved relative to the original potentials. The binary potential was fit to the liquid enthalpies of mixing and the CM portions of the phase diagram in the Ni-rich and Ti-rich regions. The fitted binary potential for Ti-Ni was also tested against various non-fitted properties such as lattice parameters, formation energies of different intermetallic compounds, and the temperature dependence of liquid density at various concentrations. As with pure Ni and Ti, most of the high temperature properties of the binary are improved relative to the original potential. The binary Ti-Ni potential accurately captures the CM coexistence portions of the equilibrium phase diagram on the Ti-rich side from pure Ti down to about 1550 K and on the Ni-rich side and from pure Ni down to about the eutectic temperature of 1577 K.

4 INVESTIGATION OF CRYSTAL-MELT INTERFACE ENERGY AND KINETIC COEFFICIENT BY MOLECULAR DYNAMICS[1]

Many phase field studies show the importance of the effect of crystalline anisotropy on dendrite shape [173] and growth rate [173]. The anisotropy of a pure material can be perturbed by the addition of alloying elements[174]. A major limiting factor of quantitative prediction of microstructure with phase field simulation approach is the scarcity of available experimental data pertining to the crystal-melt interfacial properties and the anisotropy parameters of the materials.

In this chapter, we will use our developed potential to calculate the crystal-melt interface free energy and kinetic coefficient during the solidification.

4.1 Crystal-melt Interface free energy

4.1.1 MD simulation methodology

The starting configuration of MD simulation consists of a periodic system with dimensions of 80×4×220 bcc unit cells. The central half of the system is melted in the NVT ensemble at 2,600 K, while the remaining half of the atoms are fixed. For pure material, the resulting solid-liquid coexistence system is equilibrated at the melting point for 1 ns in the $NP_{zz}T$ ensemble, using an extended system thermostat and barostat. Assuming the melting point is accurate, one can assume that the system is now close to equilibrium. The positions of the two crystal-melt interfaces are then obtained from an NPH simulation lasting for 240 ps. During this step, the system configuration is saved every 0.2 ps for later analysis of the interface fluctuations.

[1] Part of this chapter has been published in *Computational material science*, reprinted with the permission of the publisher. [S. Kavousi, B.R. Novak, M.A. Zaeem, D. Moldovan, Combined molecular dynamics and phase field simulation investigations of crystal-melt interfacial properties and dendritic solidification of highly undercooled titanium, Computational Materials Science, 163 (2019) 218-229].

To obtain the interface positions, $h(x)$, an order parameter is needed to allow us to distinguish the solid from the liquid. In the case of the kinetic coefficient calculations of pure material, only the average interface position was needed and therefore the choice of order parameter was not so critical. However, for the calculation of the interfacial free energy in addition to the average interface position one also needs to know the local interface position and, as such, the order parameter must be chosen more carefully. In this study we used the order parameter introduced by Sun et al. [103]. To start, for each atom, j, the order parameter, β_j, is calculated from the difference of the vectors to 1NN and 2NN atoms to those same vectors in a perfect crystal, shown as pc, and is given by:

$$\beta_j = \frac{1}{14}\sum_i \left|\vec{r_i} - \overrightarrow{r_{pc}}\right|^2 \tag{4.1}$$

The values of this order parameter still exhibit large fluctuations which makes the determination of interface position difficult. To solve this issue, the smoothed order parameter, introduced by Asadi et al. [93], was used in this work:

$$\psi(x,z) = \frac{\sum_i w_d r_i \beta_i}{\sum_i w_d r_i} \tag{4.2}$$

where $w_d = [1-(r_i/d)^2]^2$, $r_i = \sqrt{(x_i - x)^2 + (z_i - z)^2}$ and d is a smoothing distance. Large smoothing distances lead to inaccurate results and small smoothing distances do not sufficiently dampen the fluctuations. Note that ψ is obtained from a smoothing over cylinders perpendicular to the y direction, so it does not need to be calculated for each atom, only on a grid in the $x-z$ plane. We use a grid spacing of $0.5a$ and a smoothing distance of $d = 2.5a$, where a is the lattice parameter. Figure 4.1 shows ψ for one value of x and β for atoms within $0.25a$ of the same value of x along the z direction. The average values of ψ in the solid and liquid phases are estimated to be 0.038 and 0.135 respectively. The interface location is taken to be where ψ is halfway between those values, 0.086. Figure 4.1 shows that the interface positions can be easily determined using

the ψ order parameter.Once h(x) for each interface was calculated, the Fourier transform was applied and amplitude of each Fourier mode was determined. The amplitudes of the Fourier modes for all times were then squared and averaged to obtain $\langle|A(k)|^2\rangle$. The slope of $k_BT/(bW\langle|A(k)|^2\rangle)$ versus k^2 for small k yields the stiffness value.

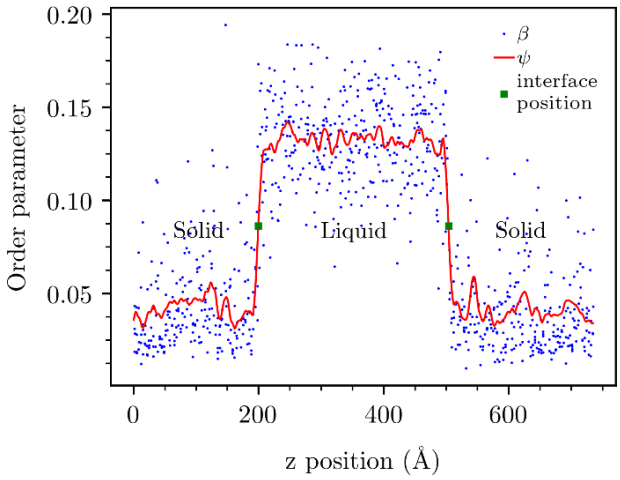

Figure 4.1. The local order parameter, ψ, as a function of z for the (001) oriented interface for one value of x and β for atoms within 0.25a of that value of x

The simulation methodology for alloys is a little bit different than the pure material. For alloys, we used hybrid NPT MD/MC to equilibrate the concentrations in the crystal and melt phases in alloys for 1 ns by using MC to attempt to swap a randomly chosen Ti atom with a randomly chosen Ni atom 500 times after every 5000 MD steps. After this equilibration period, MC swapping was turned off.

4.1.2 Results and discussion

Figure 4.2 shows the variation of $k_BT/bW< |A(k)|^2 >$ versus k^2 for three different crystal-melt interface orientations obtained from MD simulations of Ti-4 atom% Ni alloy using our developed MEAM potential. The slope of the solid line is the stiffness value for that orientation. The data shows deviation from linearity for large values of k^2, and therefore there is

a question of how much data at large k^2 value one should use for fitting. There is no precise way to decide on this issue, therefore in our procedure we keep adding points with higher k until the R^2 for the fit falls below 0.95 which is similar to [93] where the criterion used was the norm of the residuals being greater than 3. Equation suggests that the stiffness value is only a function of interface normal orientation. In MD simulations, two systems with $\{111\}$ orientations in interface normal direction are studied. In one of the systems the x direction was chosen to be $\langle 1\bar{1}0\rangle$ and in the other it was $\langle 11\bar{2}\rangle$. For a crystal with cubic symmetry, the interfacial free energy as a function of orientation can be represented by the following equation:

$$\gamma = \gamma_0 \left[1 + \delta_1 \left(\sum_{i=1}^{3} n_i^4 - \frac{3}{5}\right) + \delta_2 (3 \sum_{i=1}^{3} n_i^4 + 66 n_1^2 n_2^2 n_3^2 - 17/7)\right] \quad (4.3)$$

where γ_0 is the average interfacial free energy, δ_1 and δ_2 are the anisotropy parameters, and n_i are the components of the unit vector, $\hat{n}$, normal to the interface plane [93]. Table 4.1 contains the calculated interface stiffness using the capillary fluctuation method for Ti-4atom%Ni. The parameters from equation were obtained by a best fit to the MD data are γ_0=172±3 mJ/m^2, δ_1=0.024, and δ_2= -0.0048.

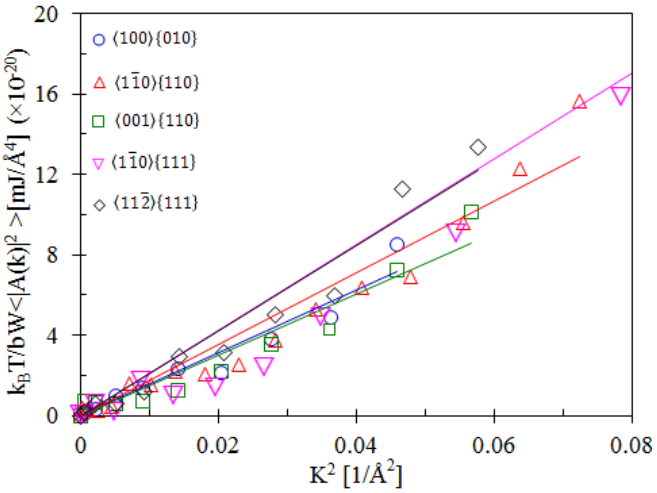

Figure 4.2. The variation of $k_B T/bW < |A(k)|^2 >$ versus k2 for different orientations as obtained from MD simulation Ti- 4 atom% Ni. The solid lines are linear fits where the color of the line is the same as the symbols for the data it was fit to.

Table 4.1. The crystal melt interface stiffness for various interface orientations as given by equation 4.3 and obtained from MD simulations.

Interface orientation	Interface stiffness [mJ/m^2]	
	Expression (equation 4.3)	MD simulations
⟨100⟩ {001}	$\gamma_0 [1- (18/5) \delta_1 - (80/7) \delta_2]$	156
⟨1$\bar{1}$0⟩ {110}	$\gamma_0 [1+ (39/10) \delta_1 + (155/14) \delta_2]$	179
⟨001⟩ {110}	$\gamma_0 [1- (21/10) \delta_1 + (365/14) \delta_2]$	177
⟨1$\bar{1}$0⟩ {111}	$\gamma_0 [1+ (12/5) \delta_1 - (1280/63) \delta_2]$	193
⟨11$\bar{2}$⟩ {111}	$\gamma_0 [1+ (12/5) \delta_1 - (1280/63) \delta_2]$	186

Table 4.2 summarizes the parameters entering equation obtained by a best fit to the MD data of pure Ti and Ti alloyed with 2 and 4 atom% Ni. As a validation of our interfacial free energy simulations, the model of Kaptay (equation 16 in [175]) for pure Ti with the enthalpy of fusion and latent heat obtained using our potential gives an almost identical result for γ_0 of 199 mJ/m^2. The value for pure Ti is near the upper range of experimental values.[176] The results show that the addition of Ni to the pure alloy decreases the average interfacial free energy, γ_0, but increases the magnitude of both anisotropy parameters, δ_1 and δ_2. For all three studied cases $\delta_1 > 0$ and $\delta_2 < 0$, which means that either the <100> or <110> oriented dendrites will be produced. As δ_1 decreases, the dendrites would prefer to grow in <110> direction rather than <100>. We should note that although the results are over a very limited concentration range, our δ_1 increased with decreasing values of the equilibrium partition coefficient (increasing concentration for our data) while for recently published results for Fe-Cr [177] δ_1 decreased strongly with decreasing equilibrium partition coefficient and is even negative for one concentration. The reason for this difference is not clear but may simply indicate that the behavior of the anisotropy is strongly dependent on the crystal structure of the alloy.

Table 4.2. The average CM interface free energy, γ_0 (mJ/m2), and anisotropy parameters, $\delta 1$ and $\delta 2$, defined in equation for Ti-X atom% Ni (X = 0, 2, 4). The numbers in the parentheses are the uncertainties of the last significant digits

	Pure Ti	Ti-2 atom% Ni	Ti-4 atom% Ni
γ_0	198(3)	186(6)	172(3)
δ_1	0.021(5)	0.022(5)	0.024(6)
δ_2	-0.0007(7)	-0.0037(2)	-0.0048(9)

4.2 Kinetics of rapid solidification

4.2.1 Pure Ti

4.2.1.1 MD simulation methodology

The MD simulation approaches used for calculation of the kinetic coefficient of solid-liquid interfaces can be divided into equilibrium and non-equilibrium methodologies [4]. The equilibrium methods rely on the analysis of the fluctuations of the solid-liquid interface through the capillary fluctuation method [4]. The non-equilibrium MD methods are classified as either forced velocity [101, 102] or free solidification [102] approaches. In this study the kinetic coefficient was calculated by using a free solidification method [102]. Under the MD simulation conditions, the solid-liquid interface, on average, remains planar during the solidification and therefore according to Gibbs-Thomson relation (see Eq. (2.8)) the slope of the solidification velocity as function of temperature gives the kinetic coefficient. Due to the latent heat generated during solidification, the interface region will be at a higher temperature if only a single global thermostat is used. To eliminate the temperature gradients and avoid the calculation of interface temperature we used a system of multiple local thermostats applied independently to thin slabs aligned parallel to the plane of the solidification interface. This approach was proven to provide

nearly identical results to those obtained by using a global thermostat and the actual interface temperature calculation [102].

Calculation of the kinetic coefficient requires determination of the velocity of the crystal-melt interface at different undercoolings, but initially an equilibrated solid-liquid coexistence system at the melting temperature is needed. These sets of calculations are performed on a potential by Ko et al. [117] where the melting point is 1716 K. For a (001) oriented solidification interface, shown in Figure 4.3, the whole simulation system was initialized on a lattice consisting of 14×14×69 bcc unit cells (27,048 atoms) of approximate dimensions 46×46×230 Å. The simulation systems with different orientations of the crystal-melt interface, (110) and (111), have similar dimensions and number of atoms. Next, the system was equilibrated for 50 ps as a solid under the NPT ensemble where P = 0, followed by an additional 300 ps simulation during which the mean lattice parameter was determined. To create the crystal-liquid coexistence system, the central three quarters portion of the simulation box along the z-direction (see Figure 4.3) was melted by heating it at 2,600 K for about 50 ps under the NVT ensemble while the other quarter of the system remained in the original (solid) state. This lead to the creation of two crystal-melt interfaces. Finally, the equilibrated solid-liquid coexistence system was obtained by a 100 ps MD simulation under $NP_{zz}T$ conditions in which the temperature of the entire system is set to the melting temperature and the normal stress in the z direction, P_{zz}, is zero. The box sizes in the x and y directions, after they were adjusted to the values determined by the average lattice parameter for the melting temperature, were maintained fixed. An additional 100 ps NPT simulation was used to obtain the equilibrated solid-liquid coexistence configurations that were used as the starting configurations for non-equilibrium solidification.

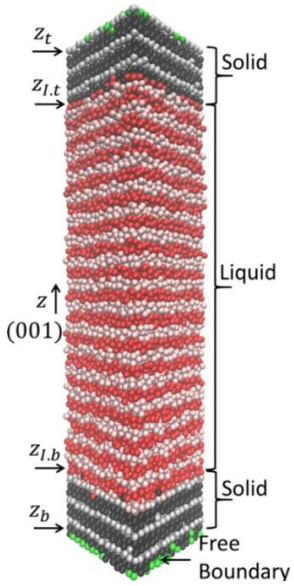

Figure 4.3. The starting configuration of the system used for the nonequilibrium MD simulations of solidification of pure titanium. Red/pink and dark gray/light gray regions are located in liquid and solid phases respectively. Alternating dark/light colors are used to clearly indicate the adjacent slabs that are thermostated independently. The green atoms are boundary atoms which were restrained to have an average force of zero in the x and y directions.

Starting from the equilibrated solid-liquid coexistence system, the kinetic coefficient is calculated from the investigation of the variation of the crystal-melt interface velocity with the applied undercooling. For these, the values of the lattice parameter for various undercooling temperatures were needed. These were obtained from a set of separate MD simulations of the solid at the corresponding temperatures similar to those performed at the melting point but with a smaller box size of only 13×13×13 unit cells (4394 atoms). Starting from an equilibrated solid-liquid coexistence configuration, the velocities of all atoms are scaled down to obtain the desired temperature below the melting point. |The boundary conditions in the z-direction are changed from periodic to free boundaries, the barostat is turned off, and the box sizes and atom positions are scaled in the x- and y-directions (the interface plane) such that the solid regions have the lattice parameter appropriate for the undercooled temperature. The solidification step is effectively run

under conditions of constant normal stress due to the free boundaries (P_{zz} = 0) and constant temperature where the undercooled temperature is maintained by using the multiple thermostats approach in which the simulation system is divided along the z direction into a set of slab regions parallel to the interface and each slab is independently thermostatted. The free boundaries along the z-direction are required in order to be able to use multiple regional thermostats. Surface melting was observed at the free boundaries, especially for small undercoolings. To prevent surface melting, the atoms located in the two atomic planes adjacent to the free boundaries were restrained such that the average forces in the x and y directions on those groups of atoms were set to zero and the temperature in these regions was maintained to the desired undercooling by applying a Langevin thermostat with a damping parameter of 0.1 ps only in the z direction. The thickness of all of the other regional thermostats was set to 5.0 Å and velocity rescaling was used whenever the temperature deviated more than 1 K from the target temperature. Ten independent solidification simulations were run starting from different initial coexistence configurations to determine the uncertainty in interface velocity for each undercooling.

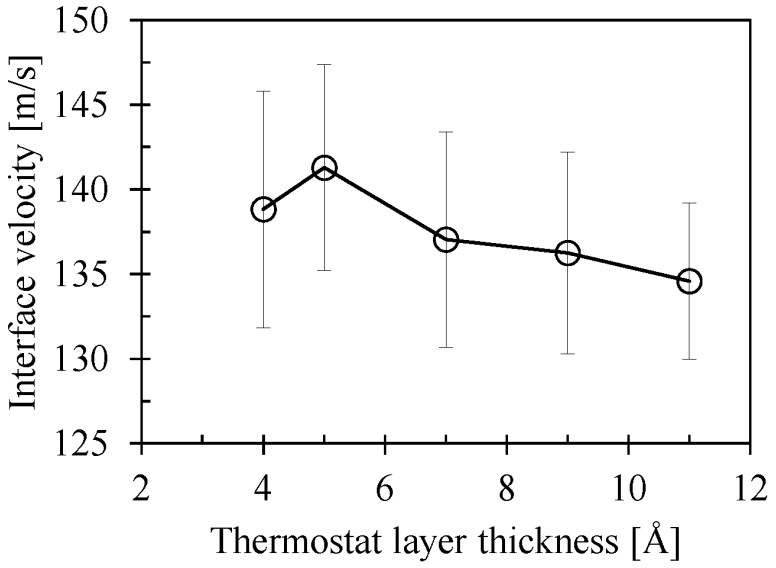

Figure 4.4. Crystal-melt interface velocity as a function of thermostat bin thickness with 200 K undercooling. Error bars represent 95% confidence intervals.

The selection of the optimum thermostats bin thickness was based on the analysis of the variation of crystal-melt interfacial velocity with the bin thickness for a given temperature undercooling. Figure 4.4 shows that the decrease of bin thickness leads to an increase of interface velocity and for a 200K undercooling it reaches a plateau for bin thickness less than 5 Å.

The velocity of the interface was calculated by using two methodologies. The so-called indirect method relies on the relationship between interface velocity and the average slope of the variation of the total potential energy with time during a steady state solidification simulation at a given undercooling temperature T and is given by

$$v_{int} = \frac{1}{2AL}\frac{dE}{dt} \tag{4.4}$$

where v_{int} is the interface velocity, A is the area of the interface, E is the total interatomic potential energy of the system. L is latent heat per volume of solid, $\langle V_{sol} \rangle$, and can be calculated as:

$$L = \frac{\langle H_{liq} \rangle - \langle H_{sol} \rangle}{\langle V_{sol} \rangle} \tag{4.5}$$

where $\langle H_{sol} \rangle$ and $\langle H_{liq} \rangle$ are the enthalpies of solid and liquid respectively at the simulation undercooling temperature. The interface velocity is also obtained by direct tracking of the interface position as function of time and using

$$v_{int} = \frac{1}{2}\left[\frac{d(d_I)}{dt} - \frac{d(d_{Sys})}{dt}\right] \tag{4.6}$$

$d_I = z_{I,t} - z_{I,b}$ and $d_{Sys} = z_t - z_b$, where $z_{I,t}$ and $z_{I,b}$ are the positions of the top and bottom interfaces and z_t and z_b are the positions of the upper and lower solid layers, see Figure 4.3. Note that z_t and z_b change due to the volume change of solidification which must be accounted for when calculating the interface velocity. The time to reach steady state solidification is taken as the time to create solid with a 12 Å depth or about 3 layers at each interface which is sufficient so that the calculated velocity is no longer dependent on starting time.

Obtaining $z_{I,t}$ and $z_{I,b}$ requires use of an order parameter whose average value is clearly different in the liquid and solid phases. For convenience we use the centrosymmetry parameter, CS, based on 12 nearest neighbors, which is calculated for each atom in the system [178]. Twelve nearest neighbors is close to the number in the liquid phase and gave a larger difference between liquid and solid than the 8 nearest neighbors typically used for the bcc crystal. Although the centrosymmetry parameter fluctuates, the mean values in the liquid and solid phases are clearly different as shown in Figure 4.5. To obtain the interface positions, the fitting of error function to CS is used:

$$CS_{fit} = \begin{cases} 0.5\left(\langle CS_{sol}\rangle + \langle CS_{liq}\rangle + \left(\langle CS_{sol}\rangle - \langle CS_{liq}\rangle\right) erf\left[\frac{z-z_{I,t}}{\sigma\sqrt{2}}\right]\right), & z_{center} < z < z_{upper} \\ 0.5\left(\langle CS_{sol}\rangle + \langle CS_{liq}\rangle + \left(\langle CS_{sol}\rangle - \langle CS_{liq}\rangle\right) erf\left[\frac{z-z_{I,b}}{\sigma\sqrt{2}}\right]\right), & z_{lower} < z < z_{center} \end{cases} \quad (4.7)$$

$$z_{center} = 0.5(z_t - z_b) + z_b, \quad (4.8)$$

$$z_{upper} = 0.95(z_t - z_b) + z_b \quad (4.9)$$

$$z_{lower} = 0.05(z_t - z_b) + z_b \quad (4.10)$$

Although $\langle CS_{sol}\rangle$ and $\langle CS_{liq}\rangle$ can be obtained from averages by separate bulk solid and liquid simulations, we consider them to be adjustable parameters along with $z_{I,t}$, $z_{I,b}$, and σ. The fitting is performed using the *lmfit* python package [179] during the simulation at 0.375 ps intervals by utilizing the ability of LAMMPS [126] to use python functions. This feature also allows the simulations to be terminated when the distance between interfaces is less than 50 Å.

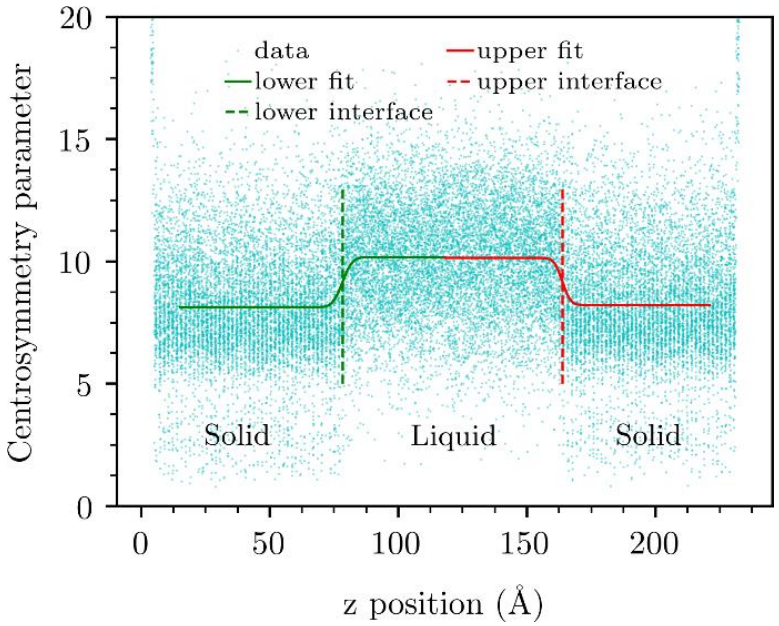

Figure 4.5. Variation of the centrosymmetry parameter along the z direction (the solidification direction) at a given time during a MD simulation of the solidification in a crystal-melt coexisting system. The solid green and red lines depict the error function fit of the order parameter around the lower and upper interface respectively. The dashed green and vertical lines indicate the current location of the two crystal melt interfaces.

4.2.1.2 Results

Figure 4.6 shows the MD simulation results for interface velocity versus undercooling temperature for different interface orientations where the interface velocity was obtained using both direct (equation 4.6) and indirect (equation 4.4) methods. Due to the periodic boundary conditions, the interface is planar on average. Therefore, based on the Gibbs-Thomson equation, we expect a linear relationship between interface velocity and undercooling temperature. The kinetic coefficient is given by the slope of the velocity-undercooling curve.

For a crystal with cubic symmetry, the kinetic coefficient as a function of interface orientation is given by:

$$\frac{1}{\mu(\hat{n})} = \frac{1}{\mu_0}(1 + 3\varepsilon_k - 4\varepsilon_k \sum_{i=1}^{3} n_i^4) \tag{4.11}$$

where n_i are the components of the unit vector, $\hat{n}$, normal to the interface plane, μ_0 is the average kinetic coefficient, and ε_k is the anisotropy parameter [91].

Table 4.3 summarizes the information about the orientations, the kinetic coefficient expressions as given by equation 4.11, and the calculated values from MD simulations. < > denotes the interface in-plane crystallographic orientation in the x direction and { } denotes the orientation characterized by the normal to the crystallographic plane parallel to the interface. For crystals with cubic symmetry, only the crystal orientation in the interface normal interface direction should affect the kinetic coefficient. The MD results proved that this is indeed true as evident from the results obtained for $\langle 1\bar{1}0 \rangle \{110\}$ and $\langle 001 \rangle \{110\}$ orientations for which the kinetic coefficient differ by only about 1%. Direct and indirect calculation of interface velocity gives approximately the same results, but the indirect method gives consistently lower kinetic coefficients.

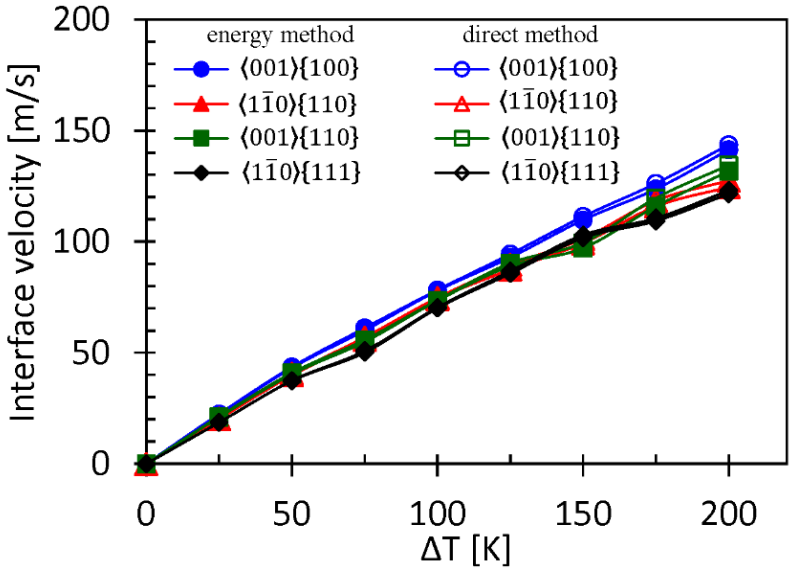

Figure 4.6. The interface velocity versus undercooling temperature from MD simulations of titanium obtained using two different methods. Four different interface orientations were considered.

Table 4.3. The crystal melt interface kinetic coefficient for various interface orientations as given by equation 4.11 and MD simulations

Interface orientation	Kinetic coefficient [m/(s-K)]		
	Expression (Eq. 4.11)	Direct method	Indirect method
$\langle 001 \rangle \{100\}$	$\mu_{001} = \mu_0/(1-\varepsilon_k)$	0.74	0.729
$\langle 1\bar{1}0 \rangle \{110\}$	$\mu_{110} = \mu_0/(1+\varepsilon_k)$	0.6839	0.6675
$\langle 001 \rangle \{110\}$	$\mu_{110} = \mu_0/(1+\varepsilon_k)$	0.6914	0.6767
$\langle 1\bar{1}0 \rangle \{111\}$	$\mu_{111} = \mu_0/(1+1.667\varepsilon_k)$	0.6542	0.6469

Using the results from MD calculations and equation 4.11 one can calculate the mean kinetic coefficient and anisotropy. The direct method for obtaining interface velocities gives ε_k = 0.037 and μ_0 = 0.71 m/(s-K) and the indirect method gives ε_k = 0.04 and μ_0 = 0.7 m/(s-K). The values for the parameters μ_0 and ε_k were obtained without using the data for $\langle 1\bar{1}0 \rangle \{111\}$ orientation and therefore this can instead be used as a check. Specifically, the values of μ_{111}, obtained by using μ_0 and ε_k, are 0.669 m/(s-K) and 0.656 m/(s-K) for the direct and indirect methods, respectively. These values are reasonably close to the simulation values.

4.2.2 Ti-Ni alloys

4.2.2.1 MD simulation methodology

4.2.2.1.1 SGC simulations

Following are the details of the SGC simulations. It is used to obtain the equilibrium crystal-melt phase diagram needed for the kinetic coefficient calculation using equation (2.61), and also estimation of ΔG_{DF} and ΔG_D needed for the interface mobility and drag constant calculations. For SGC, we use a hybrid molecular dynamics/Monte Carlo (MD/MC) method where atom type swap attempts are alternated with MD simulation. Since we are interested in the Ti rich region of the phase diagram, pure Ti is used as the reference. Ti in the liquid and solid phases (bcc)

was simulated at 0 bar pressure at 1942.65 (melting point), 1860, 1749, and 1613 K with equilibration times of 50 ps and production times of 300 ps. Liquid was obtained by melting a bcc lattice at 3000 K and scaling velocities down to obtain the desired temperature prior to equilibration. Mean enthalpies obtained from these simulations were used to calculate $\Delta G(T,0)$ using equation (2.55). The SGC simulations were started from pure Ti in the liquid or solid phase at the desired temperatures below the melting point. The time step was 2 fs, 200 swaps were attempted every 200 steps, the temperature used to determine acceptance of swaps was the same as the temperature for the MD thermostat, the equilibration time was 75 ps, and the production time used to obtain average concentrations was 375 ps. The system size was 1458 atoms which was deemed large enough since it gave results within uncertainty of an even smaller system with only 1024 atoms. For the purpose of calculating free energies using equation (2.56) and for interpolation, we fit the excess chemical potential difference to a fourth order polynomial as in [99]. Initially, a set of 7 or 8 chemical potential differences spaced by 0.05 eV were chosen. The one with the largest magnitude was chosen to get a solid mole fraction of less than 0.005 using trial and error by running a few short simulations. Once the first set of simulations completed, the first estimate of the equilibrium value of the chemical potential, $\Delta\mu_{eq}$, was obtained by solving equation (2.57) after fitting the grand potentials with a cubic interpolating function. Then two more semi-grand ensemble simulations were run with $\Delta\mu=\Delta\mu_{eq}$, equation (2.57) was solved to give a new estimate for $\Delta\mu_{eq}$, and these two steps were repeated a few times until the mean concentrations in the liquid and solid on subsequent iterations were within uncertainty of each other.

4.2.2.1.2 Solidification simulations

To study the velocity-dependent non-equilibrium partition coefficient to compare to the solute trapping models in equation (2.14) and equation (2.15), we should first obtain the interface

mobility using equation (2.14), estimate the drag coefficient, and calculate the kinetic coefficient using equation (2.61). In this study, the interface velocities and partition coefficients are obtained from MD simulations using a non-equilibrium free solidification method.[4, 101, 180]. The driving force for performing the free solidification can be obtained either by reducing the temperature of an equilibrium system (undercooling) at a target concentration or reducing the liquid composition from the equilibrium value at a target temperature. In our simulations, we used the second method and therefore the interface temperature are equal to the interface temperature and it is maintained at a constant value by using the multiple thermostats approach [180].

Following are the details of the free solidification simulations. The orthogonal directions parallel to the interface plane are defined as x and y, and the direction normal to interface is referred as z, as shown in Figure 4.7. The simulation box dimension is much larger in the interface normal direction to ensure, even for very large solidification velocities, we could obtain a period of steady state solidification. The lattice was initially populated with all Ti atoms, and then random Ti atoms were replaced by Ni atoms to reach the desired equilibrium solidus concentration at the target temperature. Next, the system was equilibrated for 80 ps, as a solid, under the NPT ensemble where P = 0, followed by an additional 200 ps simulation during which the mean lattice parameter was determined. The central three quarters of the simulation box along the z-direction was melted by heating up to 3000 K for about 40 ps under the NVT ensemble, while keeping the rest of the atoms fixed. Then, the box sizes in x and y directions were scaled so that the remaining crystal had a lattice constant corresponding to the mean value of the solid calculated in the previous step. The systems then had crystal and melt in coexistence with two crystal-melt interfaces. To maintain the interface temperature at the desired value during solidification, we used multiple thermostats, shown by different shades in Figure 4.7. Fifty independent thermostats were implemented in all

simulation systems leading to slab depths of about 5.5 Å, and velocity rescaling was used in each slab when the temperature in the slab deviated from the target by more than 1 K. Using multiple regional thermostats requires setting free boundaries along the z-direction, while the boundary conditions in the x and y directions are still periodic. To prevent surface melting, the average forces in the x and y directions on the atoms located in the two atomic planes adjacent to the free boundaries were set to zero and the temperature in these regions was maintained to the desired temperature by applying a Langevin thermostat with a damping parameter of 0.1 ps only in the z-direction [14].

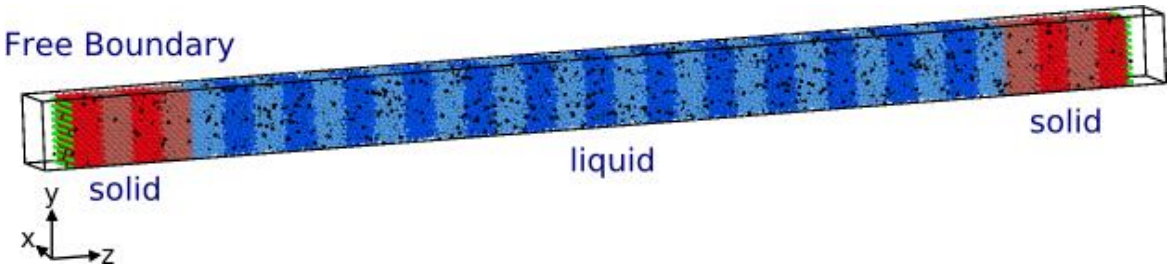

Figure 4.7. An initial configuration of the atoms used in a simulation of solidification. Dark red/light red and dark blue/light blue regions indicate the solid and liquid phases, respectively. Alternating dark/light colors are used to indicate the slabs that are thermostatted independently. The green atoms are boundary atoms which were restrained to have an average force of zero in the x and y directions to prevent surface melting. The atoms marked in black are the Ni solute atoms.

As mentioned previously, the driving force for solidification of the system is the deviation of solute concentration in the melt from the equilibrium liquidus concentration at the target temperature. So, for each desired concentration of the melt, the simulation system is generated by adjusting the Ni concentration in the liquid phase to the target value by randomly substituting some Ti atoms in the melted region with Ni atoms. To obtain accurate partition coefficients, N_{MD} independent solidification simulations starting from different initial configurations were performed. Using multiple simulations is particularly important for high velocities where simulation times are very short. It also allows for a simple estimation of the uncertainty for each

driving force. The N_{MD} starting configurations were generated during a simulation in the NVT ensemble on the liquid phase at the target temperature, and writing the trajectory file every 20 psec. The solidification step is effectively run under conditions of constant normal stress due to the free boundaries ($P_{zz} = 0$), constant interface area, and constant temperature. The solidification simulations were repeated for different temperatures with multiple starting liquid concentrations at each temperature. Additionally, the simulations at each of these states were repeated for systems with different orientations of the crystal-melt interface; (100), (110) and (111). For (100) interface normal orientations, the simulation systems were initialized on a lattice with 10×10×160 bcc unit cells. For the other orientations, the system sizes were modified to have approximately the same number of atoms and simulation box size.

4.2.2.1.3 Interface determination and concentration profiles

Kinetic coefficient and interface mobility calculations require gathering various information, such as solute concentration profile across the interface, the interface velocity, from the free solidification simulations by post processing the trajectory files. The first step is the determination the interface that is performed using a local structure order parameter. The methodology and definition of order parameter used is similar to the one discussed the literature [14, 180-182]. The only difference with the literature is that in previous works, the interface was considered quasi-1D and the order parameter was smoothened over cylinders perpendicular to the y-direction. While in this study we consider the interface to be two-dimensional, and in the smoothing step, we consider the spherical cutoff with the radius of a 2.5 lattice parameter [14]. Although the average curvature of the interface is zero, the instantaneous, local curvature is not zero. The interface velocity is obtained from the average interface positions in the z-direction as a function of time.

Once the interface position was defined, we performed binning on more than 10Å into either solid or liquid side of the interface, and counted the number solute and solvent atoms in each bin. Figure 4.8 demonstrates the bins used in this study to obtain concentrations near a lower interface for a single frame. Instead of box shaped bins with rectangular cross section, the cross section of the bins we used in this study was in the shape of the instantaneous topography of the interface, as shown by the upper surface of Figure 4.8, and the bins were equally spaced in the z-direction. The width of each bin (z-direction) was 2.865 Å, which is about the diameter of a Ti atom and to get better spatial resolution, overlapping bins were used such that lower bin edges were spaced by 0.4775 Å. For each time frame, the solute concentration profile can be obtained from the ratio of the number of solute atoms to the total atoms within each bin.

Estimating the partition coefficient requires defining the solidus and liquidus concentrations across interface; this becomes tricky in high solidification velocities, where both the solid and liquid concentrations are both small and close to each other. For the slower solidifications, the partition coefficient is estimated by $= 1/2N_{MD} \sum_{i=1}^{2N_{MD}} C_s/C_L$.

Estimating the partition coefficient requires defining the solidus and liquidus concentrations across interface; this becomes tricky in high solidification velocities. Partition coefficient is estimated by $= 1/2N_{MD} \sum_{i=1}^{2N_{MD}} k_i$, where k_i is the average partition coefficient of each interface. For the slower solidifications, there is a considerable gap between the liquidus and solidus concentrations and the fluctuations of concentrations are negligible in comparison with their absolute values. So, k_i can be estimated as the average concentration of solute far from interface on the solid side to the maximum of concentrations on the liquid side of the interface. At high solidification velocities, both the solid and liquid concentrations are small and very close to each other, so the fluctuations of the concentration effect the partition coefficient estimatios and

we need more accurate determination of solidus and liquidus concentrations. Thus, during the steady state rapid solidification, the approximate position of the maximum concentration is estimated by the average concentration profile. For each time frame, the reciprocal of solute concentration of the corresponding bin to its concentration when the whole bin is solidified, is known partition coefficient of that time frame, and by averaging them over the steady state period one can estimate k_i.

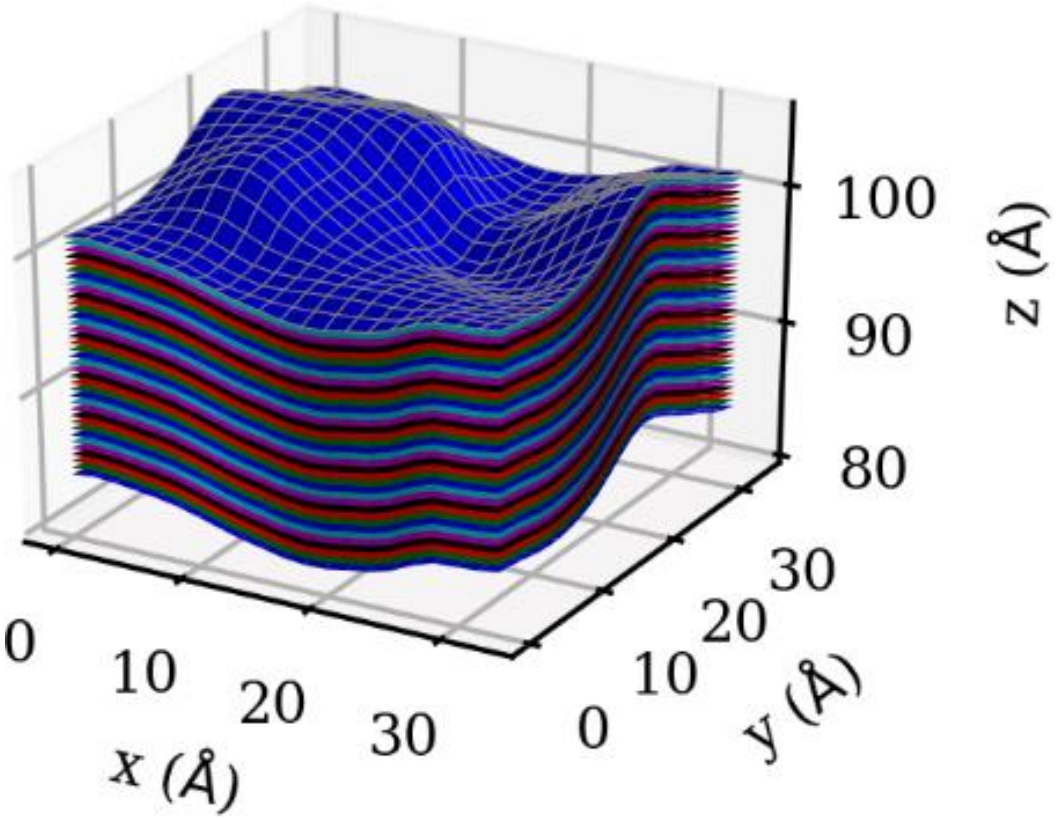

Figure 4.8. Visualization of the lower bin edges used to obtain concentrations near a lower interface for 1 frame. The upper surface represents the instantaneous topography of the interface. Bins edges are constructed by shifting the surface defining the interface such that all bin edges have the same topography as the interface. Bin widths were 2.865 Å and overlapping bins were used such that lower bin edges were spaced by 0.4775 Å. The binned region had a depth of 7 atoms = 20.055 Å leading to 37 bins, and the interface was in the center of that region. Different colors are used to represent these overlapping bins; the region between the lowest blue surface and the second lowest blue surface is the first bin, the region between the lowest green surface and the second lowest green surface is the second bin, etc.

Knowing the CM interface velocity and concentration profile alongside the drag coefficient calculated previously, we could use equation (2.61) to estimate the kinetic coefficient. Figure 4.9 graphically summarizes the workflow of the kinetic coefficient calculations.

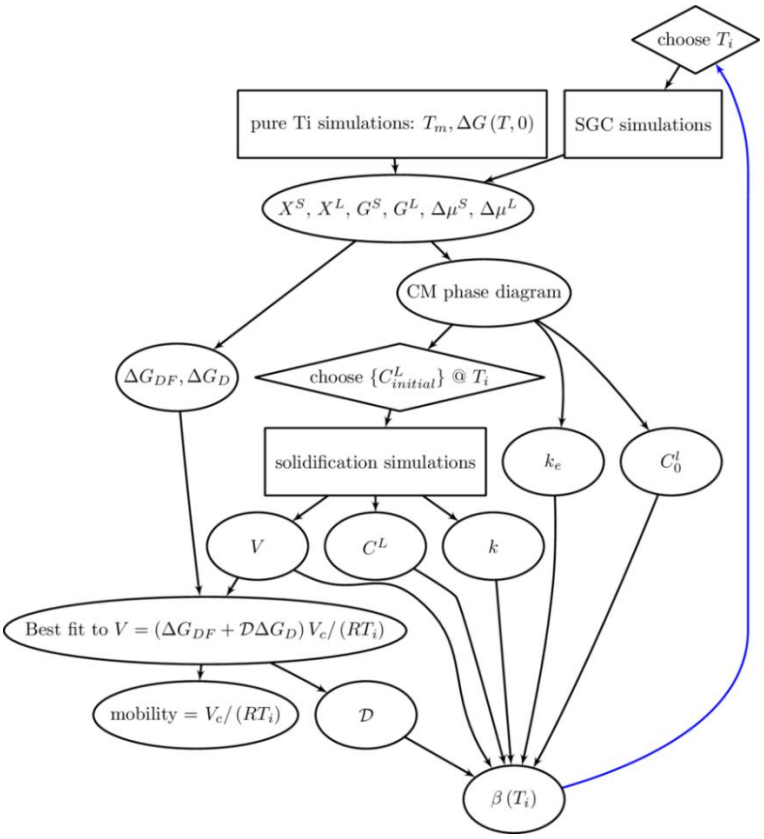

Figure 4.9. Workflow for calculation of the kinetic coefficient.

4.2.2.2 Results

The results are divided into three main subsections. In the first part, the calculations of kinetic coefficient is explained. In the second subsection, we study how the interface width changes by velocity, where two different definitions of interface width, based on either concentration or structure, is used. Finally, the atomistic simulation data are compared with the solute trapping models to find the model which can predict the kinetic properties during the rapid solidification.

4.2.2.2.1 Kinetic coefficient

As discussed previously, the first step should be calculating the equilibrium solid-liquid phase boundary compositions for different temperatures, which is obtained by employing thermodynamic integration for pure Ti combined with semi-grand canonical ensemble (SGC) simulations of alloys. The phase boundary concentrations are the concentrations corresponding to the chemical potential difference where the grand potentials of the liquid and solid are equal. The Ti-rich composition-temperature phase diagram for Ni-Ti alloy is shown in Figure 4.10. For T=1613 K, the equilibrium solid and liquid phase boundary compositions have 3.95 and 10.67 atom% Ni, respectively. For T=1749 K, equilibrium compositions are 2.04 and 7.16 atom% Ni for solid and liquid phase, respectively. The composition range becomes even smaller as the temperature is elevated to 1860 K; between 0.8 and 3.22 atom% Ni. The equilibrium partition coefficient drops from 0.37 to 0.25 as temperature changes from 1613 K to 1860 K.

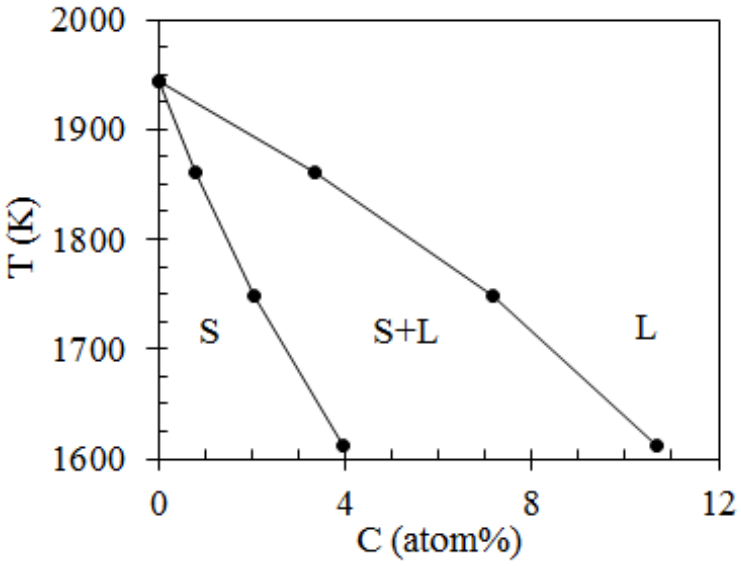

Figure 4.10. Ti-rich composition-temperature phase diagram for Ni-Ti alloy calculated by semi-grand method. The symbols L and S denote the liquid and solid phases, respectively.

Table 4.4 summarizes the details of the free solidification MD simulations. The driving force for solidification is the concentration difference; the initial concentration of the liquid phase is set to be smaller than the equilibrium liquid concentration. The more the concentration deviates from the equilibrium value, the higher solidification velocities are achieved in MD simulations. However, achieving higher solidification velocity at lower concentrations comes with the cost of higher uncertainty in the calculations. Therefore, the number of independent simulations considered for these states is higher than the cases with concentrations closer to the equilibrium liquid concentration. For each temperature, the initial concentrations of the liquid phase, $C_L^{initial}$, and the number of independent simulations used for each concentration, N_{MD}, is presented in this table. There are two interfaces in each simulation system, which in total give $2N_{MD}$ data sets for each state. For all states, the MD simulations are performed considering (100), (110), and (111) interface normal orientations to investigate the effect of crystallographic anisotropy on the kinetic coefficient.

Table 4.4. Details of the MD simulations. $C_L^{initial}$ is the initial composition of the liquid phase (atom%), and N_{MD} is the number of system replicas. Simulations were run for (100), (110), and (111) interface normal orientations

T=1613 K		T=1749K		T=1860 K	
$C_L^{initial}$	N_{MD}	$C_L^{initial}$	N_{MD}	$C_L^{initial}$	N_{MD}
4.5	9	2.5	9	1.1	9
5.0	9	3.0	9	1.25	9
5.5	9	3.5	9	1.4	9
6.0	9	4.0	9	1.6	9
6.5	9	4.5	9	1.8	9
7.0	4	6.5	4	2.0	9
8.0	4			2.3	4
10.0	4			3.3	4

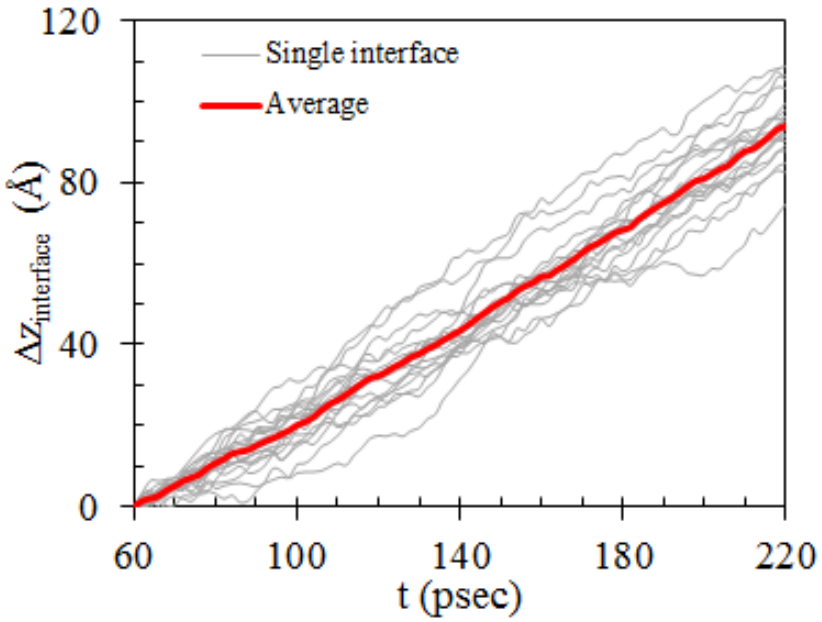

Figure 4.11. Crystal-melt interface displacement versus the simulation time over the steady-state time period during solidification of Ti-2.5 atom% Ni alloy at 1749 K. The gray lines are the results for single interfaces while the red line is the average of the 18 interfaces.

During an MD simulation, the solidification has three stages. In the beginning, there is a non-linear relationship between the interface position and time (non-constant interface velocity) until the solidification reaches steady state. During the steady-state period, the interface velocity is constant and is calculated from the slope of a linear fit to the interface position-time data. Due to the finite system size, the steady-state period is followed by a third stage with decreasing velocity over time which is due to the increasing concentration in the remaining melt and therefore decreasing driving force for solidification. Figure 4.11 demonstrates the steady-state part of the (100) oriented interface displacement versus time for solidification of Ti- 2.5 atom% Ni alloy at T=1749 K. Each of the gray lines represents the displacement of a single interface over time and the red line is the average position of the 18 interfaces from the 9 independent simulations (see Table 4.4). In the analysis, separate linear fits to the data for each interface gives a velocity, V_i, and the average velocity and 95% confidence interval are calculated from this set of averaged

velocities. We chose the steady-state time based on the best time range for the linear fit of position-time data. We also monitored the liquidus concentration at interface and the interface width to be sure they do not change during this period, and in case needed initially predicted steady-state region is shortened.

One important analysis performed in this study is determining the concentration profiles across the interfaces. For each time frame, first the interface position is defined and more than 20 Å into each solid and liquid side of the interface are binned as described in section 4.2.2.1.2 and atoms of each type are counted to obtain the concentration in each bin. The concentration profiles are then averaged over all the time frames and all $2N_{MD}$ interfaces. Averaging over all frames requires considering a moving reference on the interface, so bins are always created relative to the instantaneous interface position and topology. Figure 4.12 shows the average concentration versus the distance from the interface for 4 different initial concentrations at T=1613 K. The liquid phase is to the right and the solid phase is to the left of the interface, respectively. The error bars denote the 95% confidence intervals. Error bars on the liquid side are much larger than the solid side of the interface due to the larger diffusion coefficient in the liquid phase resulting larger fluctuations in the concentrations. For all four initial concentrations, there is a higher concentration on the liquid side of the interface compared to the solid side and, as expected, the position of the maximum concentration is in the liquid side of the interface. For $C_L^{initial} = 4.5$, the concentration only changes over a small region, assuming bulk values not far from the interface. As concentration increases, the width of the region where the concentration is changing increases. This observation will be further investigated in more detail.

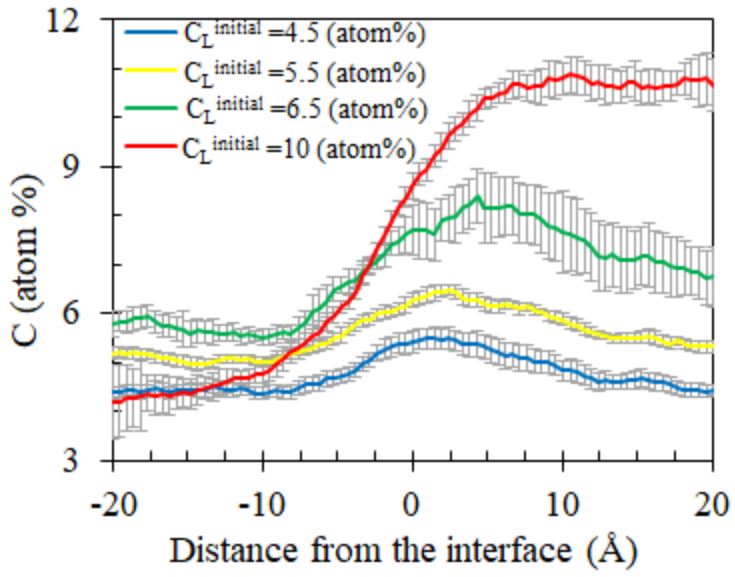

Figure 4.12. Average solute concentration over the $2N_{MD}$ independent simulations (2 interfaces per simulation) versus the distance from the interface for Ti-X atom% Ni (X=4.5, 5.5, 6.5, and 10) at 1613 K. Positive and negative values of distance from the interface correspond to the melt and crystal sides on the interface, respectively. Error bars denote the 95% confidence intervals.

Calculating the kinetic coefficient using equation (2.61) requires obtaining $f\big(k(V)\big)$ from equation (2.11) with a reasonable estimation of the drag coefficient, $\mathfrak{D}$. As described in the methodology, we chose the drag coefficient that gave the best linear relationship between the effective free energy, ΔG_{eff}, and interface velocity. The effective free energy is calculated by equations (2.4)-(2.6). The driving force and drag free energies are computed using thermodynamic integration and semi-grand canonical ensemble simulations as described in the methodology.

Figure 4.13 shows the velocity versus the driving force for the (111) orientation at T=1613 K for two cases: without drag and with drag. The black solid line is the linear fit of velocity versus ΔG_{eff} neglecting the solute drag. Specifically, the fitted line overestimates it for small driving forces. The intercept of the line is set at zero since the driving force should be zero at zero velocity. For this case, we found that $\mathfrak{D} = 0.37$ gave the best linear fit between the velocity and the

corresponding driving force. The blue points and solid blue line in Figure 4.13 correspond to the optimum value of $\mathfrak{D}$. The data for the case with solute drag fits much better to a line with R^2 = 0.85 compared to R^2 = 0.72 for the zero drag fit. The main effect of using the optimum $\mathfrak{D}$ is that, for both large and small velocities, the MD results agrees well with the linear fit.

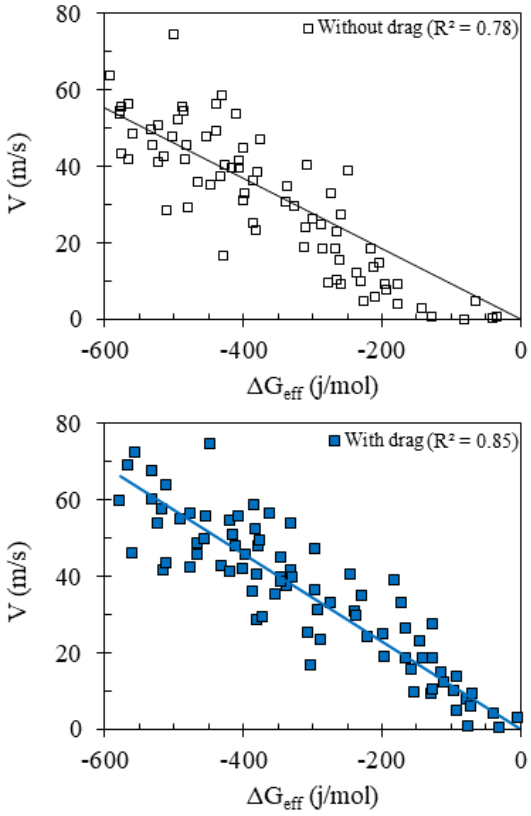

Figure 4.13. Scatter plot of the interface velocity versus the effective driving force with and without solute drag for the (111) orientation at T=1613 K. The solid lines are linear fits based on equation (2.14).

The optimal drag coefficients are determined for three different crystallographic orientations at different temperatures, and Table 4.5 summarizes the mobilities, drag coefficients, and kinetic prefactors, V_c, found in equation (2.14). Except for the (100) orientation at T=1860 K, the results presented in Table 4.5 follow a trend. We could say for each temperature, the largest mobility is obtained for growth of (100) oriented interface and it decreases as orientation changes

to (110) and (111). However, the M_{100}/M_{110} is very close to one, which can be interpreted as a very small anisotropy for the studied alloy compositions. This was expected as the Ti-rich compositions of binary Ni-Ti alloy have BCC crystal structures and BCC metals are known to have small anisotropy values for the interface energy and kinetic coefficient [14, 183]. Also comparing the mobilities given in each row of Table 4.5 shows that the interface mobility increases as the temperature increases. The optimal drag coefficients values, except for one case at T=1860 K and (100) orientation, range between 0.22 and 0.37, and they do not follow any special orientation-related, or temperature-related trend. The drag coefficient of 0.3 estimated by Yong et al. [100] for the Lenard-Jones metal systems and Ni-Cu alloys is within the range of our estimations.

Table 4.5. The mobility, M (m·mol/(s·J)), drag coefficient, $\mathfrak{D}$, and the kinetic prefactor, V_c (m/s), calculated for three interface normal orientations at T=1613, 1749, 1860 K.

	T=1613 K			T=1749 K			T=1860 K		
	M	$\mathfrak{D}$	V_c	M	$\mathfrak{D}$	V_c	M	$\mathfrak{D}$	V_c
(100)	0.116	0.27	1555.6	0.134	0.28	1948.5	0.114	0.51	1762.9
(110)	0.115	0.23	1542.2	0.132	0.28	1919.4	0.146	0.22	2257.7
(111)	0.112	0.37	1502.0	0.122	0.26	1774.0	0.132	0.22	2041.2

The velocity-dependent partition coefficients for three different studied cases (T=1613, 1749, 1860 K), with three different orientations, are presented in Figure 4.14. For all these cases, generally, the partition coefficient increases as the solidification velocity increases. One expects if the solidification velocity reaches a large-enough value, the solidification would be partitionless. Based on the studied MD simulation cases, which are presented in Table 4.4, one observes that although considering the initial liquidus composition far

from the equilibrium liquidus and close to the equilibrium solidus compositions leads to solute trapping, it does not guarantee the onset of partitionless solidification. Specifically for T=1613 K with equilibrium solidus and liquidus compositions of Ti-3.95 and 10.67 atom%Ni, using the initial liquid composition of Ti-4.5 atom%Ni results large-enough driving force to obtain k(V)≈1. Similarly, for T=1749 K, considering the initial liquidus composition (Ti-2.5atom%Ni) close to the equilibrium solidus composition (Ti-2.04atom%Ni) leads to complete solute trapping. For the T=1860 K, although the smallest investigated initial liquidus composition, Ti-1.1atom%Ni, is very close to the equilibrium solidus value, the driving force is large to observe some solute trapping but not large enough for partitionless solidification. For T=1613 and T=1749 K, if the effective driving force becomes larger than the 350-400 J/mol, the complete solute trapping occurs. While for the T=1860 K the largest possible effective driving force obtainable, considering both the solidus and liquidus compositions equal to equilibrium solidus concentration, is 256 J/mol. This suggests that the onset of partitionless solidification depends on the investigated alloy composition. In Figure 4.14, the partition coefficient at T=1860 K has the largest error bars, which is because the equilibrium solid and liquid phases only have 0.8 and 3.22 atom% solute particles. Very small concentration of solute in the system, especially in the liquid phase where atoms move frequently, leads to high uncertainties in the concentration calculations. Fitting the MD simulation results to the CGM and LNM solute trapping models, which is presented by the dotted and dashed lines in Figure 4.14, will be discussed in details in section 4.2.2.2.3.

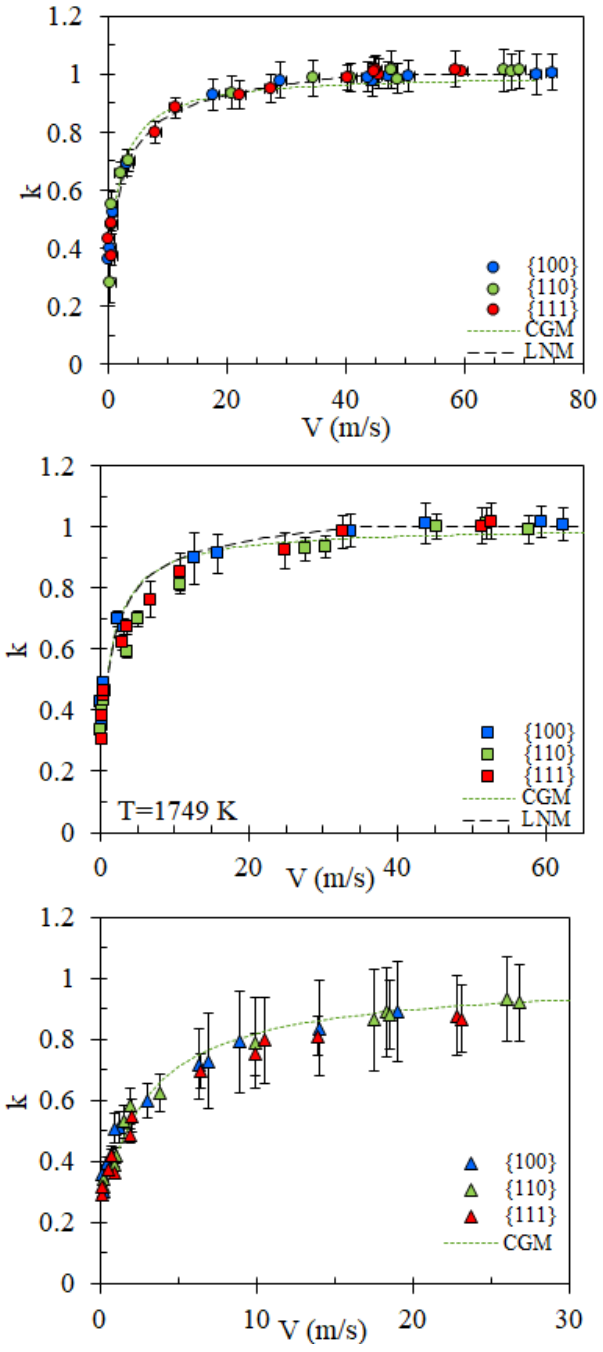

Figure 4.14. MD calculated values of partition coefficient versus the interface velocity for (100), (110) and (111) interface normal orientation. Error bars denote the 95% confidence in. The dotted and dashed lines are fit of MD data to CG [40] and LN [45] models respectively for (100) orientations.

Kinetic coefficient calculations require the drag coefficients, concentrations on liquid-side of the interface, interface velocities, equilibrium and non-equilibrium partition coefficients. These quantities are used to estimate the kinetic coefficient using equation (2.61), and as an example, Figure 4.15 presents the fit for solidification of (100) interfaces at T=1613 K. One finds a good linear relation between the $(1 - f(k)C^L/C_0^L)/(1 - k_e)$ term and solidification velocity with the slope corresponding to the kinetic coefficient. It worth mentioning that the very small velocities are not included in the fitting process, because based on equations (2.11) and (2.61), as velocity decreases, the $(1 - f(k)C^L/C_0^L)/(1 - k_e)$ term goes to zero. It is because both C^L/C_0^L and $f(k)$ will approximately be 1. Thus, if we consider very small velocities there would be a sharp increase in the y-axis values and the graph would have a quadratic-like shape with the minima close to V=0. In the fitting process, we only considered the velocities larger than the minima of the quadratic shape.

The kinetic coefficient values calculated by MD simulations are summarized under method 1 in

Table 4.6. For each orientation, increasing the temperature increases the kinetic coefficient value. We could say the kinetic coefficient is a function of temperature and the corresponding alloy composition. For a crystal with cubic symmetry, the kinetic coefficient as a function of interface orientation is given by:

$$\beta = \beta_0(1 + 3\varepsilon_k - 4\varepsilon_k \textstyle\sum_{i=1}^{3} n_i^4) \tag{4.12}$$

where n_i are the components of the unit vector, $\hat{n}$, normal to the interface plane, β_0 is the average kinetic coefficient, and ε_k is the anisotropy parameter [35] For different orientations at

each studied case, the kinetic coefficient values are very close to each other and the kinetic coefficient shows nearly isotropic behavior. Thus, in

Table 4.6, the anisotropy parameter is considered zero and β_0 is estimated by averaging the kinetic coefficient of all three orientations. The kinetic coefficient can also be estimated in terms of velocity of sound in the melt, V_s:

$$\beta = \frac{1}{V_s(1-k_e)^2 C_L^0} \tag{4.13}$$

Using this method requires calculating the velocity of sound in the liquid phase. We also performed MD simulations to calculate the isothermal speed of sound for the Ti-Ni alloys. Details of the calculations can be found in [184]. The velocity of sound for T=1613, 1749 and 1860 K are 4118, 4313, 4432 m/s, respectively. The speed of sound increases with increasing temperature (decreasing solute concentration). The kinetic coefficients calculated using equation (4.13) are listed under method 2 in

Table 4.6. The results of method 1 and method 2 are consistent and kinetic coefficients calculated using both methods follow similar trends with temperature.

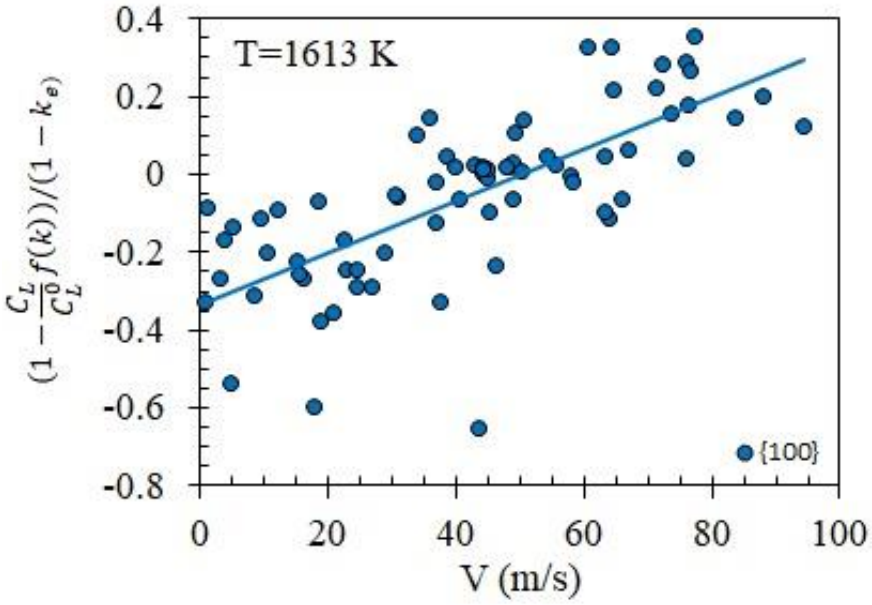

Figure 4.15. Scatter lot of $(1-\mathrm{f(k)C_L/C_L^0})/(1-\mathrm{k_e})$ versus velocity for T=1613 K and (100) interface normal orientations. The solid line is linear fits based on equation (2.61).

Table 4.6. The kinetic coefficient, β (s/m), calculated by two different methods at T=1613, 1749, and 1860 K. In method 1, the MD simulation results using three crystal orientations are fitted to equation (2.61). Using data for each orientation, the average kinetic coefficient, β_0 (s/m), and the kinetic anisotropy, ε_k, are calculated using equation (4.12). Method 2 is based on estimation of the kinetic coefficient using the speed of sound in the melt and equation (4.13). The numbers in the parentheses are the uncertainties in the last significant digits,

	Method 1					Method 2
	orientation	β	Expression (Eq.17)	β_0	ε_k	β
T=1613 K	(100)	0.0067	$\beta_0(1-\varepsilon_k)$	0.0057	0	0.0057
	(110)	0.0069	$\beta_0(1+\varepsilon_k)$			
	(111)	0.0035	$\beta_0(1+1.667\varepsilon_k)$			
T=1749 K	(100)	0.0072	$\beta_0(1-\varepsilon_k)$	0.0076	0	0.0062
	(110)	0.0086	$\beta_0(1+\varepsilon_k)$			
	(111)	0.0071	$\beta_0(1+1.667\varepsilon_k)$			
T=1860 K	(100)	0.0120	$\beta_0(1-\varepsilon_k)$	0.0130	0	0.0121
	(110)	0.0148	$\beta_0(1+\varepsilon_k)$			
	(111)	0.0117	$\beta_0(1+1.667\varepsilon_k)$			

4.2.2.2.2 Interface width

When talking about the interface width, there are two main approaches. The first definition is based on the concentration profile, as described by Aziz and Kaplan [40] and the second is based on some order parameter describing the local structure. For the first definition, the interface width is described as the thickness of the region where the solute concentration increases from its steady state value in the solid phase up to the maximum concentration inside the liquid phase. The concentration profiles in Figure 4.12 shows that when initial concentration is close to equilibrium value (slow solidification), the maximum concentration position is located far from the interface, and it moves closer to the interface as the solidification velocity increases. Doubling the distance between maximum concentration position and interface is a good estimation for the first definition of interface width. The second definition is based on the distance that order parameter [185], which is previously used to define the interface, changes between its corresponding solidus and liquidus values.

Figure 4.16 shows how the distance between the position of maximum concentration, $Z_{C^{L}_{max}}$, and interface, $Z_{interface}$, changes by the interface solidification velocity. In spite of the scatter in the data, a decrease in the interface width with increasing velocity is observed for all cases. Low solidification velocities provide enough time for the solute atoms to diffuse in front of the interface and prevent them from being trapped in the solid phase. Therefore, one would expect to get larger interface width as the velocity decreases.

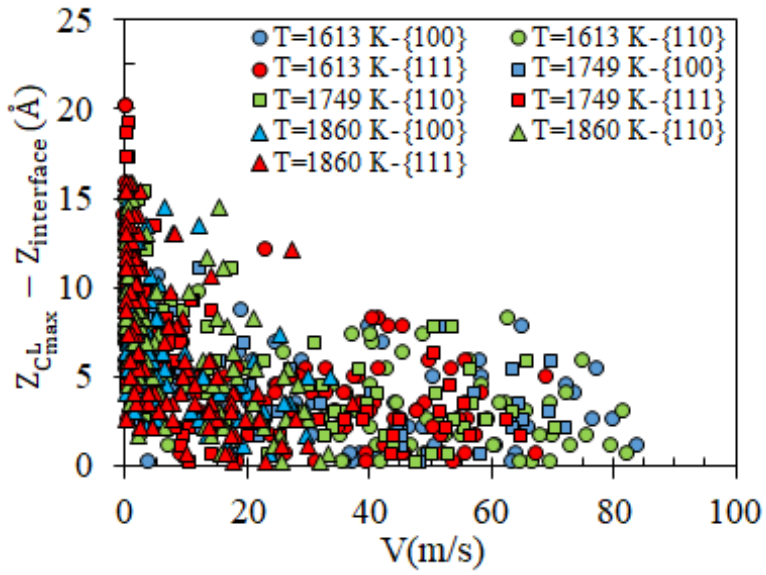

Figure 4.16. Scatter plot for interface width (first definition) versus interface velocities.

Figure 4.17 shows how the interface width, based on the second definition using local structure, changes with velocity for three different temperatures, and different orientations. The results demonstrate contradictions for the high and low solidification velocities. For velocities up to approximately 1 m/s, the interface width constantly increases as the velocity increases. As the velocity exceeds 1 m/s, the interface width decreases with an increase of interface velocity. This velocity is in the order of the diffusive velocity, which is the ratio of diffusion coefficient to the interface width.

The only relation we found relating the interface width to the solidification velocity is presented by Salhoumi and Galenko [186], where they studied rapid solidification and interface propagation kinetics both analytically and numerically. Using the hyperbolic phase field model [45], the effective interface thickness is defined as[186]:

$$l = \delta\left[1 - V^2/V_\varphi^2\right]^{1/2} \tag{4.14}$$

where δ is the mean interface width at V=0 and V_φ is the maximum phase field propagation velocity defined by the relaxation time, τ_φ, and phase field diffusion parameter, υ, such that $V_\varphi=(\tau_\varphi/\upsilon)^{1/2}$. The difference between parabolic phase field models [15] with the hyperbolic ones, is that for those models $\tau_\varphi=0$ ($V_\varphi=\infty$). This suggests, for slow solidifications, the interface width must stay constant while the MD-calculated interface widths, as presented in Figure 4.17, demonstrates an increase as the velocity increases from 0 to approximately 1 m/s.

As velocity increases and exceeds this limit, the interface width decreases, which is what we expected from equation (4.14). The fit for MD-calculated results to equation (4.14) is presented in Figure 4.17 and the fitting parameters are summarized in Table 4.7. For each temperature and all the velocity ranges, (100) orientation has the largest and (111) orientation has the smallest interface width and the results of (110) orientation lie between them. Also, the fit of T=1860 K results for (100) and (110) orientations did not result in a finite V_φ. We believe this can be because high velocities were not achieved for those sets of simulations.

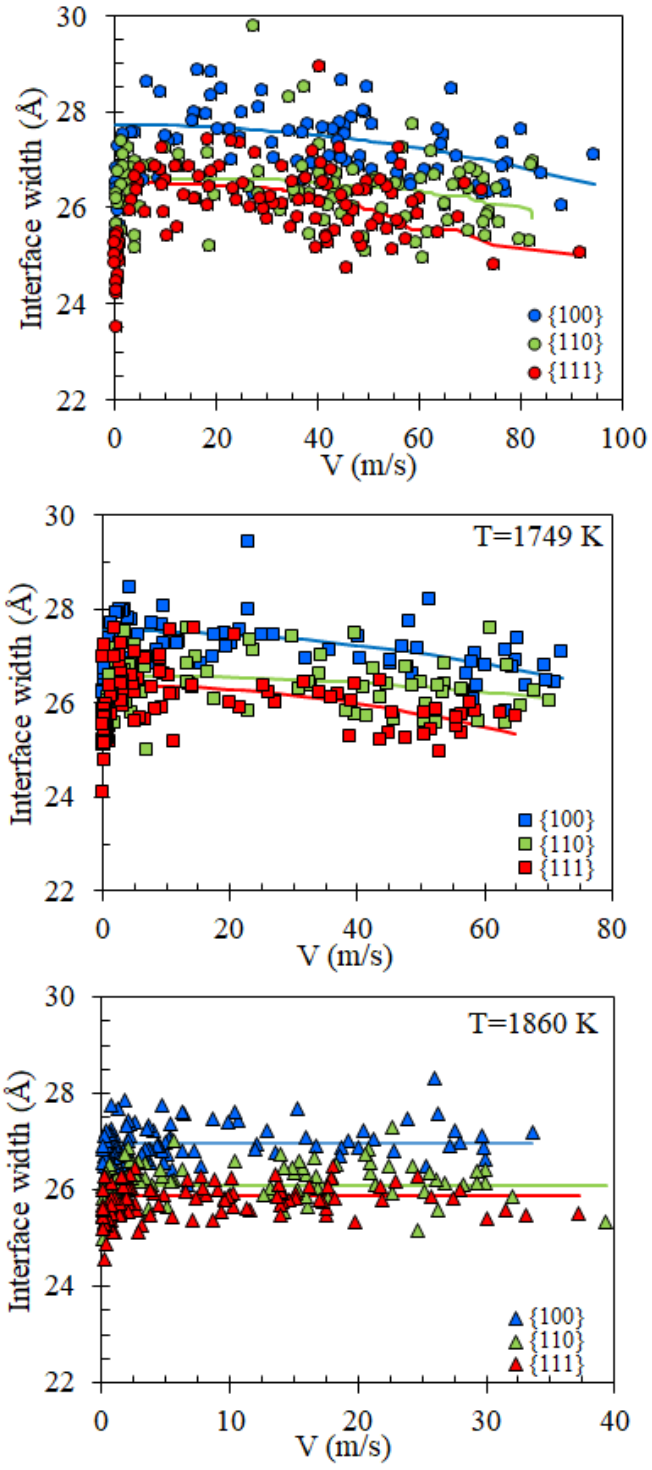

Figure 4.17. Scatter plot for interface widths (second definition) versus interface velocities. The solid blue, green and red lines are linear fits based on equation (4.14) for (100), (110), (111) orientations, respectively.

Table 4.7. phase field propagation velocity, V_φ (m/s), and mean interface width, δ (Å) calculated by fitting MD simulation results to equation (4.14) for T=1613, 1749, 1860 K and three interfacial orientations.

T(K)	orientation	V_φ	δ
1613	(100)	318.18 ±44.4	27.73±0.126
	(110)	381.93±91.5	26.62±0.141
	(111)	286.19±38.14	26.51±0.099
1749	(100)	268.89 ± 26.48	27.53± 0.093
	(110)	371.8± 94.7	26.58± 0.102
	(111)	232.43± 23.81	26.38±0.089
1860	(100)	∞	26.97
	(110)	∞	26.1
	(111)	319.21±161	25.88±0.05

4.2.2.2.3 Solute trapping

As discussed previously, Figure 4.14 also compares the MD partition coefficient values with CG [40] and LN [45] models. Overall, we can say CG model fits very well for the low to moderate solidification velocities but it fails for high values. This model cannot predict the onset of complete solute trapping. The dotted lines in Figure 4.14 show, based on the CG model, k=1 occurs at infinite solidification velocity, while the MD simulation results suggest that the complete solute trapping will occur at a finite velocity. In the CG model, the diffuse interface velocity, V_D^{CGM}, is the ratio of the interface diffusivity to the interface thickness, which cannot be calculated directly. Additional estimations of V_D^{CGM} like the ratio of liquid diffusivity to the interatomic spacing, or the 0.01 times the prefactor velocity, V_c, as defined by equation (2.14), can be used instead. Other than these estimations, one can consider it as a free parameter, and defined it using the best fit of MD results to CG model. The estimations of V_D^{CGM} from all three methods are illustrated in Table 4.8. It seems both method 1 and method 2 overestimate the diffuse interface

velocity and the values obtained from fitting the data to CG model are very smaller. One unsolved issue related to the non-equilibrium crystal-growth kinetics, is the diffuse interface velocity and its dependence on the interface orientations. For each temperature, the results presented in Table 4.8 show that V_D^{CGM} increase as the interface normal orientation changes from (100) to (110), and (111).

Table 4.8. the diffuse interface velocity for CG model, V_D^{CGM} (m/s) calculated from 3 methods, diffuse interface velocity, V_D^{LNM} (m/s), and bulk diffusion speed, V_B^{LNM} (m/s), for LN model calculated at T=1613, 1749, 1860 K and three interfacial orientations.

		V_D^{CGM}				
T (k)	Orient.	Method 1 $0.01\times V_c$	Method 2 D_L/λ	Method 3 Fitting MD results to CGM	V_D^{LNM}	V_B^{LNM}
1613	(100)	15.55	5.9	2.53±0.43	4.10±0.35	55.7±10.5
	(110)	15.42		2.89±0.35	2.96±0.35	48.1±13.5
	(111)	15.02		3.5±0.37	4.61±0.52	40.2±5.2
1749	(100)	19.49	10.7	2.6±0.20	1.98±0.18	50.8±28.2
	(110)	19.19		3.23±0.31	3.69±0.35	47.6±12.5
	(111)	17.74		4.0±0.35	2.8±0.2	47.7±18.9
1860	(100)	17.63	16.7	3.1±0.27	-	-
	(110)	22.58		3.52±0.27	-	-
	(111)	20.41		4.18±0.35	-	-

Contrary to the CG model, the LN model shows a great agreement with the MD results by predicting the onset of complete trapping at a finite velocity. The only method to estimate V_D^{LNM} and V_B^{LNM} in the LN model is to fit parameters and the obtained values of each model are presented in Table 4.8. In the LN model, V_B^{LNM} is the velocity beyond which the partition coefficient is equal to one and complete solute trapping occurs. For T=1613 K very high velocities were achieved and predictions of V_B^{LNM} were more accurate than the T=1749 K. One unsolved issue related to the non-equilibrium crystal-growth kinetics, is the dependence of interface orientation on the solute trapping. For T=1613 and 1749 K, the results presented in Table 4.8 show that V_B^{LNM} decreases as

the interface normal orientation changes from (100) to (110), and (111). This is more clear for T=1613 where the error in estimating V_B^{LNM} is small rather than T=1749 K. For T=1860 K as we did not achieve complete solute trapping in MD simulations, estimating the LNM model parameters was not possible.

4.3 Conclusion

Building on the ongoing developments and applications of atomistic simulation methods to the computation of important thermodynamic and kinetic properties of solid-liquid interfaces in metals, we performed detailed MD calculations of pure titanium and Ti-Ni crystal-melt interfacial energy, kinetic coefficient, and their corresponding anisotropies. Using the MD capillary fluctuation method, the calculated solid-liquid interface energy of of pure Ti 198 mJ/m^2 is in good agreement with the reported experimental data ranging between 149 and 207 mJ/m^2 and by adding Ni to the system the interface energy of the alloy decreases and the corresponding anisotropy increases.

By using the free solidification method, implemented based on a multiple layered thermostats approach, the kinetic coefficient of pure Ti and Ti-Ni dilute binary alloy is calculated. The kinetic coefficient of pure Ti is 0.71 m/(s-K).

For Ti-Ni alloys, the kinetic coefficient is predicted by an equation relating the concentration profile across the solid-liquid interface to the solidification velocity. For this first, the drag coefficient and interface mobility should be estimated. This requires the calculations of effective free energy change during the solidification, which is not possible by classical molecular dynamics and combined thermodynamic integration for pure Ti with semi-grand canonical ensemble (SGC) simulations of alloys are used to estimate it. The results show that the kinetic

coefficient ranges between 0.0057- 0.0121 s/m as the interface temperature increases from 1613 to 1860 K and , as expected for BCC crystal structure, it did not present large anisotropic behavior. We also presented the non-equilibrium partition coefficient and compared it to the solute trapping models namely the continuous growth model and local non-equilibrium model. The MD simulations predicted the onset of complete solute trapping for T=1613 and T=1749 K and partition coefficient values were more consistent with the local non-equilibrium model. For T=1860 K, the complete solute trapping was not achieved in the MD simulations. For T=1613 and 1749 K, the complete solute trapping happened when the effective free energy ranges between 350-400 J/mol and for T=1860 the maximum achievable effective driving force is 256 J/mol. This suggests that the complete solute trapping might not necessarily occur for all the alloys.

We also investigated the dependence of interface width on the solidification velocity. Two different definitions are used for the interface width; one is based on the local structure and the other based on the concentration profile. For slow solidifications, the solute atoms in the liquid phase have enough time to diffuse in front of the interface and the position of maximum concentration is far from the interface. As the velocity increases, solute atoms cannot diffuse ahead of the interface and as the velocity increases the position of the maximum of concentration gets close to the interface. The concentration based-interface width decreases dramatically as velocity increases. On the other hand, the local structure-based interface width also decreases with the velocity. The dependence of interface width to velocity is consistent with the predictions of hyperbolic phase field model, which is suitable for studying the rapid solidification.

5 ATOMISTICALLY INFORMED PHASE-FIELD SIMULATION OF SOLIDIFICATION FOR Ti AND Ni-Ti ALLOY[1]

Using phase field modeling simulation approach, we investigate the effect of various parameters on the solidification in a pure Ti and binary Ni-Ti system. The phase-field model is based on the CM interfacial properties calculated by molecular dynamics in the previous chapter.

5.1 Pure Titanium

For pure material, considering the time evolution of the thermal diffusion field subject to the crystal-melt interface conditions, the final time-evolution equations [55] for the two field variables, T and ϕ, are given by governing equations 2.19 and 2.20. The system of governing equations for the evolution of the phase-field order parameter and temperature are solved numerically using a finite difference algorithm The PETSC package is used as solver in our code [187]. All terms on the right-hand side of equation 2.20, except the Laplacian term, are discretized using a second order scheme, and for the Laplacian term we used the fourth order skewed 9-point scheme.

At the start of the simulation, a nucleus is placed on the bottom wall. Therefore, as the time progresses, the solid-liquid interface moves from the bottom wall up into the liquid phase. In order to eliminate the boundary affect, the computational domain has to be assumed considerably large. However, there is no need to solve the equations in the whole region when the solid-liquid interface is just affective in a small part of the region. Thermal diffusivity (D) is larger than $M\varepsilon(\theta)^2$, which means the temperature field is always ahead of phase field. In this technique, it is assumed that if

[1] Part of this chapter has been published in *Computational material science*, reprinted with the permission of the publisher. [S. Kavousi, B.R. Novak, M.A. Zaeem, D. Moldovan, Combined molecular dynamics and phase field simulation investigations of crystal-melt interfacial properties and dendritic solidification of highly undercooled titanium, Computational Materials Science, 163 (2019) 218-229].

the temperature at the boundary reaches 1 K larger than the temperature in the liquid phase far from the interface, more grid points are added to the computational region. The algorithm we used to implement the adaptive domain in PETSC is shown in Figure 5.1.

The simulations are carried out on a grid with $\Delta x = \Delta y = 0.5\zeta_p$ and $\Delta t = 10$ ps where ζ_p is the interface thickness which was set to be larger than the microscopic capillary length.

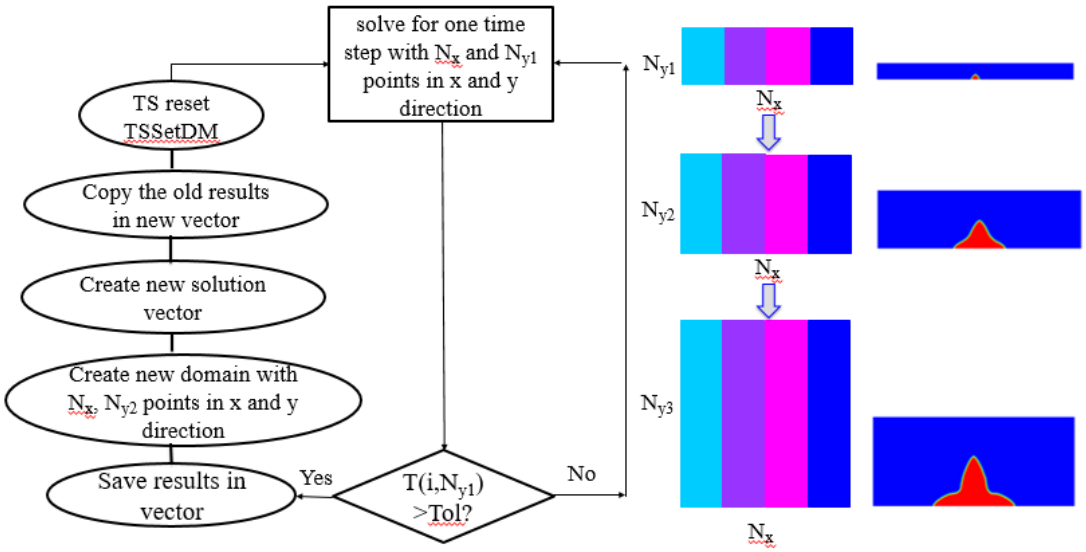

Figure 5.1. Algorithm to implement adaptive domain in the PETSC code

5.1.1 Phase-field parameters

The set of parameters entering the phase field equations (equations 2.19 and 2.20) are summarized in Table 5.1. These parameters were obtained by either MD simulations combined with thin-interface to phase-field mapping, as explained previously, or were taken from existing experimental data [120]. In 2D, the anisotropic ε and M parameters can be obtained from equations (5.1) and (5.2). θ is given by equation (5.3) where ϕ_x and ϕ_y are the derivatives of ϕ with respect to x and y respectively:

$$\varepsilon = \varepsilon_0(1 + \delta_\varepsilon \cos(4\theta)) \tag{5.1}$$

$$\frac{1}{M} = \frac{1}{M_0}(1 - \delta_M \cos(4\theta)) \tag{5.2}$$

$$\theta = tan^{-1}\left(\frac{\phi_y}{\phi_x}\right) \varepsilon = \varepsilon_0(1 + \delta_\varepsilon \cos(4\theta)) \tag{5.3}$$

Although the mobility anisotropy parameter, δ_M, depends on both μ and ϵ anisotropy parameters, it will be referred to as the kinetic anisotropy and δ_ϵ will be referred to as the capillary anisotropy.

Table 5.1. Thermophysical properties and phase field parameters for pure titanium. The parameters were obtained by either MD simulations or by combined MD with thin-interface to phase-field mapping or, for those properties indicated by *, were taken from existing experimental data [120].

L_0 [kJ/mol]	14.3 *	D [m^2/s]	9.5×10^{-5} *
C_p [kJ/mol K]	45.5 *	T_m [K]	1943 *
ρ [kg/m^3]	4130 *	γ_0 [mJ/m^2]	176
w [J/m^3]	2.9×10^7	ζ_p [m]	8×10^{-8}
ε_0 [$\sqrt{J/m}$]	0.000138	M_0 [m^3/sJ]	6.76
δ_ε	0.00455	δ_M	0.021

5.1.2 Results

Figure 5.2 shows the comparison of the steady-state solidification rate obtained from our phase field simulations, two sets of experimental data [188, 189], and from the analytical Lipton-Kurz-Trivedi (LKT) model [190] parameterized for titanium. The results from the phase field simulations, based on the model described by equations 2.19 and 2.20, are in reasonable agreement with the results from both experiments and LKT model for undercooling, ΔT, below 200 K. When ΔT is larger than 200 K, the phase field and experimental results start to deviate from each other and the deviation increases with increasing undercooling. The question is, what is the source of

this discrepancy? Is it caused by the inaccuracies of experimental investigations, by the limitations and inaccuracies of the phase field model or by both simulations and experiment? In the experiments, the solidification investigations at large undercoolings were done under electromagnetic levitation conditions. The nucleation of the solid phase was initiated by using a needle and establishing a contact with the levitating titanium droplet; the subsequent solidification time was estimated by tracking the evolution of the temperature at the top and bottom edge of the solidifying droplet. The solidification was considered to be completed when the temperature of the droplet top surface started to increase with respect to the undercooling temperature. As predicted by homogeneous nucleation theory, for undercooling in titanium smaller than 400 K, the probability of homogeneous nucleation in the liquid phase is very low, and therefore the nucleation process is unlikely to play any major role in determining the high solidification velocities obtained experimentally for large undercooling. It is therefore important to focus on possible sources of inaccuracies associated with model formulation, parameterization, and code implementation of phase field simulation methodology.

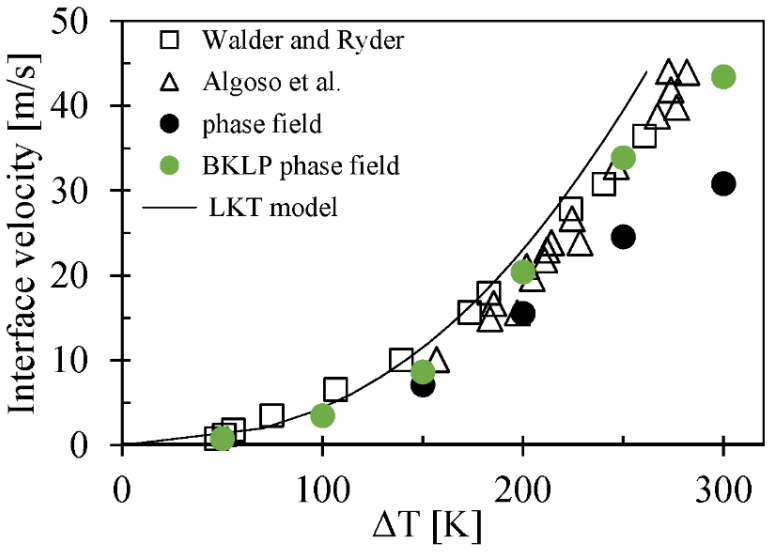

Figure 5.2. Interface velocity versus undercooling in titanium as obtained from phase field simulations, two sets of experiments [188, 189], and from the LKT analytical model.

As evident from Figure 5.2, the phase field simulations indicate that the variation of the interface velocity with undercooling exhibits a crossover from linear to an approximately square root dependence when the undercooling is about 150 K. To gain additional insight into the role of the phase field simulation model on the existence of such a crossover we performed additional phase field simulations based on slightly modified models. First, we investigate the solidification in a system with one-dimensional (1D) symmetry. Specifically, the equivalent of equation 2.20 for the order parameter in one dimension and in a reference frame that is translating with velocity V_n along the +x direction can be written in the following form:

$$-\frac{V_n}{M}\frac{\partial \varphi}{\partial x} = \varepsilon^2 \frac{\partial^2 \varphi}{\partial x^2} - wg'(\phi) - h'(\phi)\frac{L_0}{T_m}\Delta T \tag{5.4}$$

This can be rewritten in dimensionless form by normalizing the spatial and temperature variables $x' = \frac{x}{\bar{X}}$, $u = \frac{T}{L_0/c_p}$, where $\bar{X} = 10^{-6}\ m$. The dimensionless form of this equation in terms the new variables is:

$$-\frac{V_n}{\bar{X}}\frac{\partial \phi}{\partial x'} = \frac{\varepsilon^2}{\bar{X}^2}\frac{\partial^2 \phi}{\partial x^2} wg'(\phi) - h'(\phi)\frac{{L_0}^2}{c_p T_m}(u - u_m) \tag{5.5}$$

In the phase field method, the order parameter increases monotonically from zero to one as a function of position in the interfacial region and remains constant far from the interface. For each undercooling, there is only one specific value of V_n, which results in a physically valid solution of equation 5.5; it complies with the desired order parameter shape explained above [22]. Solving this boundary value problem with one unknown parameter was done by using *bvp4c* solver in MATLAB [191]. The solution of this second order boundary value problem with one unknown parameter requires the knowledge of three boundary conditions. The order parameter values are zero and one at -∞ and ∞ respectively and the derivative of the order parameter far from the interface is zero in both liquid and solid phases.

By solving the equation 5.5 for different values of ΔT, one can compute the interface velocity $V_n(\Delta T)$. Figure 5.3 shows the variation of the interface velocity with undercooling during solidification in a 1D system. Similar to the results obtained in phase simulations in the 2D system, discussed previously, for small undercoolings, up to ΔT ≈ 150 K, $V_n(\Delta T)$ varies approximately linearly with ΔT. At larger undercoolings, the interface velocity variation with undercooling follows a trend similar to 2D simulations at high undercoolings, and the undercooling temperature at which the deviation from linearity occurs is very close to undercooling temperature at which the 2D phase field simulation results start to deviate from the experimental results as seen from Figure 5.2.

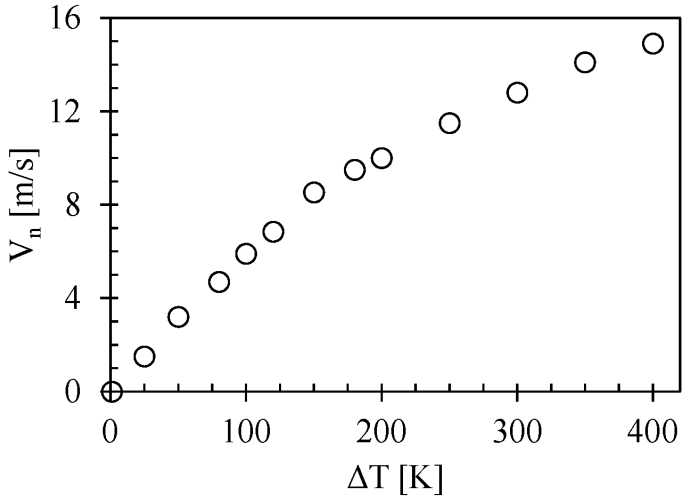

Figure 5.3**.** Variation of the steady state velocity of a planar one-dimensional interface with undercooling.

Based on the phase field simulation results in both 2D and 1D systems one can infer that the deviation from linearity of the interface velocity versus undercooling at large undercoolings might be related to the actual phase field model as represented in equations 2.19 and 2.20. Building on the methodology developed by Bragard *et al*. [22] we implemented and used a modified phase field model that seem to mitigate the shortcomings present at large undercooling in the regular

phase field model. The modification proposed by Bragard et al. consist of the introduced of a new form of the driving force term in the bulk free energy density function (the second term in the right-hand side of equation2.20) of the phase field method. Specifically, in this method the relationship between thermodynamic driving force and undercooling is chosen to behave like $V_n^{-1}(\Delta T)$, which is the inverse of the function V_n. The simulation results, based on the Bragard et al. modifications, hereby referred to as the BKLP phase field model, are also shown in Figure 5.2 and are in good agreement with the experimental results.

Another way that one can check the accuracy of phase field simulation results is to compare the values of the interface temperature as obtained from simulation with those calculated by using the analytic GT relation in equation 2.8. Based on the phase field formulation, the solid-liquid interface is at local equilibrium and as such the interface temperature must follow the GT equation. According to GT relation, the deviation of the interface temperature from the melting point is due to both capillary and kinetic effects and can be calculated by knowing: the interface velocity, interface stiffness, dendrite tip curvature, and kinetic coefficient. Figure 5.4 shows the variation with undercooling of the interface temperature as obtained directly from the phase field simulations and from the GT relation. The results from both phase field and BKLP phase field are presented. The calculation of the interface temperature from the GT relation is based on the following data: the MD calculated kinetic coefficient and stiffness, the phase-field calculated interface velocities (depends on the actual phase field model used), and tip curvatures.

As evident from Figure 5.4, for small undercoolings, $\Delta T < 150$ K, there is a good agreement between the interface temperatures obtained directly from the phase field model and GT relation; this is true for both phase field models used. As the undercooling increases above 150K the deviation between the interface temperature calculated directly from phase field simulation and

the value calculated from GT equation increases for both phase field models. It is however evident that when the BKLP phase field is used, the direct and GT interface temperatures are close to each other even at high undercoolings; the difference is less than 10 K at ΔT = 300 K. When the phase field model based on equations 2.19 and 2.20 is used the difference between the GT temperature and the direct temperature from phase field is about 32 K at ΔT = 300 K. One can rationalize these differences by the following observations: For small undercooling, both the capillary and kinetic effects play a role in determining the interface temperature. Although the dendrite tip shape has a higher curvature for larger undercooling, the effect of the kinetic term is still more dominant than the capillary one due to the large solidification velocity. Therefore, underestimation of the velocity calculated from the phase field method accounts for most of the deviation of the interface temperature from the GT equation.

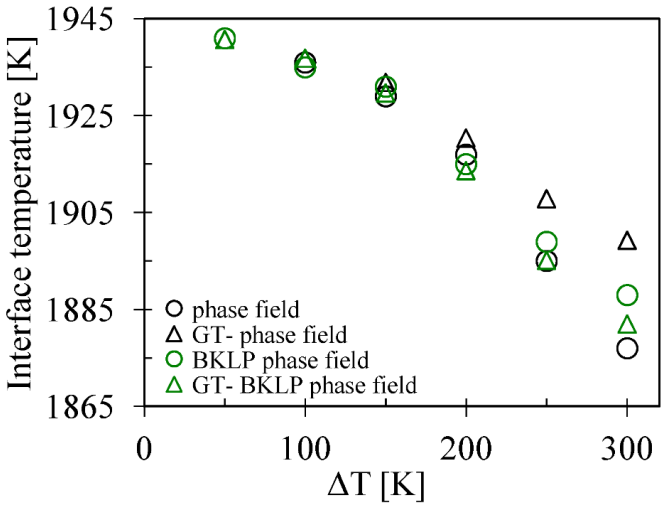

Figure 5.4. The variation with undercooling of the interface temperature as obtained by direct temperature calculation from phase field simulations and by use of Gibbs-Tompson equation.

Numerous studies show the importance of crystalline anisotropy on dendrite shapes [192] and growth rate [193]. The capillary and kinetic anisotropy calculated using MD simulations for titanium are $\delta_\varepsilon=0.0045$ and $\delta_M=0.021$ respectively and, in comparison with those for FCC metals,

these are very small. Given that the spectrum of anisotropy present in various metals and metallic alloys of different crystal structures is pretty large it is important to investigate, in a more general framework, its effect on solidification characteristics such as: solidification morphology, dendrite tip velocity, and mean solidification velocity. Therefore, in this section in addition to the simulations parameterized for titanium we will also explore model systems with anisotropies varying over a large range.

Figure 5.5 shows the shape of solid-phase generated during solidification by considering titanium and four other model systems at undercoolings of ΔT=100 K and ΔT=250 K. Figure 5.5 (a) and (d) are the morphologies of the simulated systems with anisotropy parameters corresponding to titanium. The other four morphologies correspond to model systems in which alternately one of the anisotropy terms was turned off. The anisotropy parameters were changed separately to study the individual effect of each term on dendrite morphology. Figure 5.5 (a), (b), and (c) illustrate the effect of the anisotropy parameters on the dendrite shapes for small undercooling of ΔT=100 K. Both the tip radius and the preferred growth direction are affected by the capillary and kinetic anisotropy parameters, δ_ε and δ_M. For the larger undercooling of ΔT=250 K shown in Figure 5.5 (d), (e), and (f), the effect of kinetic undercooling on the shape of the dendrites and preferred growth direction is much more pronounced and shows the emergence of side branches in the dendrites. Generation of secondary dendrite arms is related to the thermal diffusion layer thickness which in turn can be estimated as the ratio of thermal diffusivity over interface velocity (D/V). For large undercoolings, the small thermal layer thickness leads to large temperature gradients at the tips of protrusions. When the front of the protrusion faces an undercooled liquid, the heat is dissipated from solid into the liquid. In this case, the protrusion

grows and generates side branching. At low undercoolings, the temperature gradient at the tips of protrusions is small, therefore those protrusions cannot survive, and no side branching is observed.

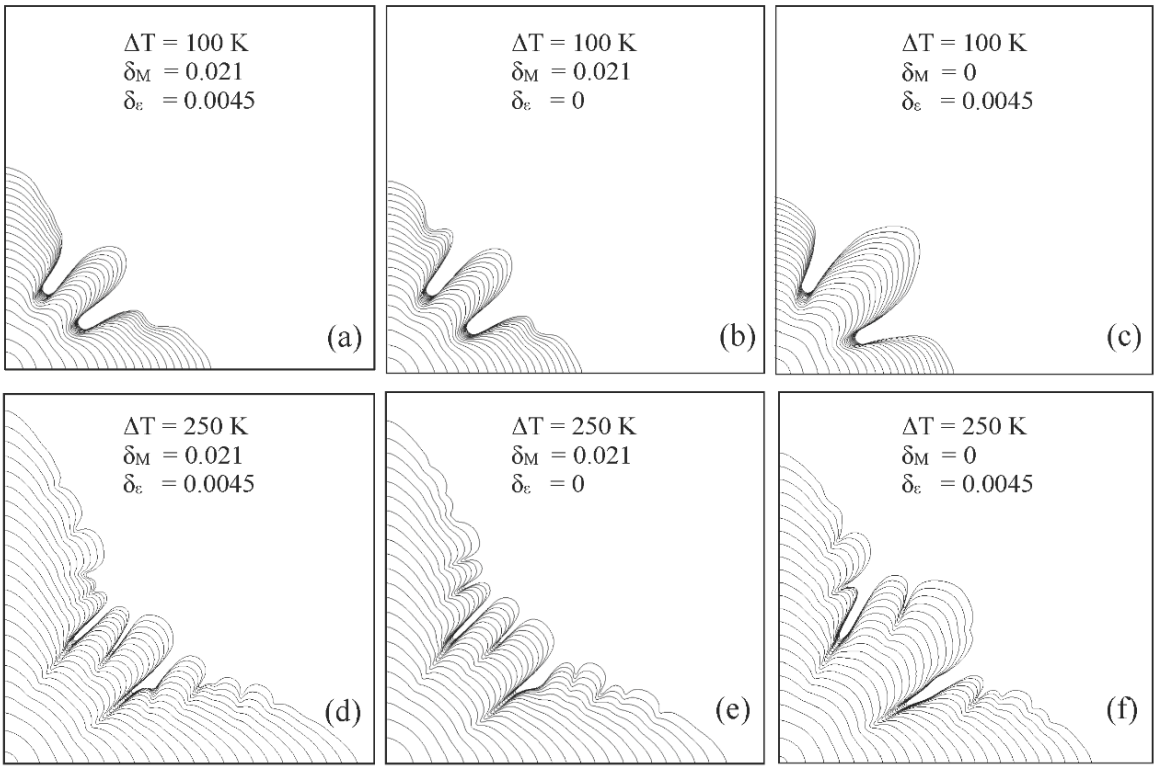

Figure 5.5. The effect of capillary, δ_ε, and kinetic, δ_M, anisotropy on dendrite morphology development during solidification in systems at two undercoolings

Figure 5.6 shows variation of the tip and average solidification velocities with kinetic anisotropy at undercoolings of ΔT=100 K and ΔT=250 K. The capillary anisotropy was maintained constant at δ_ε=0.0045 while the kinetic anisotropy was varied between δ_M=0 and δ_M=0.08. For both undercoolings, the simulation results show that the increase of δ_M leads to significant increase of the tip velocity while the average solidification velocity increased by only a small amount. Based on equation 5.2, higher kinetic anisotropy leads to a more preferred growth in directions parallel to the x and y-axis directions which in turn increases the tip velocity. When increasing δ_M from 0 to 0.08, at larger undercooling, the tip velocity increases from 16.85 to 23.4 m/s and the average solidification velocity increases from 25.83 and 26.78 m/s. At smaller undercooling when

varying δ_M, the tip velocity increases from 1.91 to 2.85 m/s and the average solidification rate increases from 3.28 to 3.62 m/s. These simulation results are in agreement with previous simulations [193] which also show that the effect of kinetic anisotropy is more dominant for large undercoolings.

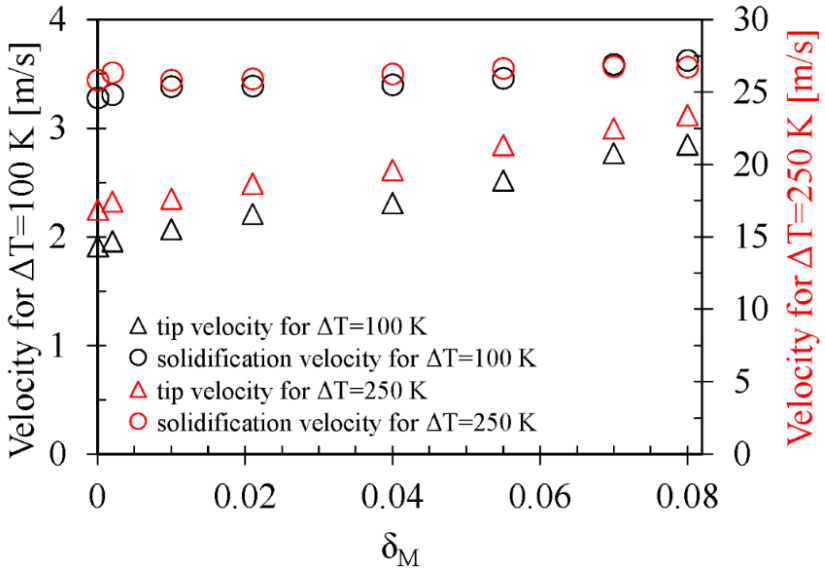

Figure 5.6. Variation of the tip and average solidification velocities with kinetic anisotropy at two undercoolings.

The same analysis is repeated by varying the capillary anisotropy and maintaining the kinetic anisotropy, δ_M=0.021, constant. Figure 5.7 illustrates the variation of the tip and solidification velocities with capillary anisotropy for two undercoolings. At small undercooling, the increase of δ_ε from 0 to 0.03 increases the tip velocity from 2.1 to 2.76 m/s and increases the average solidification velocity from 3.3 to 3.7 m/s. For larger undercooling, the increase of δ_ε from 0 to 0.03 increases the tip velocity from 18.21 to 20.86 m/s and increases the average solidification velocity from 25.58 and 26.7 m/s. As with kinetic anisotropy, increasing the capillary anisotropy parameter affects the tip velocity more than the average solidification velocity, especially at larger undercoolings.

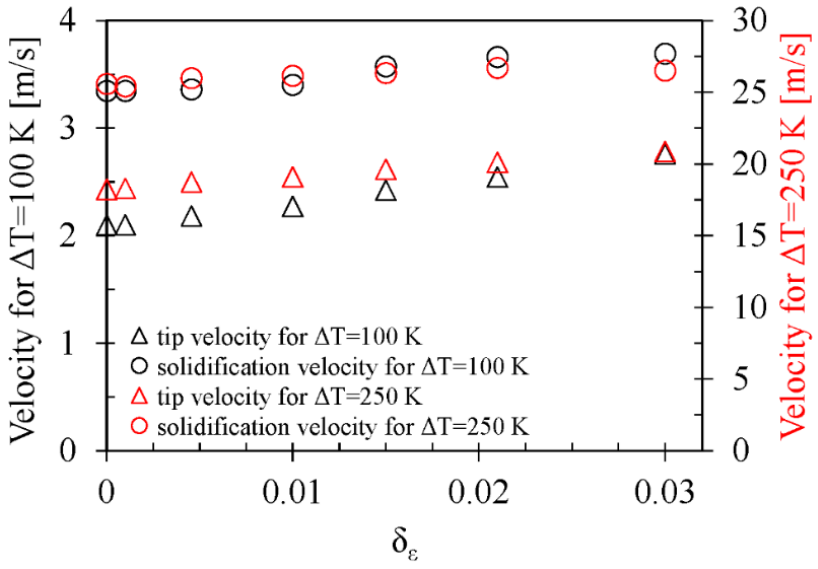

Figure 5.7. Variation of the tip and average solidification velocities with capillary anisotropy at two undercoolings.

5.2 Ni-Ti binary alloy

5.2.1 Phase-field parameters

The set of thermophysical parameters calculated by MD simulations which will later be used to parametrize the EFKP and PP phase field models (equations 2.26 and 2.27) are summarized in where εc and εk are the capillary and kinetic anisotropy parameters.

Table 5.2. These properties will be used later alongside the thin interface analysis relations, to obtain the characteristic dissipation time scale, τ_0, and the interface width, W, for the phase field model. Dependence of d and β parameters on the interface normal orientation is described as:

$$d(\vec{n}) = d_0(1 + 3\varepsilon_c - 4\varepsilon_c \sum_{i=1}^{3} n_i^4) \tag{5.6}$$

$$\beta(\vec{n}) = \beta_0(1 + 3\varepsilon_k - 4\varepsilon_k \sum_{i=1}^{3} n_i^4) \tag{5.7}$$

where ε_c and ε_k are the capillary and kinetic anisotropy parameters.

Table 5.2. Thermophysical properties calculated by MD simulations for Ti-X Ni alloys (x=0.9 and 3.22).

	Ti-0.9 atom% Ni	Ti-3.22 atom% Ni
γ_0 (mJ/m^2)	186	175
L_0 (kJ/mol)	14.3	14.3
m_L (K/atom%)	25.78	30.92
Γ ($\times 10^{-6}$ Km)	0.293	0.276
ΔT_0 (K)	62.5	207.8
d_0 ($\times 10^{-9}$m)	4.9	1.327
D_L ($\times 10^{-9}$m^2/s)	13.3	11
β (s/m)	0.0057	0.0130
ε_k	0	0
ε_c	0.007	0.01
C_L^0(atom%)	3.22	10.67
T_s (K)	1860	1613
k_e	0.245	0.370

5.2.2 EFKP phase field Model

The system of governing equations for the evolution of the phase-field order parameter and concentration are solved numerically using a finite-difference algorithm and PETSC package is used as the solver in our code [187]. Each simulation starts with the system consisting of two phases; a thin layer of solid phase at the bottom of the simulation box and liquid phase in the rest of the system. For the case of directional solidification, the solid phase grows as the temperature field with the gradient of G and the puling velocity V_p moves. The temperature gradient considered in this study is 10^8 K/m and the puling velocities range between 0.01-0.7 m/s. For the solidifications of Ti-0.9 atom% Ni and Ti-3.22 atom% Ni, the ratio of interface width to the capillary length is assumed to be 2 and 6 respectively. This two parameter are chosen such that the the two systems have approximate equal domain sizes. The corresponding values for the interface width and characteristic dissipation time scale are presented in Table 5.3. Using the thin interface

analysis, as presented in section 2.5, considering a non-zero kinetic coefficient increases the value of τ_0.

Table 5.3. The interface width, W(m), characteristic dissipation time scale, τ_0(s), for Ti-X Ni alloys (X=0.9 and 3.22) based on the zero and MD calculated kinetic coefficient, β (s) and using thin interface analysis (equations (2.65) and (2.66))

	Ti-0.9 atom% Ni		Ti-3.22 atom% Ni	
	β=0	β=0.0057	β=0	β=0.013
W/d_0	2.0	2.0	6.0	6.0
W ($\times 10^{-9}$)	9.808	9.808	7.96	7.96
τ_0 ($\times 10^{-8}$)	0.561	0.600	1.755	1.782

Figure 5.8 shows the steady-state concentration profile change along the interface during Ti-0.9 atom% Ni solidification for V_p = 0.01 m/s and V_p = 0.5 m/s. For smaller puling velocity, the solute particles have enough time to diffuse ahead of the interface while for the high puling velocities solute particles are trapped inside the interface. For the last case, the width of the concentration profile shrinks as the interface velocity increases. This was also observed in our MD simulations, presented in Figure 4.16, where the concentration profile width decreases exponentially as velocity increases. Therefore, the position of the maximum concentration located in the liquid phase gets closer to the interface position.

There is a jump in the concentration profile of Figure 5.8. The left and right-hand side of the jump corresponds to the solid and liquid phases, respectively. As the solidification velocity increases, one expects the solute atoms to be trapped inside the liquid phase. Comparison of the results for V_p = 0.01 and 0.5 m/s presented in Figure 5.8 shows that the solute concentration of solid increases with the increase of interface velocity. In addition, a clear reduction of the concentration peak value is observed, as the velocity increases. The solute concentration increase on the solid-side coupled with a concentration decrease at the maximum point in the liquid-side leads to an increase of the partition coefficient.

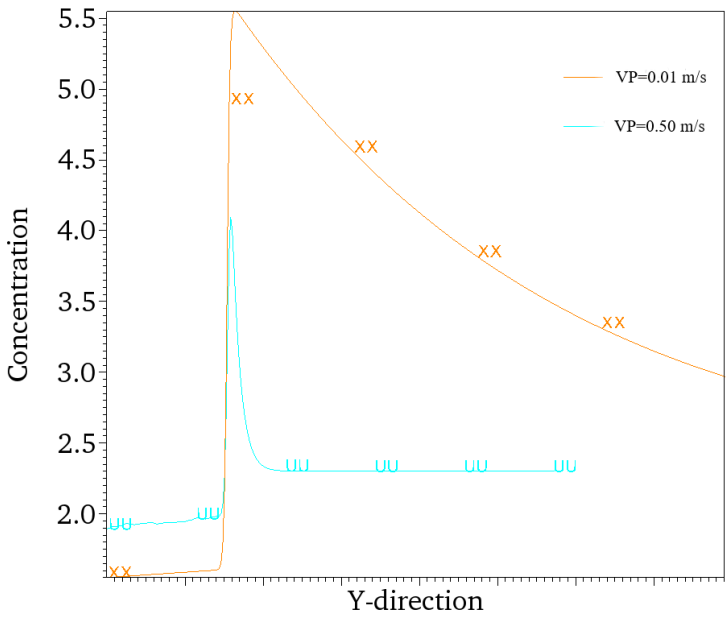

Figure 5.8. Concentration profile change along the interface during Ti-0.9 atom% Ni solidification for V_p=0.01 m/s and V_p=0.5 m/s

The proper analysis of the phase field results pertaining to the velocity-dependent partition coefficient requires an a priory clear and realistic definition of the partition coefficient. Different definitions have been used in various phase field simulations. Ahmad et al. [23] defined the solid concentration as the concentration at the end of the solid-side diffuse interface and the liquid concentration as the peak value of the concentration profile:

$$k(V) = \frac{C_s}{C_L} = \frac{C|_{\varphi=0.999}}{max(C)} . \tag{5.8}$$

While Lebedev et al. [69] used the same definition for solid-side concentration he used the concentration at the end of the liquid-side diffuse interface as the liquid concentration. Therefore, the partition coefficient can be estimated as:

$$k(V) = \frac{C_s}{C_L} = \frac{C|_{\varphi=0.999}}{C|_{\varphi=-0.99}} \quad . \tag{5.9}$$

Danilov and Nestler [24] suggested that the solidus and liquidus concentrations must be considered as the concentration at some distance (x = ±δ) from the center of the interface (φ=0) and therefore

$$k(V) = \frac{C_s}{C_L} = \frac{C|_{x=-\delta}}{C|_{x=+\delta}}. \tag{5.10}$$

From this multitude of definitions of the partition coefficient, the one used in most studies is based on equation (5.8) and it will be the one adopted in our study as well. According to the investigations of Zhang et al. [20], the hyperbolic phase field models (EFKP), when considering both the cases with and without the anti-trapping flux, overestimates the partition coefficient and it predicts the onset of the solute trapping at a lower velocity than the CGM model. Their study also showed that this model is very sensitive to the value chosen for the interface width. These findings were tested by comparing the results obtained by phase field and MD simulation.

The anti-trapping flux term was originally added to the phase field model to eliminate the chemical potential jump across the interface, which has to be eliminated at high velocities. The jump in the chemical potential favors the trapping of the solute atoms in the solid phase which can be mitigated by adding the anti-trapping flux

$$\vec{J}_{at} = -a_t W_0 (1 - k_e) C_L^0 \frac{\partial y}{\partial x} \frac{\overrightarrow{\nabla\varphi}}{|\overrightarrow{\nabla\varphi}|}, \tag{5.11}$$

that has the effect of restoring the chemical equilibrium at the interface [15]. It should be mentioned that when using the EFKP model to study the slow solidification, the kinetic coefficients are considered zero and the anti-trapping term is present in the phase field equations. However, when using this model to simulate the rapid solidification, one should include the actual values of the kinetic coefficients into the model and eliminate the anti-trapping term [17].

Figure 5.9 shows the phase field–calculated partition coefficient variation with velocity for the solidification of Ti-3.22 atom% Ni alloy. Three different plots are presented in this figure. The

first plot shows the results when the kinetic coefficient is considered to be equal to zero, and the anti-trapping term is added to the phase field equations. The second plot corresponds to the modifications suggested for modeling the rapid solidification using EFKP model in which a non-zero kinetic coefficient was considered and the anti-trapping flux term was eliminated. These two phase field simulation results for the partition coefficients are compared with those obtained from molecular dynamics simulations depicted in the third plot. As seen from Figure 5.9, in the velocity range of these studies, the anti-trapping term prevents the solute trapping by applying a flux on the opposite direction which prevents the solute atoms from trapping inside the solid . This flux changes linearly with velocity and even at V = 0.5 m/s, we were still not able to observe a considerable amount of solute trapping.

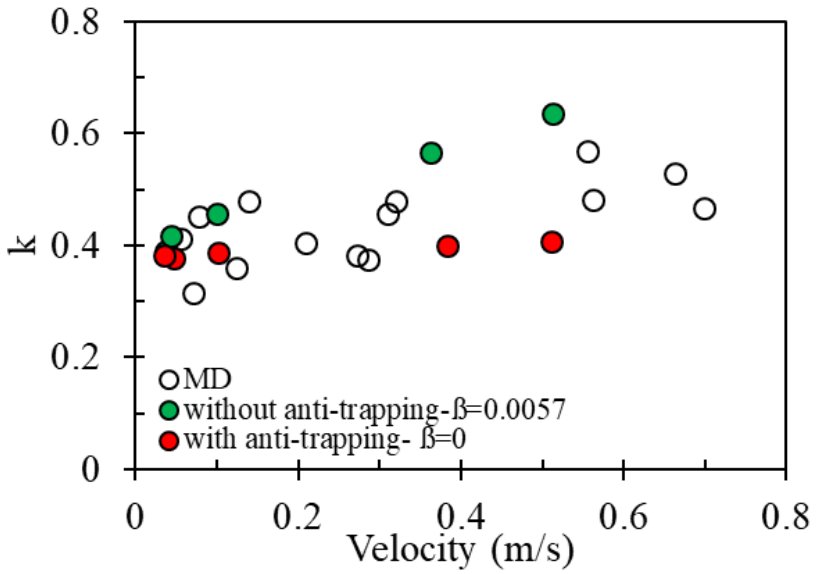

Figure 5.9. The velocity-dependent partition coefficient for solidification of Ti-3.22atom%Ni from i) MD simulations ii) EFKP model-with the anti-trapping flux and β=0 s/m iii)EFKP model without the anti-trapping flux β=0.0057.

Using the MD-calculated kinetic coefficient, β, and eliminating the anti-trapping flux, results in an increase in the partition coefficient as the solidification velocity increases. The MD calculated partition coefficient lies between the results of two sets of phase field simulations. This

suggests that the EFKP model without the anti-trapping term and with the non-zero kinetic coefficient overestimates the partition coefficient; similar to what was observed by Zhang et al. [20]. On the other hand, Zhang et al. [20] predicted that the solute trapping occurs even when the anti-trapping term was considered, while, at least in the velocity range we studied, we did not observe any considerable amount of trapping.

For reference and comparison the kinetic coefficient calculations under the same three assumptions were also performed in the investigations of solidification of Ti-0.9 atom % Ni alloy and the results are depicted in Figure 5.10. The comparison of MD results with those obtained from the two phase field models shows that the MD simulation results lie between the two obtained from the phase-field simulations.

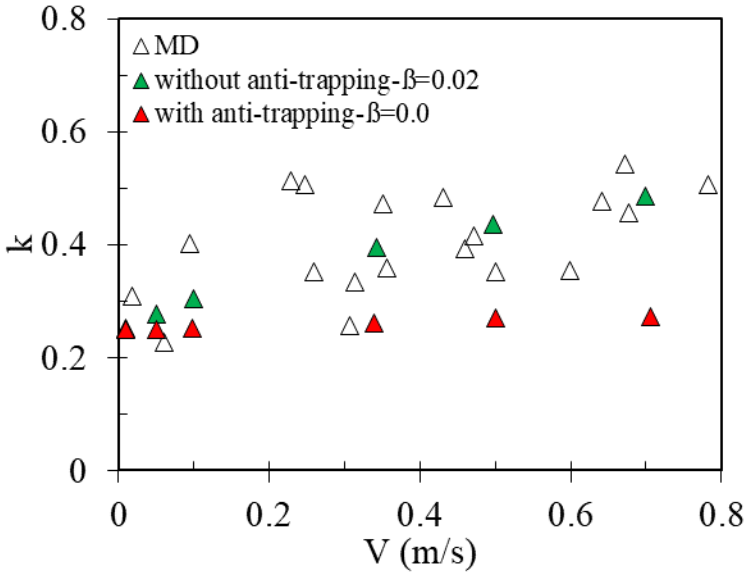

Figure 5.10. The velocity-dependent partition coefficient for solidification of Ti-0.9atom%Ni from i) MD simulations ii) EFKP model-with the anti-trapping flux and β=0 s/m iii)EFKP model without the anti-trapping flux β=0.02

As mentioned previously solidification involves multiple spatial and temporal scales. When studying the kinetics of attachment of liquid atoms to crystals during solidification, the atomic attachment time scale is of the order of a few picoseconds and the solid-liquid interface has

a thickness of the order of a few nanometers. The microstructural features are observed on the length scale of hundreds of micrometers and the diffusion of heat and solute during solidification occur and require studies over time scale scales of the order of a few seconds. Considering a larger value for the interface width, and the corresponding dissipation time scale, allows the time scale in simulations to be reduced to a few hundreds of microseconds. These modifications might on the other hand effect on the solute trapping and as such need to be evaluated further. Therefore, two sets of phase field simulations of solidification of Ti-0.9 atom% Ni alloy were performed and the corresponding W and τ_0 for each simulation are presented in corresponding W and τ_0 are presented in Table 5.4. The partition coefficients for these two phase field simulation sets are compared with MD simulations in Figure 5.11. The results clearly show that using larger interface width value results in an overestimation in predictions of phase field modeling. Previous comparison of results for Ti-0.9 atom% Ni and Ti-3.22 atom% Ni solidifications showed the former resulted closer predictions of partition coefficient to the MD simulation results. Based on the results of Table 5.4 we could say this could be due to the fact that for the simulation of Ti-3.22 atom% Ni solidification, the interface width was initially considered 6 times the capillary length. But for the solidification of Ti-0.9 atom% Ni the interface width was initially considered 2 times the capillary length. Therefore, the predictions of EFKP model were very close to the MD simulation results.

Table 5.4. The interface width, W (m), characteristic dissipation time scale, τ_0(s), for cases I and II which are used to investigate the effect of interface width on the predictions of EFKP model during Ti-0.9 atom% Ni solidification

	Case I	Case II
W/d_0	2.0	8.0
W ($\times 10^{-9}$)	9.808	39.23
τ_0 ($\times 10^{-8}$)	0.561	36.53

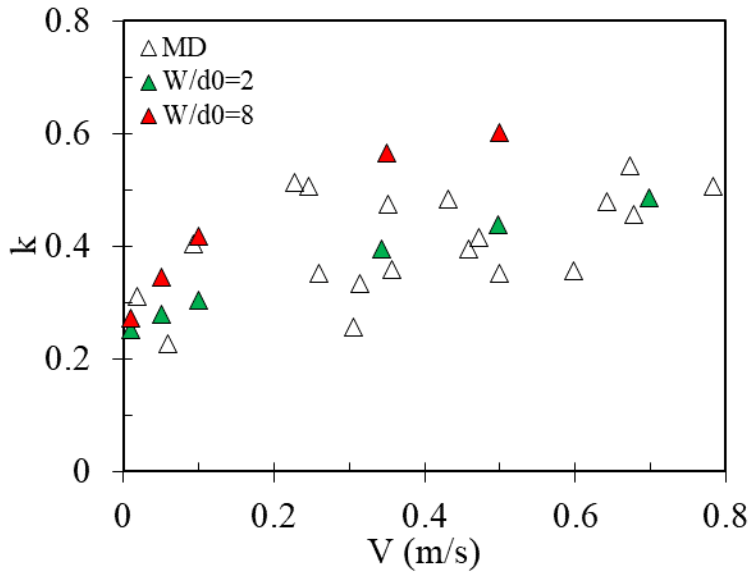

Figure 5.11. The velocity-dependent partition coefficient for solidification of Ti-0.9atom%Ni from i) MD simulations ii) EFKP model without the anti-trapping flux β=0.02 and using $W/d_0=2$ iii) EFKP model without the anti-trapping flux β=0.02 and using $W/d_0=8$.

5.2.3 PP phase field model

The difference between the EFKP and PP phase field model is the anti-trapping term. The anti-trapping term is modified so that we have control over the amount of solute trapping during the phase field simulation. The constant in the anti-trapping flux, a_t, is changed from the constant value of $1/2\sqrt{2}$ to a function of order parameter, as explained in equation (2.28). Performing phase field simulations using PP model requires defining parameter A in equation (2.28). Using perturbation theory, Pianomaa and Provatas [35] defined that using equation (5.12) the relationship between the interface velocity and partition coefficient maps to the CG model. In order to calculate A, the partition coefficient of CG model is fit to the equational form presented by equation (5.12) [35].

$$k^{PF}(V) = k_e exp\left(\sqrt{2}(1-k^{PF}(V))\frac{V}{V_D^{PF}}\right) \tag{5.12}$$

where V_D^{PF} is the characteristic solute trapping velocity given by:

$$V_D^{PF} = \frac{D_L}{AW} \tag{2.71}$$

This method requires knowing the diffuse interface velocity for CG model, V_D^{CGM}, which is estimated by fitting the experimental velocity-dependent partition coefficient to the CG model. The limitation of this method is due to the scarcity of available experimental data. In this study, we fit the MD-calculated partition coefficients to the CG model (equation 2.14) and PP phase field model (equation 5.12) to estimate V_D^{CGM} and V_D^{PF}respectively. Figure 5.12 shows the relation between the partition coefficient and velocity for the MD simulation results and corresponding fits to equations (2.14) and (5.12) for the (100), (110), and (111) interface normal orientations for Ti-3.22 atom% Ni solidification. For the (100) orientation$V_D^{CGM} = 2.1\ m/s$, and$V_D^{PF} = 2.35\ m/s$. For estimating V_D^{PF}, first, the MD results are fitted to the CG model which resulted $V_D^{CGM} = 2.1\ m/s$. Then the equation 5.12 is solved numerically using the velocity and partition coefficient from the fitted CGM to estimate the V_D^{PF}. The corresponding diffuse interface velocities are summarized in Table 5.5. As in the phase field model the "A" parameter does not depend on orientation, we have averaged over different orientations and used equation (2.71) to estimate this parameter.

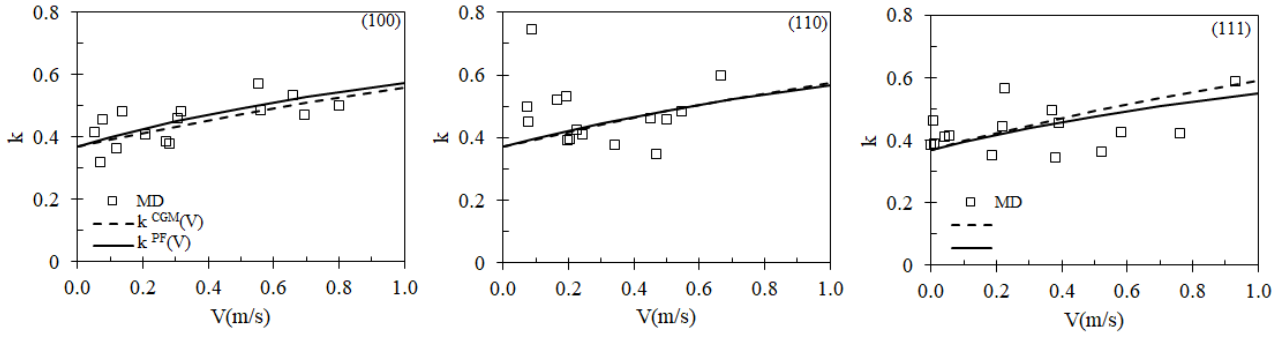

Figure 5.12. Scatter partition coefficient versus velocity from the MD simulation of Ti-3.22atom%Ni solidification for the (100), (110), and (111) interface normal orientations and the corresponding fits to equation (2.14), as the CG model, and equation (5.12), as the PP phase field model.

Table 5.5. The diffuse interface velocities calculated by fitting the MD results to the partition coefficient-velocity relations for the CM model (equation 2.14) and PP phase field models(equation 5.12) for Ti-Xatom%Ni (x=0.9, 3.22) alloy solidification

Alloy	orientation	V_D^{PF}	V_D^{CGM}
Ti-0.9atom%Ni	(100)	1.09	1.73
	(110)	1.17	1.977
	(111)	1.4145	2.50
Ti-3.22atom%Ni	(100)	1.515	2.53
	(110)	1.36	2.22
	(111)	1.233	3.11

Table 5.6 summarizes the phase field parameters used to solve the PP phase field model. It is noted that the PP model is developed for two cases considering full-drag and no-drag. The MD simulations, presented in Table 4.5, showed that the drag coefficient is approximately 0.3. However, in our phase field analysis, we only considered drag coefficients equal to zero and one.

Table 5.6. The parameters used in PP phase field model to study Ti-Xatom%Ni (X=0.9 and 3.22) solidification using zero and non-zero kinetic coefficient and considering fill-drag and no-drag. A is the anti-trapping parameter, W is the interface width (m), d_0 is the capillary length and τ_0 (s) is the characteristic dissipation time scale.

	Ti-0.9 atom% Ni				Ti-3.22 atom% Ni			
	With drag		Without drag		with-drag		without-drag	
	β=0	β=0.02	β=0	β=0.02	β=0	β=0. 057	β=0	β=0. 057
A	1.097	1.097	1.097	1.097	1.017	1.017	1.017	1.017
W/d_0	2.0	2.0	2.0	2.0	6.0	6.0	6.0	6.0
$W (\times 10^{-9})$	9.81	9.81	9.81	9.81	7.96	7.96	7.96	7.96
$\tau_0 (\times 10^{-8})$	1.683	1.722	0.235	0.250	5.01	5.037	0.738	0.764

Figure 5.13 compares the PP phase field model results of Ti-0.9 atom% Ni and Ti-3.22 atom% Ni solidification with the corresponding CG model. The fit to CG model is calculated based on the MD simulations. For each alloy, four sets of phase field simulations are performed which

is based on different combinations of zero/non-zero kinetic coefficient and no/full solute drag. For all the phase field simulations the partition coefficient increases with the increase of velocity and the calculated partition coefficients are very close to each other. At lower velocities, the phase field simulation results match very well with the CG model. As the velocity increases, the deviation between the CG model and phase field simulation increases too.

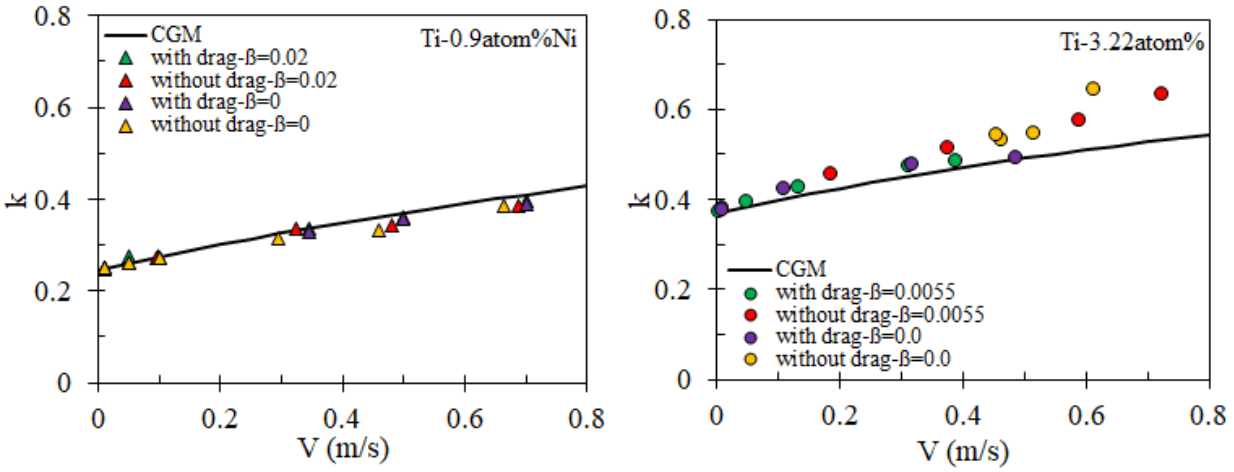

Figure 5.13. Comparison of PP phase field model results of Ti-0.9atom%Ni and Ti-3.22atom%Ni solidification with the corresponding CG model

Figure 5.13 showed that the diffuse velocity choice, V_D^{PF}, affects the results of the phase field simulations rather than considering full/no drag or using a zero/non-zero kinetic coefficient. By fitting the partition coefficient to equation (5.12), one defines the trend line for the phase field predictions and, at least at lower velocities, does not expect to observe any change in the predictions. This statement is tested in Figure 5.14 where we compared the phase field simulation using an MD-calculated kinetic coefficient with a system model with a kinetic coefficient equal to 0.5 s/m. The reason for choosing such a large kinetic coefficient value is that in the paper by Pianomaa and Provatas [35] they chose considerably large kinetic coefficient values for validating their model, and for this, we try to investigate the effect of kinetic coefficient on the results. The results of Figure 5.14 show that the change of kinetic coefficient does not affect the partition

coefficient values. It looks that parameters affecting V_D^{PF}, namely interface width, parameter A, and diffusion coefficient, affect the predictions of PP phase field model.

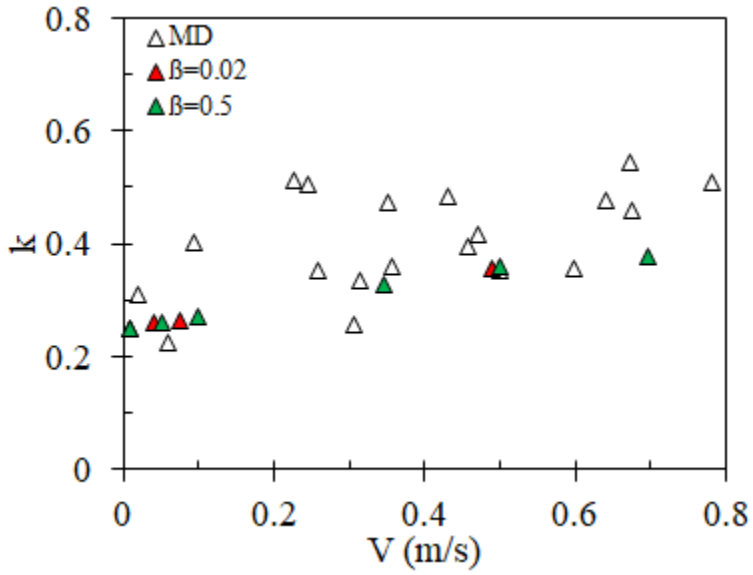

Figure 5.14. The velocity-dependent partition coefficient for solidification of Ti-0.9atom%Ni from i) MD simulations ii) PP model with full drag and using β=0.02 s/m iii) PP model with full drag and using β=0.5 s/m.

We have previously stated that the expected results of the phase field simulations are fit to CGM so that the partition coefficient-velocity relation follows equation (5.12). Therefore, V_D^{PF} is the critical parameter to determine the behavior of PP phase field model. On the other hand, there is a reverse correlation between V_D^{PF} and AW, and the magnitude of A defines the difference between EFKP and CG model. If the A parameter is very small, so the PP model will be close to EFKP model, where we did not eliminate the anti-trapping, and we expect to see very small solute trapping in the system. In order to test this statement, we considered three different cases, presented in Table 5.7, to study the solidification of T-0.9 atom% Ni using the PP phase field model. Case II is the same case studied in Table 5.6 with a non-zero kinetic coefficient with considering the full solute drag. Cases I and III have different interface width values, and corresponding parameter

A values. The phase field simulations of these three cases and their comparison with MD simulations are presented in Figure 5.15.

Table 5.7. The interface width, W (m), characteristic dissipation time scale, τ_0 (s) and A, for cases I-III which are used to investigate the effect of parameter A on the results of PP model by studying Ti-0.9 atom% Ni solidification

	Case I	Case II	Case III
W/d_0	0.5	2.0	8.0
W ($\times 10^{-9}$)	2.452	9.808	39.23
τ_0 ($\times 10^{-8}$)	0.081	0.561	36.53
A	4.388	1.097	0.274

The results presented in Figure 5.15 model shows that as the interface width increases, the PP phase field model does not predict any solute trapping. For W/d_0=8, parameter A is the smallest among the three cases and one expects the PP phase field simulation results to be close to EFKP model results with the anti-trapping flux. The results for W/d_0=0.5 and 2 are very close to each other. This suggests that capillary length is the smallest length scale that can be considered in phase field modeling and there is no point in choosing the interface width values smaller than that. Figure 5.15 addresses a big issue about the PP phase field model which is limitations in choosing the interface width and A parameter. Choosing a larger parameter A and smaller interface width does not alwys improve the results. Also, the effectiveness of a phase field model is defined by how the model performs for diffuse interfaces with interface width larger than the sharp interface. These results presents than the increase of W/d_0 from 2 to 8 suddenly turns PP phase field model into EFKP model with the anti-trapping term which was not able to predict solute trapping.

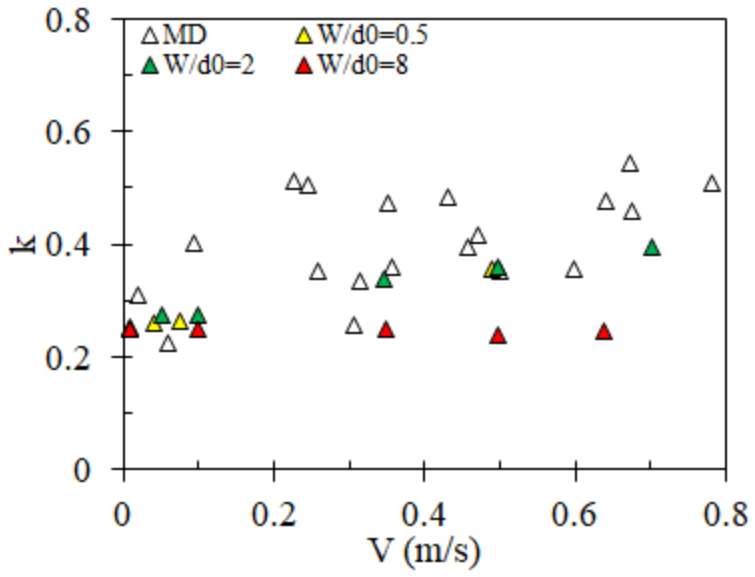

Figure 5.15. The velocity-dependent partition coefficient for solidification of Ti-0.9atom%Ni from i) MD simulations ii) PP model with full solute drag considering β=0.02 and using W/d_0=0.5 iii) PP model with full solute drag considering β=0.02 and using W/d_0=2 iii) PP model with full solute drag considering β=0.02 and using W/d_0=8

5.3 Conclusion

Two slightly different phase field models were implemented and tested on their ability at predicting the solidification of pure titanium velocity at various undercoolings. For undercoolings below 150K, when using the classical phase field model, in which the driving force term in the bulk free energy function was considered to vary linearly with undercooling, the simulation and experiment data are in good agreement. However, at larger undercoolings the simulation results show significant deviations from experimental data. By modifying the thermodynamic driving force term in the free energy definition based on the Bragard *et al*. model, the phase field method not only predicts the solidification velocity consistent with the experiments over a large spectrum of undercoolings, but also provides good estimation of the solid-liquid interface temperature consistent with the Gibbs-Thomson equation. In addition to solidification kinetics, we have studied the effect of anisotropy parameters on the dendritic morphology and growth rate at small and large

undercoolings. For both undercoolings, modifications of capillary and kinetic anisotropies affected the dendrite shapes and the tip velocity, while it did not change the solidification velocity significantly. Moreover, the simulations showed that the effect of capillary anisotropy is larger for small undercoolings, while the kinetic effect becomes more dominant for larger undercoolings.

The results of our study demonstrate that MD simulations combined with phase field modeling has the potential to provide quantitative, parameter-free, predictions on multiple features characterizing solidification behavior in titanium.

We also tested EFKP and PP phase field models to study the solidification of Ti-0.9atom%Ni and Ti-3.22atom%Ni. All the parameters used in both phase field models are calculated by MD simulations.

EFKP model is studies by two different approaches. In first approach, we simulated the original model and in the second approach, we eliminated the anti-trapping flux term. This enables us to predict solute trapping with phase field modeling, which was not possible with the original model. PP model also have two different form. First form considers full solute drag and the second considers no-solute drag. The comparison of these two forms of PP model shows that the results of their predictions are so close to each other. But the PP model is very sensitive for the interface width value. Even if the predicted partition coefficient is fit to the CG mode, for some interface width choices we might not get any solute trapping.

6 CONCLUSION AND RECOMMENDATION

In this research, we studied non-equilibrium solidification happening during the rapid solidification of pure Ti and Ni-Ti alloys. For this first we developed 2NN MEAM potentials for Ti, Ni, and the Ti-Ni binary systems that improve the crystal-melt (CM) interfacial properties for pure and binary systems and the high temperature portions of the binary system CM equilibrium phase diagram for both the nickel-rich and titanium-rich compositions. The reliability of the potentials for pure Ti and pure Ni were tested by comparison of various physical quantities including structural properties, elastic constants, point-defect properties, surface energies, temperatures and enthalpies of phase transformations, and thermodynamic and dynamic properties of the liquid phases with experimental and DFT data. The binary potential was fit to the liquid enthalpies of mixing and the CM portions of the phase diagram in the Ni-rich and Ti-rich regions. The fitted binary potential for Ti-Ni was also tested against various non-fitted properties such as lattice parameters, formation energies of different intermetallic compounds, and the temperature dependence of liquid density at various concentrations.

Using our potential, we performed MD simulations to calculate the interfacial free energy, kinetic coefficient and its anisotropy to parameterize phase field models. Kinetic coefficient is estimated by fitting the MD results to the analytical relation which connects the non-equilibrium and velocity-dependent concentration profile, to the equilibrium liquidus and solidus concentrations, interface temperature, and interface velocity. This requires knowing the interface mobility, drag coefficient, and velocity-dependent partition coefficient. Combined thermodynamic integration for pure Ti with semi-grand canonical ensemble (SGC) simulations of alloys are used to estimate all the abovementioned quantities.

Then phase field simulation on both pure Ti and Ti-Ni dilute binary alloys is performed. For pure Ti, at larger undercoolings, the simulation results show significant deviations from experimental data. By modifying the thermodynamic driving force term in the free energy definition based on the Bragard *et al*. model, the phase field method predicts the solidification velocity consistent with the experiments over a large spectrum of undercoolings.

Comparison of two different phase field models with the MD results shows that PP model perform better than the well-known EFKP. Meanwhile, we have reported an important issue for the PP model. The results for this model is very dependent to the interface width choices. And for large interface width values, this model predicts no solute trapping. So as comparison of these models, the EFKP model with no anti-trapping flux presents a much more reliable results.

For the future work, I would recommend:

A- Calculating the kinetic coefficient and interface energy in MD simulation during the rapid solidification

B- Performing directional rapid solidification in MD to compare with phase field simulations.

C- Phase field modeling of ternary alloys

7 REFERENCES

[1] C. Cáceres, G. Wang, Dendrite cell size and ductility of Al-Si-Mg casting alloys: Spear and Gardner revisited, International Journal of Cast Metals Research, 9 (1996) 157-162.

[2] D. Bouchard, J.S. Kirkaldy, Prediction of dendrite arm spacings in unsteady-and steady-state heat flow of unidirectionally solidified binary alloys, Metallurgical and Materials Transactions B, 28 (1997) 651-663.

[3] M.S. Park, Phase-field Models for Solidification and Solid/Liquid Interactions, 2011.

[4] J.J. Hoyt, M. Asta, A. Karma, Atomistic and continuum modeling of dendritic solidification, Materials Science and Engineering: R: Reports, 41 (2003) 121-163.

[5] G.J. Fix, Phase field methods for free boundary problems, DOI (1982).

[6] J.S. Langer, MODELS OF PATTERN FORMATION IN FIRST-ORDER PHASE TRANSITIONS, Directions in Condensed Matter Physics, WORLD SCIENTIFIC2013, pp. 165-186.

[7] M. Mamivand, M. Asle Zaeem, H. El Kadiri, L.-Q. Chen, Phase field modeling of the tetragonal-to-monoclinic phase transformation in zirconia, Acta Materialia, 61 (2013) 5223-5235.

[8] M. Mamivand, M. Asle Zaeem, H. El Kadiri, Phase field modeling of stress-induced tetragonal-to-monoclinic transformation in zirconia and its effect on transformation toughening, Acta Materialia, 64 (2014) 208-219.

[9] A. Emdadi, W.G. Fahrenholtz, G.E. Hilmas, M. Asle Zaeem, A modified phase-field model for quantitative simulation of crack propagation in single-phase and multi-phase materials, Engineering Fracture Mechanics, 200 (2018) 339-354.

[10] N. Moelans, B. Blanpain, P. Wollants, An introduction to phase-field modeling of microstructure evolution, Calphad, 32 (2008) 268-294.

[11] S. Ingo, Phase-field models in materials science, Modelling and Simulation in Materials Science and Engineering, 17 (2009) 073001.

[12] B. Jacob, Z. Mohsen Asle, T. Michael, A phase-field model to study the effects of temperature change on shape evolution of γ -hydrides in zirconium, Journal of Physics D: Applied Physics, 49 (2016) 405302.

[13] J. Bair, M. Asle Zaeem, D. Schwen, Formation path of δ hydrides in zirconium by multiphase field modeling, Acta Materialia, 123 (2017) 235-244.

[14] S. Kavousi, B.R. Novak, M.A. Zaeem, D. Moldovan, Combined molecular dynamics and phase field simulation investigations of crystal-melt interfacial properties and dendritic solidification of highly undercooled titanium, Computational Materials Science, 163 (2019) 218-229.

[15] B. Echebarria, R. Folch, A. Karma, M. Plapp, Quantitative phase-field model of alloy solidification, Physical Review E, 70 (2004) 061604.

[16] A. Karma, W.-J. Rappel, Quantitative phase-field modeling of dendritic growth in two and three dimensions, Physical Review E, 57 (1998) 4323-4349.

[17] W. J. Boettinger, J. A. Warren, C. Beckermann, A. Karma, Phase-Field Simulation of Solidification, Annual Review of Materials Research, 32 (2002) 163-194.

[18] P.K. Galenko, E.V. Abramova, D. Jou, D.A. Danilov, V.G. Lebedev, D.M. Herlach, Solute trapping in rapid solidification of a binary dilute system: a phase-field study, Physical review. E, Statistical, nonlinear, and soft matter physics, 84 (2011) 041143.

[19] A.A. Wheeler, W.J. Boettinger, G.B. McFadden, Phase-field model for isothermal phase transitions in binary alloys, Physical Review A, 45 (1992) 7424-7439.

[20] L. Zhang, E.V. Danilova, I. Steinbach, D. Medvedev, P.K. Galenko, Diffuse-interface modeling of solute trapping in rapid solidification: Predictions of the hyperbolic phase-field model and parabolic model with finite interface dissipation, Acta Materialia, 61 (2013) 4155-4168.

[21] A. Karma, W.-J. Rappel, Phase-field method for computationally efficient modeling of solidification with arbitrary interface kinetics, Physical Review E, 53 (1996) R3017-R3020.

[22] J. Bragard, A. Karma, Y.H. Lee, M. Plapp, Linking Phase-Field and Atomistic Simulations to Model Dendritic Solidification in Highly Undercooled Melts, Interface Science, 10 (2002) 121-136.

[23] N. Ahmad, A. Wheeler, W.J. Boettinger, G.B. McFadden, Solute trapping and solute drag in a phase-field model of rapid solidification, Physical Review E, 58 (1998) 3436.

[24] D. Danilov, B. Nestler, Phase-field modelling of solute trapping during rapid solidification of a Si–As alloy, Acta Materialia, 54 (2006) 4659-4664.

[25] J. Dantzig, P.d. Napoli, J. Friedli, M. Rappaz, Dendritic Growth Morphologies in Al-Zn Alloys—Part II: Phase-Field Computations, Metallurgical and Materials Transactions A, 44 (2013).

[26] V. Fallah, M. Amoorezaei, N. Provatas, S.F. Corbin, A. Khajepour, Phase-field simulation of solidification morphology in laser powder deposition of Ti–Nb alloys, Acta Materialia, 60 (2012) 1633-1646.

[27] T. Keller, G. Lindwall, S. Ghosh, L. Ma, B.M. Lane, F. Zhang, U.R. Kattner, E.A. Lass, J.C. Heigel, Y. Idell, M.E. Williams, A.J. Allen, J.E. Guyer, L.E. Levine, Application of finite element, phase-field, and CALPHAD-based methods to additive manufacturing of Ni-based superalloys, Acta Materialia, 139 (2017) 244-253.

[28] S. Sahoo, K. Chou, Phase-field simulation of microstructure evolution of Ti–6Al–4V in electron beam additive manufacturing process, Additive Manufacturing, 9 (2016) 14-24.

[29] W.-L. Chan, R.S. Averback, D.G. Cahill, Y. Ashkenazy, Solidification Velocities in Deeply Undercooled Silver, Physical Review Letters, 102 (2009) 095701.

[30] G.H. Rodway, J.D. Hunt, Thermoelectric investigation of solidification of lead II. Lead alloys, Journal of Crystal Growth, 112 (1991) 563-570.

[31] M.E. Glicksman, R.J. Schaefer, J.D. Ayers, Dendritic growth-A test of theory, Metallurgical Transactions A, 7 (1976) 1747-1759.

[32] C.Y. Yap, C.K. Chua, Z.L. Dong, Z.H. Liu, D.Q. Zhang, L.E. Loh, S.L. Sing, Review of selective laser melting: Materials and applications, Applied Physics Reviews, 2 (2015) 041101.

[33] M. Barmatz, Overview of Containerless Processing Technologies, 1982.

[34] W. Kurz, B. Giovanola, R. Trivedi, Theory of microstructural development during rapid solidification, Acta Metallurgica, 34 (1986) 823-830.

[35] T. Pinomaa, N. Provatas, Quantitative phase field modeling of solute trapping and continuous growth kinetics in quasi-rapid solidification, Acta Materialia, 168 (2019) 167-177.

[36] M.J. Aziz, W.J. Boettinger, On the transition from short-range diffusion-limited to collision-limited growth in alloy solidification, Acta Metallurgica et Materialia, 42 (1994) 527-537.

[37] M.I. Mendelev, M. Asta, M.J. Rahman, J.J. Hoyt, Development of interatomic potentials appropriate for simulation of solid–liquid interface properties in Al–Mg alloys, Philosophical Magazine, 89 (2009) 3269-3285.

[38] D.A. Porter, K.E. Easterling, M. Sherif, Phase Transformations in Metals and Alloys, (Revised Reprint), CRC press2009.

[39] N. PROVATAS, M. GREENWOOD, B. ATHREYA, N. GOLDENFELD, J. DANTZIG, MULTISCALE MODELING OF SOLIDIFICATION: PHASE-FIELD METHODS TO ADAPTIVE MESH REFINEMENT, International Journal of Modern Physics B, 19 (2005) 4525-4565.

[40] M.J. Aziz, T. Kaplan, Continuous growth model for interface motion during alloy solidification, Acta Metallurgica, 36 (1988) 2335-2347.

[41] J.C. Baker, Interfacial partitioning during solidification, Massachusetts Institute of Technology, 1970.

[42] Atomistic Simulations of Solute Trapping and Solute Drag, Solidification of Containerless Undercooled Melts, pp. 363-380.

[43] S.L. Sobolev, Local-nonequilibrium model for rapid solidification of undercooled melts, Physics Letters A, 199 (1995) 383-386.

[44] S.L. Sobolev, Rapid solidification under local nonequilibrium conditions, Physical Review E, 55 (1997) 6845-6854.

[45] P. Galenko, S. Sobolev, Local nonequilibrium effect on undercooling in rapid solidification of alloys, Physical Review E, 55 (1997) 343-352.

[46] M.J. Aziz, J.Y. Tsao, M.O. Thompson, P.S. Peercy, C.W. White, Solute Trapping: Comparison of Theory with Experiment, Physical Review Letters, 56 (1986) 2489-2492.

[47] S.J. Cook, P. Clancy, Impurity segregation in Lennard-Jones A/AB heterostructures. I. The effect of lattice strain, The Journal of Chemical Physics, 99 (1993) 2175-2191.

[48] W. Olsen, R. Hultgren, The effect of the rate of cooling rate on the homogeneity of solid solution, Trans AIME, 188 (1950) 1223.

[49] G. Falkenhagen, W. Hofmann, * DIE AUSWIRKUNG EXTREM HOHER ABKUHLUNGSGESCHWINDIGKEIT AUF DIE ERSTARRUNG UND DAS GEFUGE BINARER LEGIERUNGEN, Zeitschrift fur Metallkunde, 43 (1952) 69-81.

[50] P. Duwez, R. Willens, W. Klement Jr, Continuous series of metastable solid solutions in silver-copper alloys, Journal of Applied Physics, 31 (1960) 1136-1137.

[51] P. Duwez, R. Willens, W. Klement Jr, Metastable Electron Compound in Ag-Ge Alloys, Journal of Applied Physics, 31 (1960) 1137-1137.

[52] J.A. Kittl, P.G. Sanders, M.J. Aziz, D.P. Brunco, M.O. Thompson, Complete experimental test of kinetic models for rapid alloy solidification, Acta Materialia, 48 (2000) 4797-4811.

[53] K. Eckler, R.F. Cochrane, D.M. Herlach, B. Feuerbacher, M. Jurisch, Evidence for a transition from diffusion-controlled to thermally controlled solidification in metallic alloys, Physical Review B, 45 (1992) 5019-5022.

[54] V.V. Bulatov, W. Cai, Computer simulations of dislocations. [electronic resource], Oxford ; New York : Oxford University Press, 2006.2006.

[55] S.G. Kim, W.T. Kim, J.S. Lee, M. Ode, T. Suzuki, Large Scale Simulation of Dendritic Growth in Pure Undercooled Melt by Phase-field Model, ISIJ International, 39 (1999) 335-340.

[56] J.A. Warren, W.J. Boettinger, Prediction of dendritic growth and microsegregation patterns in a binary alloy using the phase-field method, Acta Metallurgica et Materialia, 43 (1995) 689-703.

[57] N. Provatas, K. Elder, Phase-field methods in materials science and engineering, John Wiley & Sons2011.

[58] R. Kobayashi, Modeling and numerical simulations of dendritic crystal growth, Physica D: Nonlinear Phenomena, 63 (1993) 410-423.

[59] R. Kobayashi, A Numerical Approach to Three-Dimensional Dendritic Solidification, Experimental Mathematics, 3 (1994) 59-81.

[60] W.J. Boettinger, J.A. Warren, The phase-field method: simulation of alloy dendritic solidification during recalescence, Metallurgical and Materials Transactions A, 27 (1996) 657-669.

[61] G. Caginalp, Phase Field Models and Sharp Interface Limits: Some Differences in Subtle Situations, Rocky Mountain J. Math., 21 (1991) 603-615.

[62] S. Wang, M.A. Zaeem, M.F. Horstemeyer, P.T. Wang, Investigating thermal effects on morphological evolution during crystallisation of hcp metals: three-dimensional phase field study, Materials Technology, 27 (2012) 355-363.

[63] O. Penrose, P.C. Fife, Thermodynamically consistent models of phase-field type for the kinetic of phase transitions, Physica D: Nonlinear Phenomena, 43 (1990) 44-62.

[64] S. Kavousi, D. Moldovan, Phase Field Modeling of Solidification in Single Component Systems, ASME 2017 International Mechanical Engineering Congress and Exposition, American Society of Mechanical Engineers, 2017, pp. V014T011A034-V014T011A034.

[65] J. Ramirez, C. Beckermann, A. Karma, H.-J. Diepers, Phase-field modeling of binary alloy solidification with coupled heat and solute diffusion, Physical Review E, 69 (2004) 051607.

[66] S. Ghosh, L. Ma, N. Ofori-Opoku, J.E. Guyer, On the primary spacing and microsegregation of cellular dendrites in laser deposited Ni–Nb alloys, Modelling and Simulation in Materials Science and Engineering, 25 (2017) 065002.

[67] K. Reuther, S. Hubig, I. Steinbach, M. Rettenmayr, Solute trapping in non-equilibrium solidification: A comparative model study, Materialia, 6 (2019) 100256.

[68] P.K. Galenko, E.V. Abramova, D. Jou, D.A. Danilov, V.G. Lebedev, D.M. Herlach, Solute trapping in rapid solidification of a binary dilute system: A phase-field study, Physical Review E, 84 (2011) 041143.

[69] V.G. Lebedev, E.V. Abramova, D.A. Danilov, P.K. Galenko, Phase-field modeling of solute trapping: comparative analysis of parabolic and hyperbolic models, International Journal of Materials Research, 101 (2010) 473-479.

[70] W. Kurz, D.J. Fisher, Dendrite growth at the limit of stability: tip radius and spacing, Acta Metallurgica, 29 (1981) 11-20.

[71] Y.-J. Liang, A. Li, X. Cheng, X.-T. Pang, H.-M. Wang, Prediction of primary dendritic arm spacing during laser rapid directional solidification of single-crystal nickel-base superalloys, Journal of Alloys and Compounds, 688 (2016) 133-142.

[72] X.W. Hu, S.M. Li, W.J. Chen, S.F. Gao, L. Liu, H.Z. Fu, Primary dendrite arm spacing during unidirectional solidification of Pb–Bi peritectic alloys, Journal of Alloys and Compounds, 484 (2009) 631-636.

[73] M.H. Burden, J.D. Hunt, Cellular and dendritic growth. II, Journal of Crystal Growth, 22 (1974) 109-116.

[74] G. Raabe, Molecular Simulation Studies on Thermophysical Properties, Springer2017.

[75] L. Verlet, Computer "Experiments" on Classical Fluids. I. Thermodynamical Properties of Lennard-Jones Molecules, Physical Review, 159 (1967) 98-103.

[76] D. Frenkel, B. Smit, Understanding molecular simulation: from algorithms to applications, Elsevier2001.

[77] M.W. Finnis, J.E. Sinclair, A simple empirical N-body potential for transition metals, Philosophical Magazine A, 50 (1984) 45-55.

[78] M.S. Daw, M.I. Baskes, Embedded-atom method: Derivation and application to impurities, surfaces, and other defects in metals, Physical Review B, 29 (1984) 6443-6453.

[79] M.I. Baskes, Modified embedded-atom potentials for cubic materials and impurities, Physical Review B, 46 (1992) 2727-2742.

[80] B.-J. Lee, M.I. Baskes, Second nearest-neighbor modified embedded-atom-method potential, Physical Review B, 62 (2000) 8564-8567.

[81] B.-J. Lee, J.-H. Shim, M.I. Baskes, Semiempirical atomic potentials for the fcc metals Cu, Ag, Au, Ni, Pd, Pt, Al, and Pb based on first and second nearest-neighbor modified embedded atom method, Physical Review B, 68 (2003) 144112.

[82] B.-J. Lee, M.I. Baskes, H. Kim, Y. Koo Cho, Second nearest-neighbor modified embedded atom method potentials for bcc transition metals, Physical Review B, 64 (2001) 184102.

[83] M.I. Baskes, J.E. Angelo, C.L. Bisson, Atomistic calculations of composite interfaces, Modelling and Simulation in Materials Science and Engineering, 2 (1994) 505.

[84] P. Vinet, J.R. Smith, J. Ferrante, J.H. Rose, Temperature effects on the universal equation of state of solids, Physical Review B, 35 (1987) 1945-1953.

[85] J.Q. Broughton, G.H. Gilmer, Molecular dynamics of the crystal–fluid interface. V. Structure and dynamics of crystal–melt systems, The Journal of Chemical Physics, 84 (1986) 5749-5758.

[86] X.-M. Bai, M. Li, Calculation of solid-liquid interfacial free energy: A classical nucleation theory based approach, The Journal of Chemical Physics, 124 (2006) 124707.

[87] S. Angioletti-Uberti, M. Ceriotti, P.D. Lee, M.W. Finnis, Solid-liquid interface free energy through metadynamics simulations, Physical Review B, 81 (2010).

[88] D. Şopu, J. Rogal, R. Drautz, Thermodynamic and kinetic solid-liquid interface properties from transition path sampling, The Journal of Chemical Physics, 145 (2016) 244703.

[89] J.R. Espinosa, C. Vega, E. Sanz, The mold integration method for the calculation of the crystal-fluid interfacial free energy from simulations, The Journal of Chemical Physics, 141 (2014) 134709.

[90] U.R. Pedersen, Direct calculation of the solid-liquid Gibbs free energy difference in a single equilibrium simulation, The Journal of Chemical Physics, 139 (2013) 104102.

[91] J.J. Hoyt, M. Asta, A. Karma, Method for Computing the Anisotropy of the Solid-Liquid Interfacial Free Energy, Physical Review Letters, 86 (2001) 5530-5533.

[92] L. Wu, B. Xu, Q. Li, W. Liu, M. Li, Anisotropic crystal–melt interfacial energy and stiffness of aluminum, Journal of Materials Research, 30 (2015) 1827-1835.

[93] E. Asadi, M.A. Zaeem, S. Nouranian, M.I. Baskes, Quantitative modeling of the equilibration of two-phase solid-liquid Fe by atomistic simulations on diffusive time scales, Physical Review B, 91 (2015) 024105.

[94] E. Asadi, M. Asle Zaeem, The anisotropy of hexagonal close-packed and liquid interface free energy using molecular dynamics simulations based on modified embedded-atom method, Acta Materialia, 107 (2016) 337-344.

[95] W.G. Hoover, B.L. Holian, Kinetic moments method for the canonical ensemble distribution, Physics Letters A, 211 (1996) 253-257.

[96] Y. Mishin, Calculation of the γ/γ′ interface free energy in the Ni–Al system by the capillary fluctuation method, Modelling and Simulation in Materials Science and Engineering, 22 (2014) 045001.

[97] M. Asta, J. Hoyt, A. Karma, Calculation of alloy solid-liquid interfacial free energies from atomic-scale simulations, Physical Review B, 66 (2002) 100101.

[98] T. Frolov, Y. Mishin, Solid-liquid interface free energy in binary systems: Theory and atomistic calculations for the (110) Cu–Ag interface, The Journal of Chemical Physics, 131 (2009) 054702.

[99] J. Rahman, Atomistic Simulations for computing solid liquid interface properties of the Al-Mg system, 2009.

[100] Y. Yang, H. Humadi, D. Buta, B.B. Laird, D. Sun, J.J. Hoyt, M. Asta, Atomistic simulations of nonequilibrium crystal-growth kinetics from alloy melts, Physical review letters, 107 (2011) 025505.

[101] F. Celestini, J.-M. Debierre, Measuring kinetic coefficients by molecular dynamics simulation of zone melting, Physical Review E, 65 (2002) 041605.

[102] J. Monk, Y. Yang, M.I. Mendelev, M. Asta, J.J. Hoyt, D.Y. Sun, Determination of the crystal-melt interface kinetic coefficient from molecular dynamics simulations, Modelling and Simulation in Materials Science and Engineering, 18 (2010) 015004.

[103] D.Y. Sun, M. Asta, J.J. Hoyt, Kinetic coefficient of Ni solid-liquid interfaces from molecular-dynamics simulations, Physical Review B, 69 (2004) 024108.

[104] E. Asadi, M. Asle Zaeem, S. Nouranian, M.I. Baskes, Quantitative modeling of the equilibration of two-phase solid-liquid Fe by atomistic simulations on diffusive time scales, Physical Review B, 91 (2015) 024105.

[105] J.J. Hoyt, M. Asta, Atomistic computation of liquid diffusivity, solid-liquid interfacial free energy, and kinetic coefficient in Au and Ag, Physical Review B, 65 (2002) 214106.

[106] J.J. Hoyt, B. Sadigh, M. Asta, S.M. Foiles, Kinetic phase field parameters for the Cu–Ni system derived from atomistic computations, Acta Materialia, 47 (1999) 3181-3187.

[107] R. Ramakrishnan, R. Sankarasubramanian, Crystal-melt kinetic coefficients of Ni3Al, Acta Materialia, 127 (2017) 25-32.

[108] W.S. Lai, B.X. Liu, Lattice stability of some Ni-Ti alloy phases versus their chemical composition and disordering, Journal of Physics: Condensed Matter, 12 (2000) L53.

[109] G. Ren, H. Sehitoglu, Interatomic potential for the NiTi alloy and its application, Computational Materials Science, 123 (2016) 19-25.

[110] D. Mutter, P. Nielaba, Simulation of structural phase transitions in NiTi, Physical Review B, 82 (2010) 224201.

[111] Y. Zhong, K. Gall, T. Zhu, Atomistic study of nanotwins in NiTi shape memory alloys, Journal of Applied Physics, 110 (2011) 033532.

[112] C. Kexel, A.V. Verkhovtsev, G.B. Sushko, A.V. Korol, S. Schramm, A.V. Solov'yov, Toward the Exploration of the NiTi Phase Diagram with a Classical Force Field, The Journal of Physical Chemistry C, 120 (2016) 25043-25052.

[113] D. Farkas, D. Roqueta, A. Vilette, K. Ternes, Atomistic simulations in ternary Ni - Ti - Al alloys, Modelling and Simulation in Materials Science and Engineering, 4 (1996) 359.

[114] Y. Li, J. Li, J. Liu, B. Liu, Atomic approach to the optimized compositions of Ni–Nb–Ti glassy alloys with large glass-forming ability, RSC Advances, 5 (2015) 3054-3062.

[115] H. Ishida, Y. Hiwatari, MD simulation of martensitic transformations in TiNi alloys with MEAM, Molecular Simulation, 33 (2007) 459-461.

[116] K.-I. Saitoh, K. Kubota, T. Sato, Atomic-level structural change in Ni-Ti alloys under martensite and amorphous transformations, 2010.

[117] W.-S. Ko, B. Grabowski, J. Neugebauer, Development and application of a Ni-Ti interatomic potential with high predictive accuracy of the martensitic phase transition, Physical Review B, 92 (2015) 134107.

[118] Y.-K. Kim, H.-K. Kim, W.-S. Jung, B.-J. Lee, Development and application of Ni-Ti and Ni-Al-Ti 2NN-MEAM interatomic potentials for Ni-base superalloys, Computational Materials Science, 139 (2017) 225-233.

[119] M. Muralles, S.-D. Park, S.Y. Kim, B. Lee, Phase transformations, detwinning and superelasticity of shape-memory NiTi from MEAM with practical capability, Computational Materials Science, 130 (2017) 138-143.

[120] J.J. Valencia, P. Quested, Thermophysical properties, Modeling for Casting and Solidification Processing, 189 (2001).

[121] H. Okamoto, Phase diagrams for binary alloys, ASM International, 268 (2000).

[122] T. Hara, T. Ohba, K. Otsuka, M. Nishida, Phase Transformation and Crystal Structures of Ti₂Ni₃ Precipitates in Ti–Ni Alloys, Materials Transactions, JIM, 38 (1997) 277-284.

[123] O. Kubaschewski, H. Villa, W. Dench, The reaction of titanium tetrachloride with hydrogen in contact with various refractories, Transactions of the Faraday Society, 52 (1956) 214-222.

[124] O. Mercier, K.N. Melton, G. Gremaud, J. Hägi, Single-crystal elastic constants of the equiatomic NiTi alloy near the martensitic transformation, Journal of Applied Physics, 51 (1980) 1833-1834.

[125] S.D. Prokoshkin, A.V. Korotitskiy, V. Brailovski, S. Turenne, I.Y. Khmelevskaya, I.B. Trubitsyna, On the lattice parameters of phases in binary Ti–Ni shape memory alloys, Acta Materialia, 52 (2004) 4479-4492.

[126] S. Plimpton, Fast Parallel Algorithms for Short-Range Molecular Dynamics, Journal of Computational Physics, 117 (1995) 1-19.

[127] C. Kittel, Introduction to Solid State Physics, 8 ed., Wiley2004.

[128] C.S. Barrett, T.B. Massalski, Structure of metals; crystallographic methods, principles, and data, McGraw-Hill, New York, 1966.

[129] G. Simmons, H. Wang, Single crystal elastic constants and calculated aggregate properties: a handbook, M.I.T. Press, Cambridge, Mass., 1971.

[130] R.G. Hennig, T.J. Lenosky, D.R. Trinkle, S.P. Rudin, J.W. Wilkins, Classical potential describes martensitic phase transformations between the $\ensuremath{\alpha}$, $\ensuremath{\beta}$, and $\ensuremath{\omega}$ titanium phases, Physical Review B, 78 (2008) 054121.

[131] E. Hashimoto, E.A. Smirnov, T. Kino, Temperature dependence of the Doppler-broadened lineshape of positron annihilation in α-Ti, Journal of Physics F: Metal Physics, 14 (1984) L215.

[132] W.R. Tyson, W.A. Miller, Surface free energies of solid metals: Estimation from liquid surface tension measurements, Surface Science, 62 (1977) 267-276.

[133] F.R.d. Boer, R. Boom, W.C.M. Mattens, A.R. Miedema, A.K. Niessen, Cohesion in metals : transition metal alloys, North-Holland, Amsterdam, 1989.

[134] R.J. Birgeneau, J. Cordes, G. Dolling, A.D.B. Woods, Normal Modes of Vibration in Nickel, Physical Review, 136 (1964) A1359-A1365.

[135] W. Wycisk, M. Feller-Kniepmeier, Quenching experiments in high purity Ni, Journal of Nuclear Materials, 69-70 (1978) 616-619.

[136] L. Vitos, A.V. Ruban, H.L. Skriver, J. Kollár, The surface energy of metals, Surface Science, 411 (1998) 186-202.

[137] R. Namakian, G. Voyiadjis, An atomic displacive model for {1012}〈1011〉 twinning in hexagonal close packed metals with the emphasis on the role of partial stacking faults in formation of {1012} twins, Acta Materialia, 150 (2018).

[138] D.Y. Sun, M.I. Mendelev, C.A. Becker, K. Kudin, T. Haxhimali, M. Asta, J.J. Hoyt, A. Karma, D.J. Srolovitz, Crystal-melt interfacial free energies in hcp metals: A molecular dynamics study of Mg, Physical Review B, 73 (2006) 024116.

[139] A. Cezairliyan, A. Miiller, Thermodynamic Study of the a~{3 Phase Transformation in Titanium by Pulse Heating Method, JOURNAL OF RESEARCH of the National Bureau of Standards, 83 (1978).

[140] M. Cormier, F. Claisse, Beta-alpha phase transformation in Ti and Ti□ O alloys, Journal of the Less Common Metals, 34 (1974) 181-189.

[141] P.D. Desai, Thermodynamic properties of titanium, International Journal of Thermophysics, 8 (1987) 781-794.

[142] M. Martynyuk, V. Tsapkov, Electric resistance, enthalpy and phase transformations of titanium, zirconium and hafnium during pulse heating, Izvestiya Akademii Nauk SSSR, Metally, DOI (1974) 181-188.

[143] S.R. Nishitani, H. Kawabe, M. Aoki, First-principles calculations on bcc–hcp transition of titanium, Materials Science and Engineering: A, 312 (2001) 77-83.

[144] J.A. Dean, N.A. Lange, Lange's handbook of chemistry, McGraw-Hill, New York :, 1973.

[145] E.Y. Kulyamina, V.Y. Zitserman, L.R. Fokin, Titanium Melting Curve: Data Consistency Assessment, Problems and Achievements, Technical Physics, 63 (2018) 369-373.

[146] E.A. Brandes, G.B. Brook, 14 - General physical properties, Smithells Metals Reference Book (Seventh Edition), Butterworth-Heinemann, Oxford, 1992, pp. 14-11-14-43.

[147] J. Brillo, I. Egry, Density Determination of Liquid Copper, Nickel, and Their Alloys, International Journal of Thermophysics, 24 (2003) 1155-1170.

[148] T. Ishikawa, P.-F. Paradis, J.T. Okada, Y. Watanabe, Viscosity measurements of molten refractory metals using an electrostatic levitator, Measurement Science and Technology, 23 (2012) 025305.

[149] J. Horbach, R.E. Rozas, T. Unruh, A. Meyer, Improvement of computer simulation models for metallic melts via quasielastic neutron scattering: A case study of liquid titanium, Physical Review B, 80 (2009) 212203.

[150] C.B. Alcock, V.P. Itkin, M.K. Horrigan, Vapour Pressure Equations for the Metallic Elements: 298–2500K, Canadian Metallurgical Quarterly, 23 (1984) 309-313.

[151] H. Wang, S. Yang, B. Wei, Density and structure of undercooled liquid titanium, Chinese Science Bulletin, 57 (2012) 719-723.

[152] Y. Hanbyeol, P. Cheolmin, J. Sangho, L. Sooheyong, L. Geun Woo, Uncertainty evaluation for density measurements of molten Ni, Zr, Nb and Hf by using a containerless method, Metrologia, 52 (2015) 677.

[153] P.-F. Paradis, T. Ishikawa, S. Yoda, Non-Contact Measurements of Surface Tension and Viscosity of Niobium, Zirconium, and Titanium Using an Electrostatic Levitation Furnace, International Journal of Thermophysics, 23 (2002) 825-842.

[154] S. Sauerland, G. Lohöfer, I. Egry, Surface tension measurements on levitated liquid metal drops, Journal of Non-Crystalline Solids, 156-158 (1993) 833-836.

[155] A. Meyer, The measurement of self-diffusion coefficients in liquid metals with quasielastic neutron scattering, EPJ Web of Conferences, 83 (2015) 01002.

[156] B.G. del Rio, O. Rodriguez, L.E. González, D.J. González, First principles determination of static, dynamic and electronic properties of liquid Ti near melting, Computational Materials Science, 139 (2017) 243-251.

[157] H. Zhang, S.L. Shang, W.Y. Wang, Y. Wang, X.D. Hui, L.Q. Chen, Z.K. Liu, Structure and energetics of Ni from ab initio molecular dynamics calculations, Computational Materials Science, 89 (2014) 242-246.

[158] J. Frenzel, A. Wieczorek, I. Opahle, B. Maaß, R. Drautz, G. Eggeler, On the effect of alloy composition on martensite start temperatures and latent heats in Ni–Ti-based shape memory alloys, Acta Materialia, 90 (2015) 213-231.

[159] Y. Esin, M. Valishev, A. Ermakov, P. Gel'd, M. Petrushevskii, The Enthalpies of Formation of Liquid Germanium--Titanium and Nickel--Titanium Alloys, Russ. J. Phys. Chem., 55 (1981) 421-422.

[160] J.C. Gachon, J. Hertz, Enthalpies of formation of binary phases in the systems FeTi, FeZr, CoTi, CoZr, NiTi, and NiZr, by direct reaction calorimetry, Calphad, 7 (1983) 1-12.

[161] A. Pasturel, C. Colinet, D.N. Manh, A.T. Paxton, M. van Schilfgaarde, Electronic structure and phase stability study in the Ni-Ti system, Physical Review B, 52 (1995) 15176-15190.

[162] X. Huang, G.J. Ackland, K.M. Rabe, Crystal structures and shape-memory behaviour of NiTi, Nature Materials, 2 (2003) 307.

[163] D. Holec, M. Friák, A. Dlouhý, J. Neugebauer, Ab initio study of pressure stabilized NiTi allotropes: Pressure-induced transformations and hysteresis loops, Physical Review B, 84 (2011) 224119.

[164] M. Kök, F. Dağdelen, A. Aydoğdu, Y. Aydoğdu, The change of transformation temperature on NiTi shape memory alloy by pressure and thermal ageing, Journal of Physics: Conference Series, IOP Publishing, 2016, pp. 012011.

[165] J.C. Gachon, M. Notin, J. Hertz, The enthalphy of mixing of the intermediate phases in the systems FeTi, CoTi, and NiTi by direct reaction calorimetry, Thermochimica Acta, 48 (1981) 155-164.

[166] A. Taylor, R.W. Floyd, Precision measurements of lattice parameters of non-cubic crystals, Acta Crystallographica, 3 (1950) 285-289.

[167] G.A. Yurko, J.W. Barton, J.G. Parr, The crystal structure of Ti2Ni, Acta Crystallographica, 12 (1959) 909-911.

[168] M. Watanabe, M. Adachi, H. Fukuyama, Density measurement of Ti-X(X=Cu, Ni) melts and thermodynamic correlations, 2018.

[169] J. Brillo, T. Schumacher, K. Kajikawa, Density of Liquid Ni-Ti and a New Optical Method for its Determination, Metallurgical and Materials Transactions A, 50 (2019) 924-935.

[170] U. Thiedemann, M. Rösner-Kuhn, K. Drewes, G. Kuppermann, M.G. Frohberg, Temperature dependence of the mixing enthalpy of liquid Ti–Ni and Fe–Ti–Ni alloys, Journal of Non-Crystalline Solids, 250-252 (1999) 329-335.

[171] L. Kaufman, J. Ågren, CALPHAD, first and second generation – Birth of the materials genome, Scripta Materialia, 70 (2014) 3-6.

[172] J.-O. Andersson, T. Helander, L. Höglund, P. Shi, B. Sundman, Thermo-Calc & DICTRA, computational tools for materials science, Calphad, 26 (2002) 273-312.

[173] A. Karma, W.J. Rappel, Numerical Simulation of Three-Dimensional Dendritic Growth, Phys Rev Lett, 77 (1996) 4050-4053.

[174] J. Friedli, J.L. Fife, P. Di Napoli, M. Rappaz, Dendritic Growth Morphologies in Al-Zn Alloys—Part I: X-ray Tomographic Microscopy, Metallurgical and Materials Transactions A, 44 (2013) 5522-5531.

[175] G. Kaptay, On the solid/liquid interfacial energies of metals and alloys, Journal of Materials Science, 53 (2018) 3767-3784.

[176] G.W. Lee, S. Jeon, C. Park, D.-H. Kang, Crystal–liquid interfacial free energy and thermophysical properties of pure liquid Ti using electrostatic levitation: Hypercooling limit, specific heat, total hemispherical emissivity, density, and interfacial free energy, The Journal of Chemical Thermodynamics, 63 (2013) 1-6.

[177] K. Ueno, Y. Shibuta, Composition dependence of solid-liquid interfacial energy of Fe-Cr binary alloy from molecular dynamics simulations, Computational Materials Science, 167 (2019) 1-7.

[178] C.L. Kelchner, S.J. Plimpton, J.C. Hamilton, Dislocation nucleation and defect structure during surface indentation, Physical Review B, 58 (1998) 11085-11088.

[179] M. Newville, T. Stensitzki, D. B. Allen, A. Ingargiola, LMFIT: Non-Linear Least-Square Minimization and Curve-Fitting for Python¶, 2014.

[180] J. Monk, Y. Yang, M.I. Mendelev, M. Asta, J.J. Hoyt, D.Y. Sun, Determination of the crystal-melt interface kinetic coefficient from molecular dynamics simulations, Modelling and Simulation in Materials Science and Engineering, 18 (2009) 015004.

[181] E. Asadi, M. Asle Zaeem, S. Nouranian, M. I. Baskes, Two-Phase Solid–Liquid Coexistence of Ni, Cu, and Al by Molecular Dynamics Simulations Using the Modified Embedded-Atom Method, 2015.

[182] J. Lin, B. Novak, D. Moldovan, Molecular Dynamics Simulation Study of the Effect of DMSO on Structural and Permeation Properties of DMPC Lipid Bilayers, The Journal of Physical Chemistry B, 116 (2012) 1299-1308.

[183] D. Sun, M. Asta, J. Hoyt, M. Mendelev, D. Srolovitz, Crystal-melt interfacial free energies in metals: fcc versus bcc, Physical Review B, 69 (2004) 020102.

[184] T.M. Yigzawe, R.J. Sadus, Intermolecular interactions and the thermodynamic properties of supercritical fluids, The Journal of Chemical Physics, 138 (2013) 194502.

[185] S. Kavousi, B.R. Novak, M.I. Baskes, M.A. Zaeem, D. Moldovan, A Modified Embedded Atom Method Potential for High Temperature and Solid-Liquid Interfacial Properties of Ti-Ni Alloys, Social Science Research Network, Rochester, NY, 2019.

[186] A. Salhoumi, P.K. Galenko, Analysis of interface kinetics: solutions of the Gibbs-Thomson-type equation and of the kinetic rate theory, IOP Conference Series: Materials Science and Engineering, 192 (2017) 012014.

[187] S. Balay, S. Abhyankar, M. Adams, J. Brown, P. Brune, K. Buschelman, L. Dalcin, V. Eijkhout, W. Gropp, D. Kaushik, Petsc users manual revision 3.8, Argonne National Lab.(ANL), Argonne, IL (United States), 2017.

[188] S. Walder, P.L. Ryder, A simple technique for the measurement of dendritic growth rates in undercooled metallic melts and its application to Ni and Ti, Materials Science and Engineering: A, 203 (1995) 197-202.

[189] P. R. Algoso, A. S. Altgilbers, W. Hofmeister, R. J. Bayuzick, The Solidification Velocity of Undercooled Nickel and Titanium Alloys with Dilute Solute, 2003.

[190] J. Lipton, W. Kurz, R. Trivedi, Rapid dendrite growth in undercooled alloys, Acta Metallurgica, 35 (1987) 957-964.

[191] J. Kierzenka, L.F. Shampine, A BVP solver based on residual control and the Maltab PSE, ACM Transactions on Mathematical Software (TOMS), 27 (2001) 299-316.

[192] W.J. Boettinger, S.R. Coriell, A.L. Greer, A. Karma, W. Kurz, M. Rappaz, R. Trivedi, Solidification microstructures: recent developments, future directions, Acta Materialia, 48 (2000) 43-70.

[193] A. Karma, W.-J. Rappel, Numerical Simulation of Three-Dimensional Dendritic Growth, Physical Review Letters, 77 (1996) 4050-4053.

APPENDIX: PERMISSION

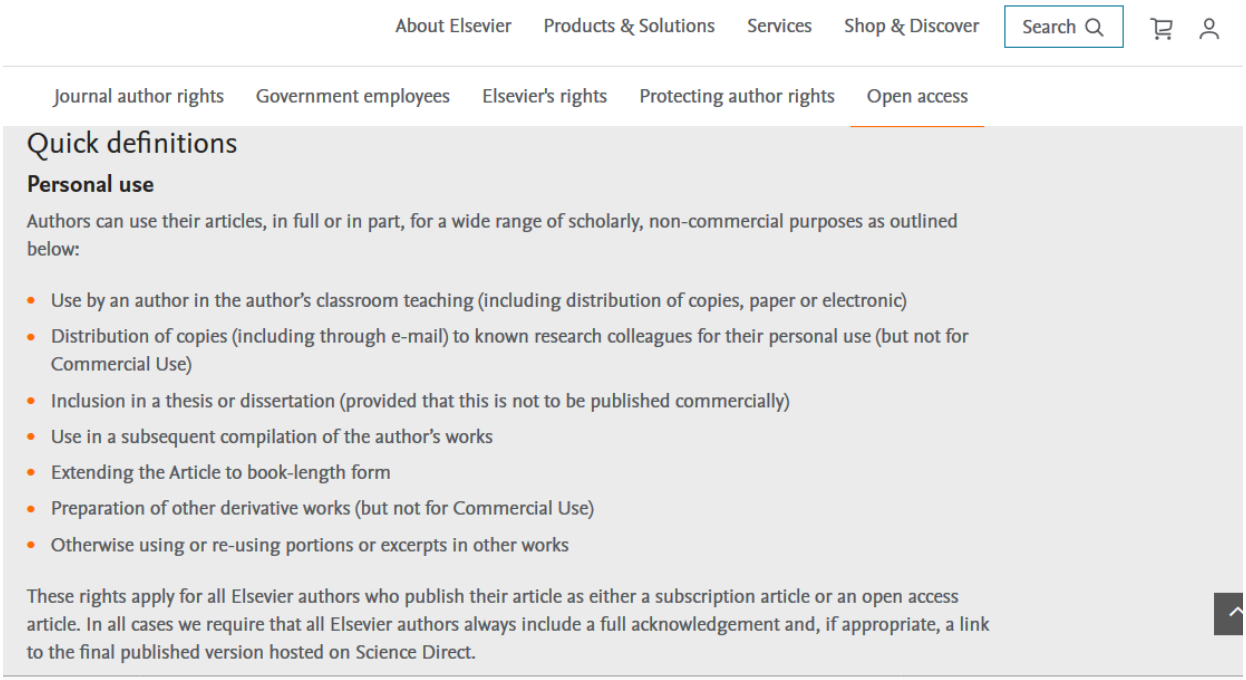

VITA

Sepideh Kavousi was born in Iran in 1987. She received her bachelor's degree in Mechanical Engineering from University of Tabriz in August 2009. Prior to pursuing a doctoral degree at Louisiana State University, starting in spring 2015, she got her Master of Science degree in Mechanical Engineering from Amirkabir University of Technology, Tehran, Iran. She is a candidate for the degree of Doctor of Philosophy in Mechanical Engineering in December 2017.